January 2022

Multi-Wavelength Analysis Of Star Formation In Galaxy Clusters

Gihan Lakmal Gamage

MULTI-WAVELENGTH ANALYSIS OF STAR FORMATION IN GALAXY CLUSTERS

by

Gihan Lakmal Gamage

Bachelor of Science, University of Ruhuna, Matara, Sri Lanka, 2016

A Dissertation

Submitted to the Graduate Faculty

of the

University of North Dakota

in partial fulfillment of the requirements

for the degree of

Doctor of Philosophy

Grand Forks, North Dakota

May

2022

Name: Gihan Gamage

Degree: Doctor of Philosophy

This document, submitted in partial fulfillment of the requirements for the degree from the University of North Dakota, has been read by the Faculty Advisory Committee under whom the work has been done and is hereby approved.

DocuSigned by:
Wayne Barkhouse
2A50DE000200413...
Dr. Wayne Barkhouse

DocuSigned by:
Tim R Young
427677AE60314EE...
Dr. Timothy Young

DocuSigned by:
D0E6B634327947F...
Dr. Kanishka Marasinghe

DocuSigned by:
760EF86F7CCE4FF...
Dr. Yen Lee Loh

DocuSigned by:
Ronald Marsh
8765BF8426ED44B...
Dr. Ronald Marsh

This document is being submitted by the appointed advisory committee as having met all the requirements of the School of Graduate Studies at the University of North Dakota and is hereby approved.

DocuSigned by:
Chris Nelson
2E0AF088C733403...
Chris Nelson
Dean of the School of Graduate Studies

4/29/2022
Date

PERMISSION

Title	Multi-Wavelength Analysis of Star Formation in Galaxy Clusters
Department	Physics and Astrophysics
Degree	Doctor of Philosophy

In presenting this dissertation in partial fulfillment of the requirements for a graduate degree from the University of North Dakota, I agree that the library of this University shall make it freely available for inspection. I further agree that permission for extensive copying for scholarly purposes may be granted by the professor who supervised my dissertation work or, in his absence, by the chairperson of the department or the dean of the School of Graduate Studies. It is understood that any copying or publication or other use of this dissertation or part thereof for financial gain shall not be allowed without my written permission. It is also understood that due recognition shall be given to me and to the University of North Dakota in any scholarly use which may be made of any material in my dissertation.

Gihan Lakmal Gamage
04/28/2022

TABLE OF CONTENTS

LIST OF FIGURES

LIST OF TABLES

ACKNOWLEDGEMENTS

I would like to thank the following people, without whom I would not have been able to complete this research.

First and foremost, my thesis advisor and mentor, Dr. Wayne Barkhouse, whose insight, patience, and knowledge steered me through this research.

To my dissertation committee members: Dr. Tim Young, Dr. Kanishka Marasinghe, Dr. Yen Lee Loh, and Dr. Ronald Marsh for their thoughtful comments and recommendations on this dissertation.

To the current and former members of the Department of Physics and Astrophysics at the University of North Dakota for the support and opportunities provided over the years.

To Sandanuwan Vithnage, who introduced me to UND and to the subject this research is based on.

To the staff at Kitt Peak National Observatory for providing me observing time and financial support.

To Haylee Archeer, Elijah Mathews, Madina Sultanova, Dean Smith, and Gregory Foote for helping me with observations at the KPNO 0.9m telescope.

Finally, to my family, for all the love and support given to me through years of studying and months of writing.

ABSTRACT

Galaxy clusters are one of the most massive structures in the Universe, consisting of hundreds to thousands of galaxies bound together by gravity. They are important laboratories for the study of the formation and evolution of galaxies over the age of the Universe. The high-density cluster environment affects the physical and morphological properties of cluster galaxies. The main goal of this dissertation is to study the effect of the cluster environment on galaxy evolution using the star-formation rate (SFR) of cluster galaxies. Multi-wavelength data at ultraviolet, u-band, and infrared wavelengths for a sample of 74 low-redshift ($0.022 < z < 0.184$) galaxy clusters were used for the analysis of this study. WIYN 0.9m+HDI telescope/detector at the Kitt Peak National Observatory was used to obtain u-band measurements of 14 galaxy clusters. This dataset was supplemented by 18 clusters from the study of Barkhouse et al. (2007), 10 clusters from Omizzolo et al. (2014), 13 clusters from Rude et al. (2020), and 19 clusters from Valentinuzzi et al. (2011). Archival data from the GALaxy Evolution EXplorer (GALEX) and the Wide-field Infrared Survey Explorer (WISE) satellites were used for ultraviolet and IR analysis, respectively. Redshifts of galaxies were obtained from SDSS spectroscopy data and were used to select cluster galaxies. The dispersion of the background-corrected red-sequence was used to separate cluster galaxies based on color into red and blue systems. A dynamical radius, r_{200}, was calculated for each cluster using the cluster velocity dispersion, and used as a normalization factor to compare cluster characteristics. For each passband, the radial dependence ($0.0 \leq r/r_{200} \leq 1.0$) of the SFR was measured for all cluster

galaxies. Evidence for the quenching of star formation towards the cluster center was found for both red and blue galaxies, with the blue galaxy SFR decreasing more than for the red galaxies. The cluster galaxy sample was divided into giant (high-mass) and dwarf (low-mass) galaxies using their absolute r-band magnitude. It was found that dwarfs are more susceptible to environmental effects compared to giant systems. These results are consistent for all multi-wavelength data used in this study. While ram pressure stripping plays a more important role in quenching star formation towards the cluster core, other mechanisms, such as galaxy harassment and starvation, were found to be more effective in the cluster outskirts.

Chapter I

INTRODUCTION

1.1 Galaxy Clusters

Galaxies are not randomly scattered throughout the Universe; instead, nearly all galaxies are found in groups or clusters. Galaxy clusters are one of the most massive structures in the Universe, consisting of hundreds to thousands of galaxies bound together by gravity. Most clusters are approximately in a state of dynamical equilibrium, making them the largest virialized system in the Universe. Clusters also contain a substantial amount of dark matter, as well as hot gas as evident by x-ray observations, known as the intracluster medium (ICM) (Voit, 2005). Due to the high density of galaxies and the pressure of the ICM, galaxy clusters play a vital role in understanding environmental effects on galaxy evolution. In addition, galaxy clusters are used as laboratories to study physics on a grand scale. For example, the Coma cluster provided the first evidence that the mass of the Universe is primarily made up of dark matter, not baryonic matter (Zwicky, 1933).

Under the Λ-Cold-Dark-Matter model of the universe (ΛCDM), objects are initially built up from quantum fluctuations in an otherwise smooth distribution of dark matter. With time, the dark matter begins gravitational collapse in over-dense regions, building up mass and attracting baryonic matter (Eisenstein & Hu, 1998). Since these perturbations have greater amplitude on smaller scale, small sub-galactic structures, such as stars, are the first to form. Larger structures, such as galaxy clusters, are built up from collections of smaller structures. This type of structure

formation is known as the hierarchical (bottom-up) scenario, where larger structures are made from smaller ones (Kravtsov & Borgani, 2012). Although most of the mass in a galaxy cluster is composed of dark matter, the primary way of understanding galaxy evolution is by observing baryonic matter, such as stars, gas, and dust, since this matter emits and absorbs light.

1.1.1 Cluster Catalogs

The history of studying galaxy clusters dates back to the 18^{th} century, but was revolutionized in the 1920s by Edwin Hubble's proof that some fuzzy objects in Messier's catalog are galaxies similar to our own (Hubble, 1925). The galaxy cluster catalog developed by George Abell in 1958 using the red Palomar Sky Survey plates is the most widely used catalog for low redshift (z) galaxy clusters since it represents a statistically complete sample (Abell, 1958). Also using Palomar plates, Fritz Zwicky and his associates constructed the *Catalogue of Galaxies and Clusters of Galaxies* (CGSS) (Zwicky et al., 1961). The cluster size of Zwicky's catalog is heavily distant-dependent (Abell, 1962). Due to this reason, it has not been used as extensively as the Abell catalog.

1.1.2 Types of Clusters

Galaxy clusters display a variety of morphological forms, ranging from rich clusters that accumulate thousands of galaxies to poor groups. Scientists used these apparent differences in optical wavelengths to classify clusters. Abell (1958) used the richness of a cluster to divide them into two categories: Regular and Irregular. Zwicky et al. (1961) classified clusters into three broad categories using their concentration: compact, medium compact, and open. In 1970, Bautz & Morgan developed a five-part classification that depends on the relative contrast of the Brightest Cluster Galaxy (BCG) to others in each cluster. Three primary types of this classification includes:

1) Type I – clusters contain a central 'cD' galaxy, 2) Type II – clusters where the brightest galaxy or galaxies are intermediate between a 'cD' and a giant elliptical, and 3) Type III – no dominant galaxy present. In addition, Type I-II and Type II-III were included as two intermediate categories.

Rood & Sastry (1971) introduced a classification scheme based on the distribution of the ten most-luminous galaxy members of the cluster. They divided clusters into six main groups: 1) 'cD' cluster – a cluster dominated by a bright member that is three or more times brighter than any member in the cluster, 2) 'B' cluster – a cluster with two supergiant galaxies present, 3) 'L' cluster – three or more of the ten brightest galaxies are arranged in a line with comparable separations, 4) 'C' cluster – four or more members of the ten brightest galaxies are located near the center forming a "core-like" feature, 5) 'F' clusters – several of the ten brightest galaxies are distributed in a flattened configuration, and 6) 'I' cluster – irregular clusters with no well defined center.

1.2 Morphological Classification of Galaxies

The Hubble tuning fork diagram, with elliptical galaxies located at the handle of a fork which splits into barred and unbarred spiral galaxies for the prongs (Fig. 1.1), is the most common method used to classify luminous galaxies (Abraham & van den Bergh, 2001). Elliptical galaxies are classified by their ellipticity (increasing from left to right on the handle), and spiral galaxies (barred or unbarred) are classified based on the compactness of their spiral arms and the relative brightness of the central bulge. S0-type galaxies are those that contain a disk but no spiral arms, and little interstellar matter. A fourth major class of galaxies, irregulars, was not included in Hubble's original classification diagram. These galaxies appear peculiar in their shape and contain lots of interstellar matter. In some sense, these galaxies represent the miscellaneous bin in which galaxies are placed if they don't fit into the other regular

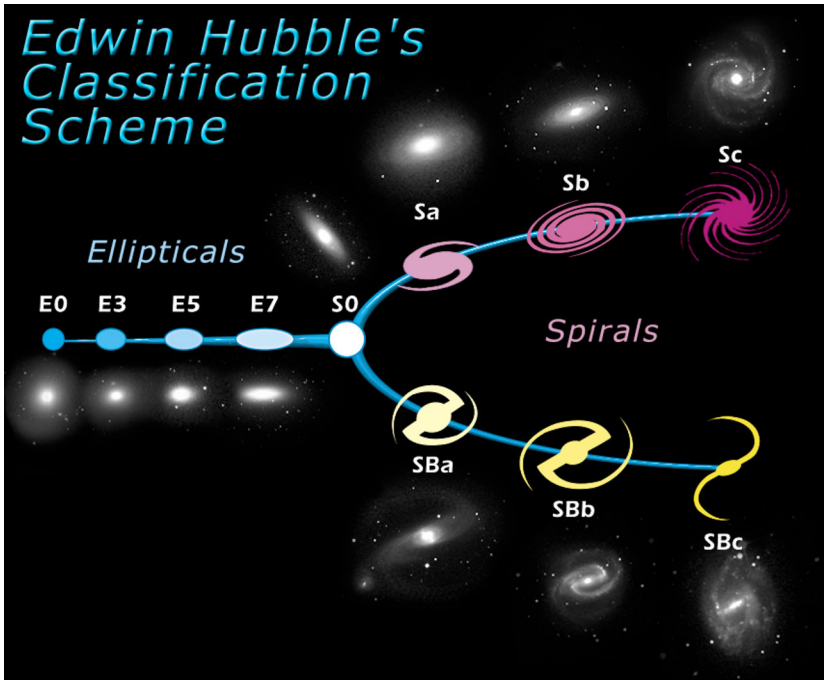

Figure 1.1: The Hubble tuning fork diagram (image credit - ESA/Hubble).

galaxy types.

1.2.1 Dwarf Galaxies

Galaxies of small mass (size), low luminosity, and faint surface brightness are called dwarf galaxies (Hodge, 1971). Dwarf galaxies are the most abundant galaxies in the Universe and are mostly found in galaxy groups and clusters. Due to their low luminosity, dwarf galaxies are in general difficult to detect.

Dwarf galaxies are classified into three main types; dwarf elliptical (dE), dwarf irregular (dI), and dwarf spheroid (dSO). The dE galaxies are considered a continuation of the giant elliptical type, but smaller in scale. They are very numerous and strongly clustered (Vader & Sandage, 1991). In general, dE galaxies have little star formation and are found to be, on average, metal-poor. The dS0 galaxy type, which is a dwarf version of S0 galaxies, are much less common than dEs. These do not contain a lot of interstellar gas, but show a complex star formation history. The dI

galaxies lack organized structure and thus are irregular in shape. They are normally gas-rich, metal-poor systems that usually contain several compact high star-forming regions. These are very common in the Local Group of galaxies (Vithanage, 2018).

1.3 Observable Properties of Clusters

1.3.1 Velocity Dispersion and Mass Estimates

The radial velocity of a galaxy can be obtained by measuring its redshift from its spectrum. The velocity distribution of a relaxed galaxy cluster is expected to be a Gaussian function with a line-of-sight velocity dispersion, σ_{vel}. The accuracy of σ_{vel} depends on the number of galaxies with measured radial velocities and the method used to identify nonmembers (Voit, 2005).

Since galaxy clusters are considered relaxed, gravitationally bound systems, the mass of a cluster can be estimated using the virial theorem

$$M \sim \sigma_{vel}^2 R_{cl}/G, \tag{1.1}$$

where R_{cl} is the cluster radius and σ_{vel} is the velocity dispersion. For a rich cluster, its mass is $\sim 10^{15} M_\odot$. Typically, the total mass-to-light ratio of a cluster is found to be (Mo et al., 2010)

$$\Big(\frac{M}{L_{tot}}\Big) \sim 350h\Big(\frac{M_\odot}{L_\odot}\Big). \tag{1.2}$$

Hence, only a small fraction of the total gravitational mass of a cluster is associated with galaxies. The mass of the ICM can be estimated using x-ray observations of clusters and is found to be about 10× more than the total stellar mass of member galaxies. Yet, the total gravitational mass of a cluster is found to be an order of magnitude larger than the combined masses of stars and hot gas, indicating that the

cluster mass is dominated by dark matter. Zwicky (1933) was the first to notice this while studying the velocity dispersion of the Coma cluster.

1.3.2 Luminosity Function

The number of galaxies per unit volume in a given luminosity interval is defined as the luminosity function (LF). The LF for galaxy clusters can be used to study the influence of the cluster environment on the galaxy population (Barkhouse et al., 2007). Schechter (1976) suggested that cluster LFs are universal in shape and can be described mathematically using a specific function (Schechter function), while several other studies have shown that the LF is not universal (e.g. Barkhouse et al. (2007); López-Cruz et al. (1997)). Barkhouse et al. (2007) showed that the cluster LF is typically characterized by the sum of two Schechter functions, one Schechter function for the giant (bright) galaxy population and one for the dwarf (faint) galaxy population. The Schechter function has the form

$$\phi(L)dL = \phi^*(L/L^*)^\alpha \exp(-L/L^*)d(L/L^*), \tag{1.3}$$

where, $\phi(L)dL$ is the number of galaxies per unit volume in the luminosity interval L to $L + dL$, ϕ^* is the number per unit volume, and L^* is the characteristic luminosity (representing the turnover in the LF).

1.3.3 Morphology-Density Relation

It is well established that early-type galaxies (ellipticals and S0s) are more commonly found in the center of galaxy clusters, and that late-type galaxies (spirals and irregulars) dominate the field or low-density environment. This correlation, referred to as the morphology-density relationship (Dressler, 1980), indicates that local density has an effect on galaxy morphology. The morphology-density relation is consistent

with a model in which spirals loose gas as they fall into the cluster environment and transform into early-type galaxies. A study by Goto et al. (2003) using the Sloan Digital Sky Survey (SDSS), provided evidence that the fraction of late-type galaxies increases with increasing cluster-centric radius (Fig. 1.2). Thus, the outskirts of galaxy clusters are dominated by spiral galaxies while the central regions contain a large fraction of elliptical/S0 galaxies.

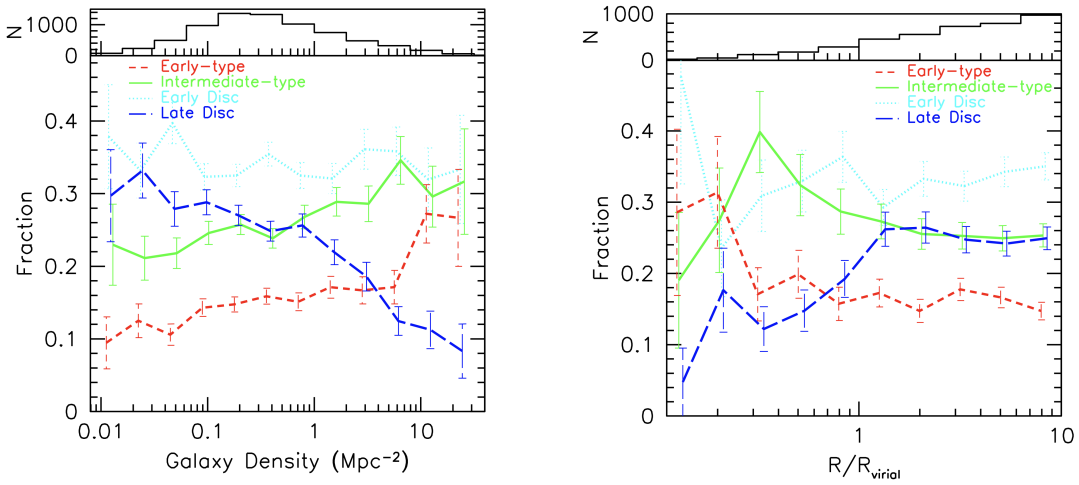

Figure 1.2: The morphology–density (a) and morphology–radius (b) relations of galaxy clusters. Fractions of each galaxy type are plotted against local galaxy density (a) and cluster-centric radius (b). The short-dashed, solid, dotted, and long-dashed lines represent early-type, intermediate-type, early-disk, and late-disk galaxies, respectively. The histogram in the upper panel shows the numbers of galaxies in each bin of cluster-centric radius (Goto et al., 2003).

1.3.4 Color-Magnitude Relation

Early researchers in the field of galaxy cluster studies found that a color-magnitude diagram of galaxies from local clusters, such as Virgo and Coma, depict passively evolving galaxies (elliptical/S0) confined to a prominent linear feature (Visvanathan & Sandage, 1977). This feature, known as the red-sequence, has a very small scatter

and appears to be extremely homogeneous from cluster-to-cluster (Lopez-Cruz et al., 2004). The small scatter of the red-sequence implies that these passively evolving red-sequence galaxies were formed coevally at higher redshifts (Stott et al., 2009). Along the red-sequence, galaxy color becomes bluer towards fainter magnitudes (Fig. 1.3). This color-magnitude relation (CMR) was first noted by Baum (1959) for field elliptical galaxies.

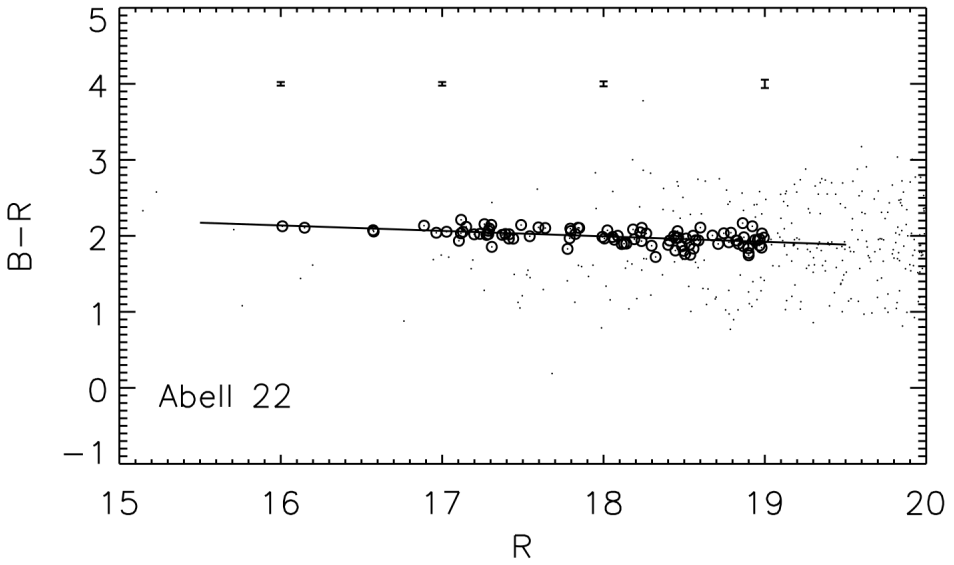

Figure 1.3: Color-magnitude diagram for Abell 22 with the red-sequence delineated by the dotted line. Representative error bars are shown for a range of magnitudes (Stott et al., 2009)

A system containing older or metal-rich stars can cause a galaxy color to be red, which then compromises the slope. This dual interpretation of the color-magnitude relation is now well known as the age-metallicity degeneracy of stellar populations. Kodama & Arimoto (1997) compared color-magnitude diagram simulations to observations in order to break this degeneracy and determined that the color-magnitude relation is primarily a mass-metallicity effect and is not due to differences in stellar age. Stars in a galaxy are embedded in an interstellar medium (ISM) consisting of gas

(both hot and cold) and dust. The origin of the mass-metallicity relation is thought to be a result of interstellar matter heating by supernovae. When the thermal energy of the gas exceeds the binding energy, a galactic wind is formed, ejecting the gas from a galaxy (Stott et al., 2009). More massive (hence bright) galaxies, due to their deeper potential wells, can retain their gas for longer times than less massive (hence less-luminous) galaxies, and thus reach higher metallicities. As a result, massive metal-rich galaxies will appear progressively redder than less massive galaxies (Carlberg, 1984).

The observed slope of the CMR for clusters at similar redshifts are found to be extremely homogeneous (Lopez-Cruz et al., 2004; López-Cruz et al., 1997). A study conducted by Gladders & Yee (2000) used this homogeneity to explore the possibility of using the CMR to identify previously unknown galaxy clusters (red-sequence method). Stott et al. (2009) found the rest frame slope of the red-sequence in galaxy clusters increases with redshift. According to Gladders et al. (1998), this change in the red-sequence slope with redshift may be used to constrain the formation epoch of elliptical galaxies within cluster cores. They show that the formation of these galaxies must have been at $z \geq 2$.

1.3.5 Butcher-Oemler Effect

A study conducted by Butcher & Oemler (1978) of the galaxy populations of clusters at redshifts between 0.3 and 0.5, found a dramatic increase in the fraction of blue galaxies compared to present-day clusters. This is known as the Butcher-Oemler effect and it is associated with an increase of the number of spiral galaxies with increasing redshifts. This indicates that the population of galaxies in clusters is rapidly evolving with redshift, most likely due to specific processes that operate in dense environments.

1.4 Evolution of Galaxies in Clusters

As mentioned in previous sections, a galaxy cluster is a multi-component system in which dark matter, hot gas, and galaxies evolve in a tightly coupled way. This high-density cluster environment affects physical and morphological properties of cluster galaxies.

1.4.1 Ram-Pressure Stripping

As galaxies move through the ICM, their interstellar matter will experience a ram pressure from the ICM. If the ram pressure is sufficiently strong, it may strip the gas from the galaxy. This is known as ram-pressure stripping.

For a galaxy moving through the ICM of density ρ_{ICM} with velocity V, the ram pressure (P_{ram}) on the ISM is given by

$$P_{ram} = \rho_{ICM} V^2. \tag{1.4}$$

If the mean surface density of the interstellar gas is σ_g and the mean mass density (dominated by stars) is σ_s, the gravitational force per unit area on the interstellar gas (F_g) is given by

$$F_g = 2\pi G \sigma_g \sigma_s. \tag{1.5}$$

The ISM is bound to the disk of a galaxy due to its self-gravitational force. If the ram pressure exceeds the binding force, the gas will be stripped. Since, σ_g and σ_s decreases as the galactocentric distance increases, there exists a radius in the disk beyond which ram-pressure stripping is inefficient (Mo et al., 2010).

Gas-rich galaxies that fall into clusters are expected to either have their star formation enhanced due to the ram-pressure squeezing of interstellar material within these galaxies, thus triggering star formation, or have their star-forming gas removed,

thus truncating star formation (Taranu et al., 2014). It is also possible that in-falling galaxies will experience both mechanisms over a short timescale, resulting in a burst of star formation followed by quenching. Due to their low mass, the ICM pressure can overcome the gravitational restoring force of dwarf galaxies, which cause them to lose their star-forming gas.

The recent discovery of "jellyfish" galaxies (galaxies with clear 'tentacles' of stripped gas extending beyond the optical extent of the galaxy) in the cluster environment provides observational evidence for ram-pressure stripping (Fig 1.4). The presence of a small number of red spirals near the cluster center may also be an indicator of the effects of ram-pressure on massive galaxies.

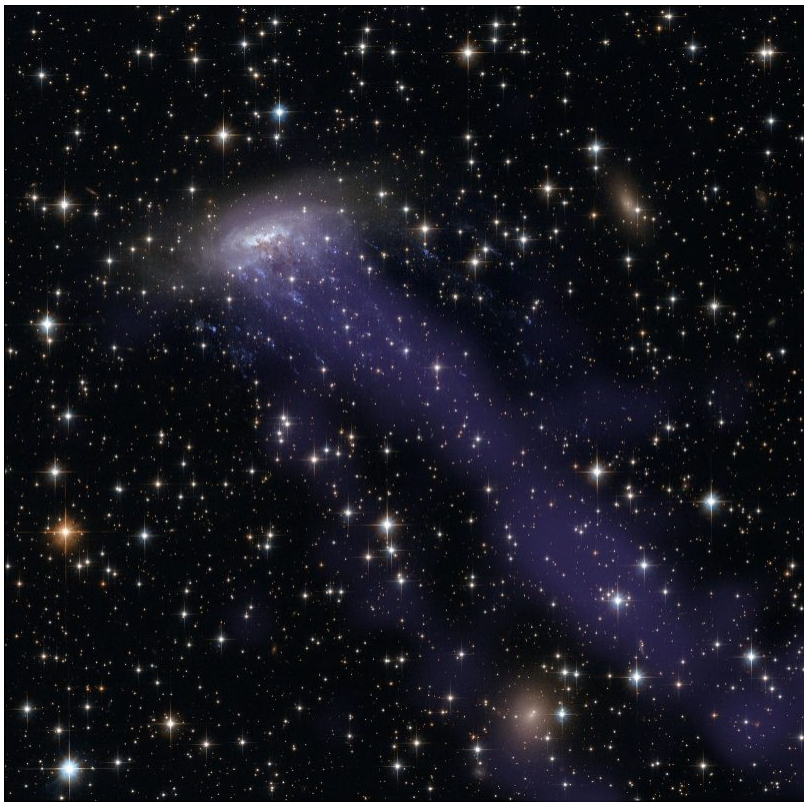

Figure 1.4: Composite pseudo color image of galaxy ESO 137-001, which includes visible wavelength observations from Hubble and x-ray light from the Chandra X-ray Observatory (in blue). It reveals a tail of hot gas that has been stripped from the galaxy (image credit - NASA/ESA).

1.4.2 Galaxy Strangulation

It has been proposed that spiral galaxies are embedded in an extended hot/warm gas halo which feeds the disk and thus supports star formation. Since this gas reservoir is relatively loosely bound to the galaxy, it is fairly easily ripped off either by ram-pressure or gravitational tidal forces, thus quenching star formation. This is called galaxy strangulation, and results in a fairly gradual decline of the galaxy's star-formation rate as it slowly runs out of fuel (Taranu et al., 2014).

1.4.3 Galaxy Harassment

The dense environment of clusters provides many opportunities for repeated gravitational interactions between galaxies. Due to the typical high speed of galaxies in a cluster, as measured by the velocity dispersion, galaxy merging is unlikely. These interactions can increase the internal energy of the interstellar matter in the host galaxy, causing it to heat up and expand. Effect of these high-speed encounters are referred to as galaxy harassment.

Using simulations, Moore et al. (1996) showed that a Sc-Sd type galaxy can transform into a dE galaxy by interacting with a more massive galaxy. Since dwarf ellipticals are abundant in clusters, it may well be that they are the remnants of disk galaxies that have experienced such harassment. Although harassment may have a strong impact on loosely-bound Sc-Sd type galaxies, it has little impact on more compact Sa-Sb type galaxies and early type disk galaxies (Moore et al., 1996).

1.4.4 Galactic Cannibalism

The motion of a galaxy through the ICM can be subjected to a drag force, dynamical friction, causing a loss of kinetic energy and momentum of a massive particle as it moves through a homogeneous system. As a result, galaxies will migrate toward the

center core of the cluster. If the dynamical friction timescale is sufficiently short, the galaxy will reach the cluster center and merge with the central galaxy already residing there. Hence, the central galaxy may accrete satellite galaxies and become more massive. This process is referred to as galactic cannibalism (Schneider, 2007).

The central cluster galaxy, also referred to as the BCG, is a massive elliptical galaxy with a diffuse and extended halo, known as a cD Galaxy. Hausman & Ostriker (1978) suggests that these cD galaxies are a product of galactic cannibalism. Such a process can explain not only the mass of the BCG, but also their diffuse halos, which are considered to be the result of material being stripped from cannibalized galaxies as they spiral into the cluster center. Some studies have found BCGs with multiple nuclei (Seigar et al., 2003). These "multiple nuclei" provide observational evidence for models which postulate that BCGs are formed via galactic cannibalism.

1.5 Star Formation in Galaxy Clusters

The formation and evolution of stars is an interplay between gravity and pressure. The gravitational collapse of dense regions in the interstellar medium of galaxies can be triggered by shock waves from supernovae explosions, or by gravitational tidal forces from encounters with other nearby galaxies, which leads to the birth of a star. Hot, massive stars live short lives and emit light primarily at ultraviolet (UV) wavelengths, while less-massive, cool stars have much longer lives, and emit light primarily at red wavelengths. Thus color can be used to separate galaxies into star-forming and non-star-forming populations (Kennicutt, 1998).

Individual stellar investigations become challenging as the distance to extragalactic systems increases. Hence, in extragalactic astronomy, astronomers study the collective behavior of star formation rather than the formation of individual stars (Zezas & Baut, 2021). Understanding star formation activity in a galaxy provides a key ingredient to obtaining a more complete knowledge regarding the evolution of stellar

populations in a galaxy. Since star formation is directly affected by the surrounding environment, studying star formation of cluster galaxies can give us a deeper understanding of the dynamical processes at work in high-density regions. The star formation rate (SFR) is the total mass of stars formed per unit time, often given in units of solar masses per year ($M_\odot$ yr^{-1}). The properties and evolution of individual stars are primarily determined by their mass. Hence, any available tracer of the SFR depends on the shape of the mass distribution of formed stars, i.e. on the stellar initial mass function (IMF). The IMF, $\phi(m)$, is defined so that $\phi(m)dm$ is the number of stars born per mass interval dm. The IMF is assumed to be a continuous function and is often normalized as (Zezas & Baut, 2021)

$$\int_{M_l}^{M_u} m\phi(m)dm = 1, \tag{1.6}$$

where M_l and M_u are the lower and upper mass limits. It is usual to represent the IMF with a power-law function, $\phi(m) \propto m^{-\alpha}$. The power-law index depends on the considered mass range. For example, for stars in the mass range $0.4M_\odot - 10M_\odot$, Salpeter (1955) determined this index to be 2.35. This is known as the Salpeter IMF.

1.6 Traces of Star Formation Rates

Various indicators of star formation in galaxies have been developed using different wavelengths, including UV continuum luminosity, infrared (IR) luminosity, nebular recombination line luminosity (Hα), and radio luminosity (Hopkins et al., 2003). There is also evidence that x-ray luminosity is an important star formation indicator (Griffiths & Padovani, 1990). Each one of these indicators sample a slightly different star-formation timescale.

1.6.1 Ultraviolet Continuum

The integrated spectrum of a galaxy in the wavelength range 1200 - 2800 Å is dominated by the photospheric emission from young, hot, massive stars. Hence, UV emission is one of the most direct probes of recent star formation. Since the lifetime of massive stars are $\leq 10^8$ yr, the UV luminosity of a galaxy can be used as a diagnostic of its current star formation (Mo et al., 2010). The main drawbacks of using UV emission to study star formation are its extreme sensitivity to dust absorption and the form of the IMF. Also, UV measurements can be heavily contaminated by UV emission from an active galactic nucleus (AGN)(Zezas & Baut, 2021).

1.6.2 Recombination Lines

UV radiation is capable of ionizing nearby hydrogen gas in the interstellar medium (H II region). When a free electron recombines with an ionized hydrogen atom and moves down through different energy orbits, photons of different wavelengths will be emitted, Hα being the most prominent in the optical range at a wavelength of 656.3 nm (red). Only extremely massive stars ($\geq 10M_{\odot}$) can produce high-energy radiation that's sufficient to ionize hydrogen gas in the ISM. Hence the strength of a nebular emission line is almost an instantaneous measure of the SFR (Zezas & Baut, 2021). Chief limitations of Hα SFR measurements are its sensitivity to uncertainties in the assumed IMF and extinction. Some parts of the created H II regions might be optically thin, and a certain fraction of the ionizing radiation eventually escapes into the diffuse medium of the galaxy. This escape fraction of ionizing photons can add a considerable uncertainty to SFR measurements using Hα lines (Kennicutt, 1998).

1.6.3 Far-Infrared Continuum

A significant fraction of the starlight in the Universe is absorbed by interstellar dust and re-emitted at IR wavelengths of roughly 10 - 300 μm (Kennicutt & Evans, 2012). Since the absorption efficiency of dust peaks at UV wavelengths, the far-infrared (FIR) luminosity can be a sensitive indicator of a young stellar population and thus star formation. The efficiency of the FIR luminosity as a SFR tracer depends on the opacity of the dust in the star forming region. If the dust is thick, escape fraction would be much less, in which case the FIR luminosity measures the bolometric luminosity of the starburst region (Kennicutt, 1998). FIR observations provide an excellent tool to study the star formation activity in dusty starburst galaxies without the complications of dust biases (see section 3.9).

1.6.4 Radio Continuum

Radio continuum emission from star-forming galaxies has two components: thermal bremsstrahlung from ionized hydrogen in H II regions, and non-thermal synchrotron emission from cosmic ray electrons spiraling in the magnetic field of a galaxy (Bell, 2003). At lower frequencies ($\leq$ 5 GHz), non-thermal radiation tends to dominate. Although a direct SFR calibration has not been derived for radio wavelengths, Bell (2003) used the tight radio-FIR correlation (see de Jongl et al., 1985) to estimate the SFR at 1.4 GHz frequency. The main advantage of using radio emission to study the SFR is their insensitivity to dust obstructions. This makes radio continuum ideal to study star forming galaxies at high redshifts.

1.6.5 X-Ray Emission

X-ray emission that is not associated with AGN accretion disks, such as, massive x-ray binaries, supernovae, and supernova remnants, is expected to be correlated with

a young stellar population and thus recent star formation (Kennicutt & Evans, 2012). The x-ray luminosity of galaxies is observed to be correlated with their IR and radio continuum fluxes (Bauer et al., 2002). Ranalli et al. (2003) used this correlation to estimate the SFR for integrated x-ray luminosities between 2 - 10 keV.

1.7 Dwarf-to-Giant Ratio

The dwarf-to-giant ratio (DGR), the ratio of the number of dwarf galaxies to the number of giant galaxies, provides a non-parametric method to describe the relative population of high- and low-mass galaxies in the cluster environment. Using a sample of 15 galaxy clusters observed in the ultraviolet (u-band), which is sensitive to star formation, and red wavelengths (r-band), Rude et al. (2020) found that the DGR increases towards the cluster outskirts, with the u-band DGR increasing faster compared to the r-band (Fig. 1.5). The decline in the DGR towards the cluster center for both filters implies that a mechanism, like ram-pressure stripping, quenches star formation.

1.8 Blue Fraction

A comparison of the number of red and blue galaxies gives a rough indication of the relative mixture of early- and late-type galaxies in a cluster (Barkhouse et al., 2009). The blue fraction (BF) is given by

$$f_b = N_b/(N_b + N_r), \tag{1.7}$$

where N_b and N_r are the number of blue and red galaxies, respectively.

Since the morphology-density relation shows that the galaxy type changes with environment such that blue galaxies are more abundant in the outskirts of clusters, the blue fraction would be expected to increase with cluster-centric radius. Rude

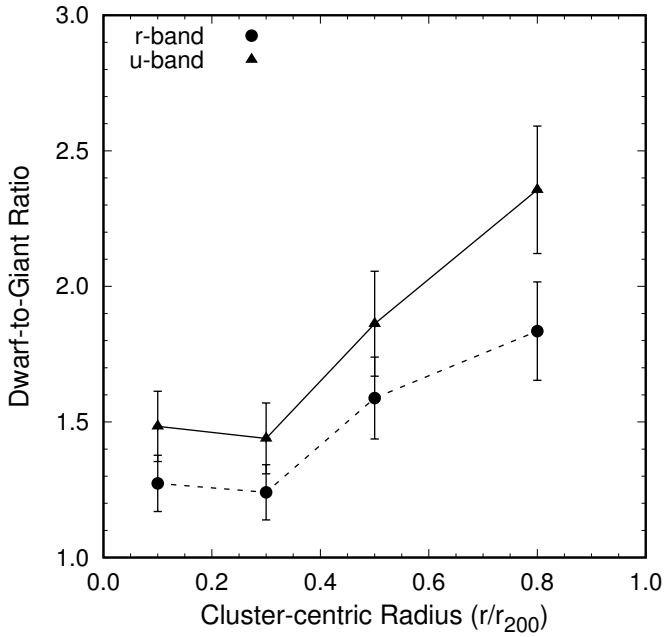

Figure 1.5: The DGR as a function of normalized cluster-centric radius (r_{200}) in both the r- and u-bands for four cluster-centric radial bins (Rude et al., 2020).

et al. (2020) found a greater blue fraction for the cluster dwarf galaxy population compared to giant galaxies, over all measured cluster-centric distances. In addition, an increase in the blue fraction for both dwarf and giant galaxies with increasing cluster-centric radius was measured (Fig. 1.6).

1.9 Motivation

As galaxies fall into the cluster environment, star formation and galaxy morphology will be subjected to influences of cluster dynamics. In the cluster outskirts, mechanisms such as galaxy harassment and gravitational tidal effects may be responsible for these changes. Towards the cluster center, ram pressure should dominate since the ICM density is higher towards the core (Rude et al., 2020). The dominance of each mechanism will also depend on the size of the galaxy. For example, ram-pressure effects in the cluster outskirts might strip the ISM from dwarf galaxies, but not for massive galaxies due to the self-gravity of the host galaxy. The discovery of "jellyfish"

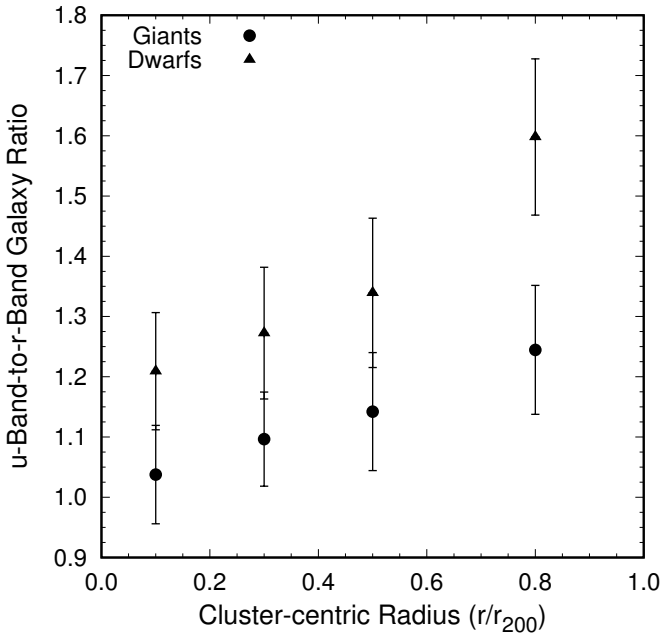

Figure 1.6: The ratio of the number of u- to r-band galaxies as a function of normalized cluster-centric radius (r_{200}) in both the r- and u-bands for four cluster-centric radial bins (Rude et al., 2020).

galaxies in the cluster environment suggests that ram-pressure is capable of stripping gas from infalling galaxies, producing bursts of star formation. Hence, studying the star formation rate of cluster galaxies as a function of cluster-centric radius using multi-wavelength observations will provide valuable insights into the impact of the cluster environment on galaxy stellar populations.

1.10 Outline

Although several studies have examined the SFR of high-mass cluster galaxies, little in comparison has been done for the combined galaxy population from dwarf galaxies to more massive systems. Additionally, most studies are limited to one or two wavelength ranges (passbands) using a relatively small sample of clusters. The goal of my dissertation is to study the SFR of giant and dwarf cluster galaxies using multi-wavelength observations in ultraviolet, u-band, and infrared for a sample of 74

low-redshift galaxy clusters.

This dissertation presents a comprehensive study of u-band observations for 14 galaxy clusters obtained using the WIYN 0.9m + HDI telescope/detector at the Kitt Peak National Observatory (KPNO). This dataset is supplemented by 18 clusters from the study of Barkhouse et al. (2007), 10 clusters from Omizzolo et al. (2014), 13 clusters from Rude et al. (2020), and 19 clusters from Valentinuzzi et al. (2011). Archival data from the GALaxy Evolution EXplorer (GALEX) and the Wide-field Infrared Survey Explorer (WISE) satellites are used for ultraviolet and IR analysis, respectively. The redshift of galaxies is obtained using the SDSS spectroscopy data and is used to select cluster galaxies. The dispersion of the background corrected red-sequence is used to separate cluster galaxies into two color bins, red and blue. For each passband, the SFR of both dwarf and giant galaxies of both colors are calculated and plotted as a function of cluster-centric radius.

In addition, the SFR measurements are compared with the SFR calculations from the GALEX–SDSS–WISE Legacy Catalog (GSWLC) (Salim et al., 2018).

This dissertation is organized into six chapters. The target clusters and observations are described in Chapter II. Data reductions and calibration measurements are outlined in Chapter III. The analysis of multi-wavelength data is presented in Chapter IV and the interpretation of the results is discussed in Chapter V. Chapter VI, contains a summary of the results and interpretations, along with a discussion of future work.

The cosmological parameters of $H_0 = 70$ km s^{-1}Mpc^{-1}, $\Omega_\Lambda = 0.7$, and $\Omega_m = 0.3$ are used in this study.

Chapter II

OBSERVATIONS

2.1 Introduction

The main goal of this dissertation, as outlined in Chapter I, is to study the star formation rate of 74 galaxy clusters using multi-wavelength data. The selected galaxy cluster sample has a redshift range of $0.022 < z < 0.184$ and has spectral data available through the SDSS. An overview of cluster properties can be found in Tables $2.1 - 2.5$. The redshift and central coordinates (BCG location) of each cluster were obtained from the NASA Extragalactic Database (NED).[1]

The WIYN 0.9m telescope was used to obtain u-band data for 14 galaxy clusters. The u-band data used in Rude et al. (2020) and Omizzolo et al. (2014) were used for this study as well. Rude et al. used archival u-band observations from the Canada-France-Hawaii Telescope (CFHT) for their study and Omizzolo et al. used u-band observations from the 2.3m Bok telescope at KPNO, 2.5m Isaac Newton Telescope at the Roque de los Muchachos Observatory, and the Large Binocular Telescope at the Mount Graham International Observatory. For clusters used in Valentinuzzi et al. (2011) and Barkhouse et al. (2007), u-band data were obtained from the Data Release 16 (DR16) of the SDSS.[2]

All final cluster galaxy catalogs (see section 3.7) were matched with archival data from GALEX and WISE satellites to measure fluxes at UV and IR wavelengths,

[1] `https://ned.ipac.caltech.edu`
[2] `https://www.sdss.org/dr16/`

respectively.

Table 2.1: Properties of the galaxy cluster sample observed using WIYN 0.9m telescope.

Cluster	RA (deg)	DEC (deg)	z	Exposure Time (s)
A1142	165.20375	10.55972	0.03490	18 × 900
A1213	169.12113	29.26029	0.04690	14 × 900
A2152	241.38417	16.44194	0.04100	22 × 900
A2399	329.35750	-7.79472	0.05790	19 × 900
A2572	349.59827	18.74020	0.04030	20 × 900
A2589	350.97292	16.80889	0.04140	19 × 900
A2593	351.08417	14.65111	0.04130	21 × 900
A260	27.68708	33.09000	0.03630	23 × 900
A2634	354.60708	27.01250	0.03139	20 × 900
A2666	357.73429	27.14474	0.02683	19 × 900
A582	112.04873	41.96415	0.05820	13 × 900
A634	123.64041	58.04786	0.02650	20 × 900
A671	127.12198	30.41684	0.05020	27 × 900
A779	139.95500	33.76028	0.02249	18 × 900

Table 2.2: Properties of Barkhouse et al. cluster sample.

Cluster	RA (deg)	DEC (deg)	z
A1413	178.82875	23.40861	0.14360
A154	17.74197	17.66563	0.06360
A1569	189.07791	16.59155	0.07400
A1650	194.67125	-1.75694	0.08384
A1656	194.95305	27.98069	0.02316
A1775	205.47417	26.37194	0.07203
A1913	216.71584	16.67630	0.05280
A2022	226.08225	28.42267	0.05780
A2029	227.72917	5.72000	0.07872
A21	5.12832	28.62738	0.09460
A2244	255.67875	34.06194	0.09680
A2255	258.12936	64.09257	0.08029
A2356	323.94292	0.11583	0.11800
A2440	335.97042	-1.63778	0.09090
A2670	358.55708	-10.41889	0.07619
A646	125.54000	47.09778	0.12700
A690	129.80942	28.83987	0.07880
A84	10.44625	21.41389	0.10300
A999	155.84220	12.84667	0.03230

Table 2.3: Properties of Omizzolo et al. cluster sample.

Cluster	RA (deg)	DEC (deg)	z
A119	14.07625	-1.21667	0.04433
A1291	173.04125	56.03083	0.05154
A1668	195.94000	19.27139	0.06408
A1795	207.22083	26.59556	0.06248
A1831	209.82292	27.97278	0.06295
A1983	223.18334	16.74606	0.04515
A1991	223.63083	18.64194	0.05813
A2124	236.25000	36.06611	0.06670
A2149	240.40874	53.87859	0.06530
A2169	243.54000	49.15306	0.05850

Table 2.4: Properties of Rude et al. cluster sample.

Cluster	RA (deg)	DEC (deg)	z
A1920	216.85230	55.75038	0.13100
A1940	218.86860	55.13115	0.14000
A2100	234.07730	37.64386	0.15300
A2107	234.91270	21.78268	0.04100
A2147	240.57100	15.97459	0.03500
A2199	247.15940	39.55117	0.03000
A351	36.33316	-8.72184	0.11100
A362	37.92159	-4.88268	0.18400
A655	126.37120	47.13358	0.12700
A76	9.98318	6.84863	0.04100
A795	141.02210	14.17265	0.13600
A98N	11.60310	20.62180	0.10400
A98S	11.62217	20.46796	0.10400

Table 2.5: Properties of Valentinuzzi et al. cluster sample.

Cluster	RA (deg)	DEC (deg)	z
A147	17.04792	2.17611	0.04401
A160	18.21417	15.51493	0.04374
A168	18.80000	0.33000	0.04474
A193	21.26583	8.68806	0.04859
A2457	338.93833	1.47591	0.05941
A2622	353.77083	27.37000	0.06200
A2626	354.12625	21.14250	0.05415
A2657	356.21253	9.14434	0.04043
A2665	357.68935	6.11143	0.05560
A602	118.35083	29.36611	0.06048
A85	10.45875	-9.30194	0.05506
A957	153.41792	-0.91444	0.04500
IIZW108	318.48296	2.56539	0.04935
MKW3s	230.46625	7.70861	0.04472
RX0058	14.59432	26.86638	0.04700
RX1022	155.65584	38.57919	0.04910
Z2844	150.65223	32.70674	0.05000
Z8852	347.59333	7.58071	0.04000

2.2 WIYN 0.9m Telescope

The KPNO observatory is located at a high elevation and far from the nearest city of Tuscon. The distance from Tucson, and its strict by-laws regarding light pollution, makes KPNO a good site for conducting astronomical observations of faint objects. KPNO is also known for its good seeing, where seeing is a measurement of the blurriness of a star-like object (in terms of its point spread function) due to the Earth's atmosphere. The name of the telescope reflects the diameter of the primary mirror (0.9 m), and the field-of-view of the detector by the camera's name; Half Degree Imager (HDI). The HDI is a single chip, multi-amplifier imager with a field-of-view of 29.2 × 29.2 arcmin. To achieve a fast read-out time (15 s), the HDI uses four amplifiers. Table 2.6 lists properties of the HDI.[3]

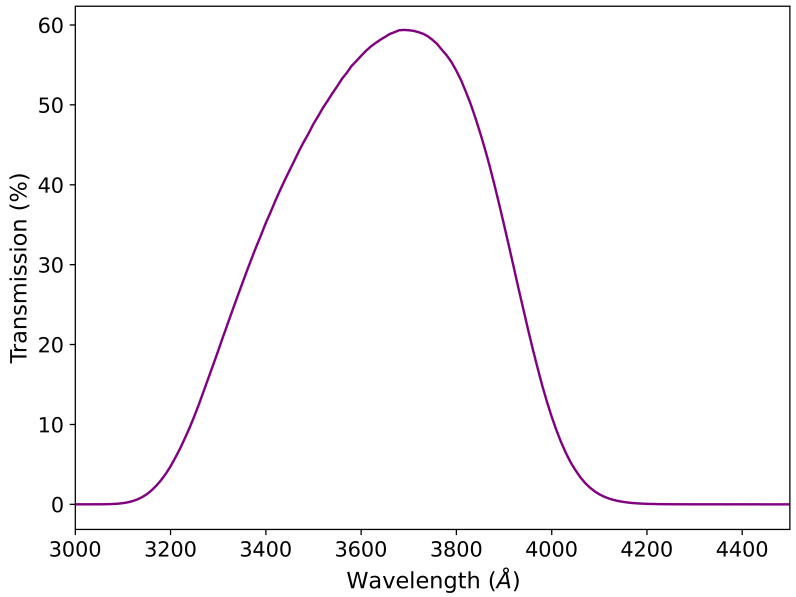

Figure 2.1: Filter transmission curve for the u-band filter at the KPNO/WIYN 0.9m telescope.[4]

[3] https://noirlab.edu/science/documents/scidoc1573
[4] https://noirlab.edu/science/documents/wy001

Table 2.6: Properties of the HDI.

Image Size	4096×4112 pixels
Pixel Size	$15\mu m \times 15\mu m$
Pixel Scale	0.428 arcsec/pixel
Read Noise	5 e^-
Dark Current	$< 5e^-$/pixel/hour (at -100 °C)
Gain	1.3 e/ADU
Linearity	Up to the saturation level
Saturation Level	$35,000$ e^-

The WIYN 0.9m+HDI telescope/detector was used in March 2017, November 2017, and November 2018 to obtain deep u-band (Fig. 2.1) observations of 14 low-redshift galaxy clusters (Table 2.1). Fifteen nights were awarded in total and four nights were lost due to technical problems and bad weather. The average seeing for combined observations was $1.5''$. The total integration time for each cluster was divided into 900 sec dithered exposures in order to minimize saturation effects, and correct for bad pixels and cosmic rays.

In addition to cluster images, several calibration exposures were acquired for each night. These consist of bias and flat field exposures. Eleven bias frames were taken for each night using zero-second exposures (i.e. the camera's shutter remains closed and the CCD is simply read out by the amplifiers). Nine u-band 'dome flats' – short exposure of an illuminated white screen inside the observatory dome – were taken for each night with a 15 second integration time. Due to the low dark current, no dark current frames were obtained. The importance of these calibration frames is discussed in the data reduction section of Chapter III.

2.3 Sloan Digital Sky Survey

The Sloan Digital Sky Survey is the largest and most successful astronomical survey that was established to construct a map of the local Universe. The survey is performed using a dedicated 2.5 m telescope located at the Apache Point Observatory, New Mexico. It is equipped with a CCD imaging camera and two multi-fiber spectrographs (Gunn et al., 1998; York et al., 2000).

The SDSS is designed to observe in five color bands; u', g', r', i', and z', simultaneously (Fig:2.2). The effective wavelength of each passband is 3550, 4770, 6230, 7620, and 9130 Å, respectively (Fukugita et al., 1996). The imaging camera contains 30 CCDs, arranged in six columns and five rows. Each CCD contains a 2048×2048 array of 24 μm pixels and each row observes the sky through a different filter. The camera operates in a drift-scan mode, i.e., a given point on the sky passes through each filter in succession, spending about 55 seconds in each filter (Gunn et al., 1998).

Once reduced and calibrated, imaging data is used for spectroscopic target selection. Each SDSS spectrograph utilizes a dual-channel design with a dichroic splitting the beam into a blue (3800 - 6100 Å) and a red channel (5900 - 9100 Å). Each channel is assigned to a separate CCD (Smee et al., 2013). The number and the size of optical fibers used in each spectrograph will vary with the survey.[5] For example, the Baryon Oscillation Spectroscopic Survey (BOSS) uses an aluminum plate with a thousand holes (each hole represents an astronomical object or sky background) with an optical fiber of $2''$ diameter plugged into each hole.

The 'CrossID' tool of the SDSS DR16 was used to obtain SDSS data for my cluster sample.[6] For each object, a search radius of three arcseconds was used to compensate for small World Coordinate System (WCS; see section 3.1.3) offsets. The "Nearest Primary Object" option was used to select measurements of the closest

[5] https://www.sdss.org/dr14/instruments/

[6] http://skyserver.sdss.org/dr16/en/tools/crossid/crossid.aspx

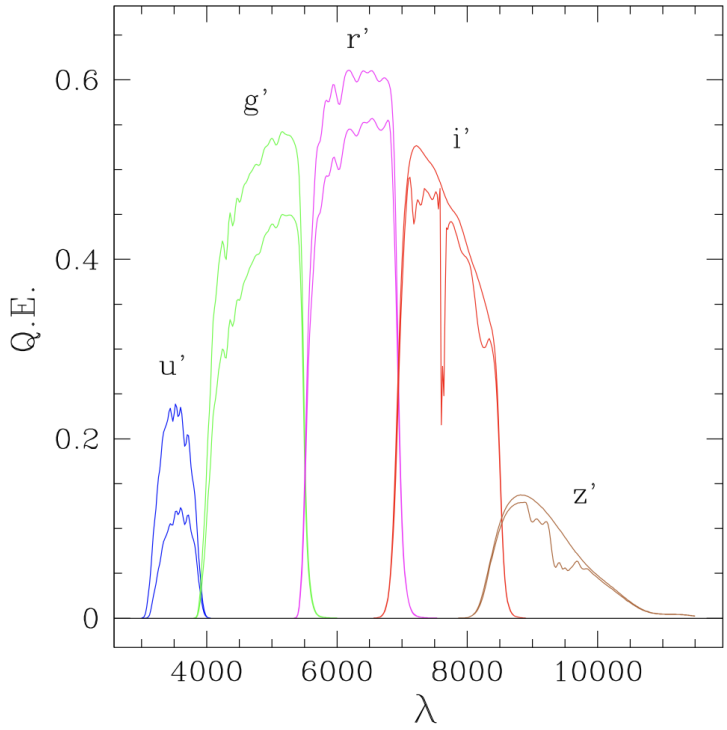

Figure 2.2: System quantum efficiency for each filter system in the SDSS. The responses are shown without atmospheric extinction (upper curves) and as modified by the expected atmospheric extinction associated with 1.2 air masses at the SDSS site (Gunn et al., 1998).

positional match. On average, 3 arcseconds is equal to 2 × the average Full Width Half Maximum (FWHM) of KPNO u-band data, which is ∼ 1.5 arcseconds (or ∼ 3.5 pixels, calculated using the pixel scale of the HDI).

2.4 Galaxy Evolution Explorer

The Galaxy Evolution Explorer (GALEX) was a NASA Small Explorer mission launched with the primary goal of studying the star formation in galaxies and its evolution with time. GALEX was the first all-sky imaging and spectroscopic survey at UV wavelengths (1350 - 2750 Å). The wavelength range was divided into two passbands: far-UV or FUV (1350 - 1750 Å) and near-UV or NUV (1750 - 2750 Å)

(Martin et al., 2005).

GALEX used a 50 cm modified Ritchey-Chrétien telescope with 1.25° field of view.[7] The FUV and NUV observations were obtained simultaneously using a dichroic beam splitter. The two detectors incorporated sealed tube microchannel plate detectors with a 65 mm active area, a photocathode, and a delay-line anode to determine photon position. A blue-edge filter was used to block airglow emission lines, such as Lyman-α (1216 Å), from the FUV channel, while a red blocking filter was used to reduce contamination from zodiacal light in the NUV channel (Morrissey et al., 2005). GALEX performed all-sky surveys with different depths and coverage, with All-sky Imaging, Medium Imaging, Deep Imaging, and Nearby Galaxy being the principal imaging surveys.

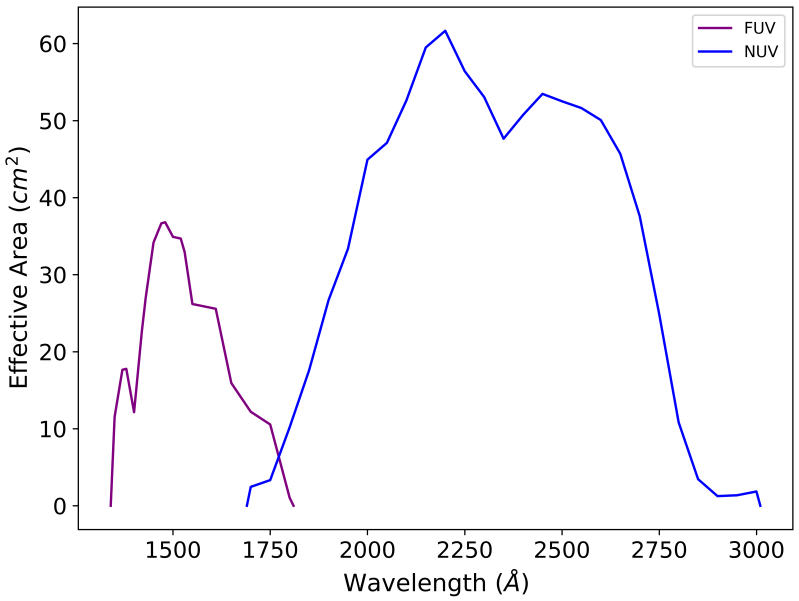

Figure 2.3: Effective area vs. wavelength for GALEX filters in imaging mode.[8]

Both FUV and NUV passband data from GALEX were acquired from the Multi-Mission Archive at the Space Telescope Science Institute (MAST)[9], using a three

[7] https://archive.stsci.edu/missions-and-data/galex
[8] https://asd.gsfc.nasa.gov/archive/galex/tools/Resolution_Response/index.html
[9] https://mast.stsci.edu/portal/Mashup/Clients/Mast/Portal.html

arcseconds search radius for each object. When the same object was observed in multiple surveys, measurements with the smallest magnitude error were used in this study.

2.5 Wide-field Infrared Survey Explorer

The Wide-field Infrared Survey Explorer (WISE) is a NASA medium-class explorer mission that is designed to map the sky in four infrared bands W1, W2, W3, W4 centered at 3.4, 4.6, 12, and 22 μm wavelengths. The telescope used in WISE has a diameter of 40 cm, with a 47 arcminute field of view. During the initial all-sky survey, 7 January 2010 to 6 August 2010, WISE instruments were cryogenically cooled using solid hydrogen to avoid instrumental thermal radiation detections. Light from each passband is measured using focal plane arrays of 1024 $\times$ 1024 pixels. WISE image resolution is about six arcseconds in the W1, W2, W3 passbands and 12 arcseconds in W4 passband (Wright et al., 2010).

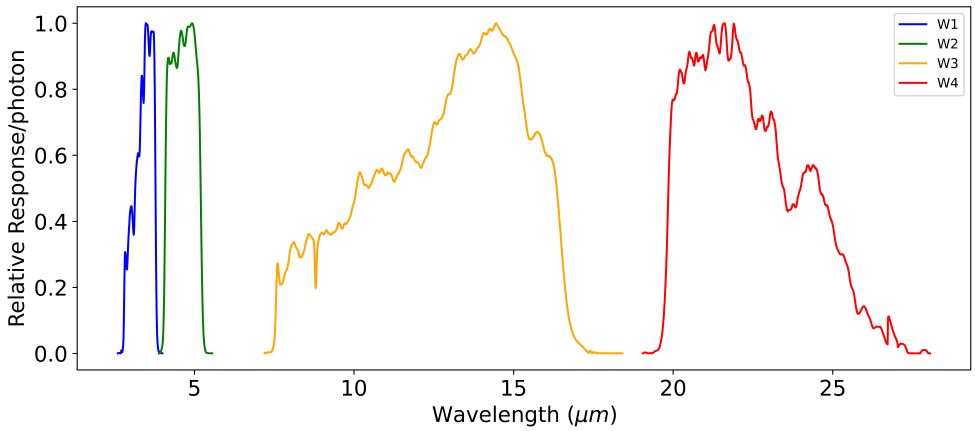

Figure 2.4: The WISE passband filter response per photon (Wright et al., 2010).

The 'ALLWISE Source Catalog', accessible through the NASA/IPAC Infrared Science Archive, was used to obtain W1, W2, W3, and W4 passband data for all

cluster galaxies.[10] A search radius of three arcseconds was used to compensate for minor WCS offsets. The "One to One Match" option was used to select measurements of the closest positional match.

[10] https://irsa.ipac.caltech.edu/

Chapter III

DATA REDUCTION AND PHOTOMETRIC MEASUREMENTS

3.1 Data Reduction

Images from the WIYN 0.9m telescope are stored as single extension Flexible Image Transportation System (FITS) files. The FITS format is a standard file format used at most professional observatories. This format allows data to be stored, transmitted, and processed as N-dimensional arrays (e.g. a 2D image). The ASCII header of a FITS image contains a series of keywords that describes the data (e.g. right ascension, declination, exposure time, filter details, etc.).

Before astrometric and photometric calibrations, the imaging data requires pre-processing to remove electronic bias levels and correct for pixel-to-pixel sensitivity variations across the detector. For WIYN 0.9m data, the Image Reduction and Analysis Facility (IRAF) software was used for image pre-processing.

3.1.1 Bias and Flat Field Calibrations

Bias frames, or zero-second exposure frames, are used to correct for artificially induced electronic bias levels. A 2D pixel-by-pixel subtraction is required to remove this electronic "noise" from each science image (Howell, 2006). Since a single bias frame does not adequately sample the electronic bias offset without introducing non-negligible statistical noise, an average 'master' bias was created for each observing

night using eleven individual bias frames.

Flat-field exposures were used to correct for wavelength-dependent pixel-to-pixel variations of the CCD response as well as any nonuniform illumination of the detector itself (Howell, 2006). Each science image was divided by a nightly average 'master' flat-field frame made from nine u-band dome flats to ensure a high signal-to-noise ratio without exceeding the saturation limit or non-linearity of the CCD.

The `CCDPROC` task in IRAF was used for these calibration steps. No correction was made to remove dark current since it is less than 5 electrons/pixel/hour and thus has a negligible impact on measurements of object brightness.

3.1.2 Image Stacking

Before combining all exposures to make a final cluster image, individual exposures were shifted to a common reference coordinate system. The `IMALIGN` and `IMCOMBINE` tasks in IRAF were used to align and combine images, respectively. All final cluster images were checked thoroughly for signs of double objects to ensure images were properly aligned and stacked. The final u-band cluster images are shown in Figs. 3.1 - 3.14.

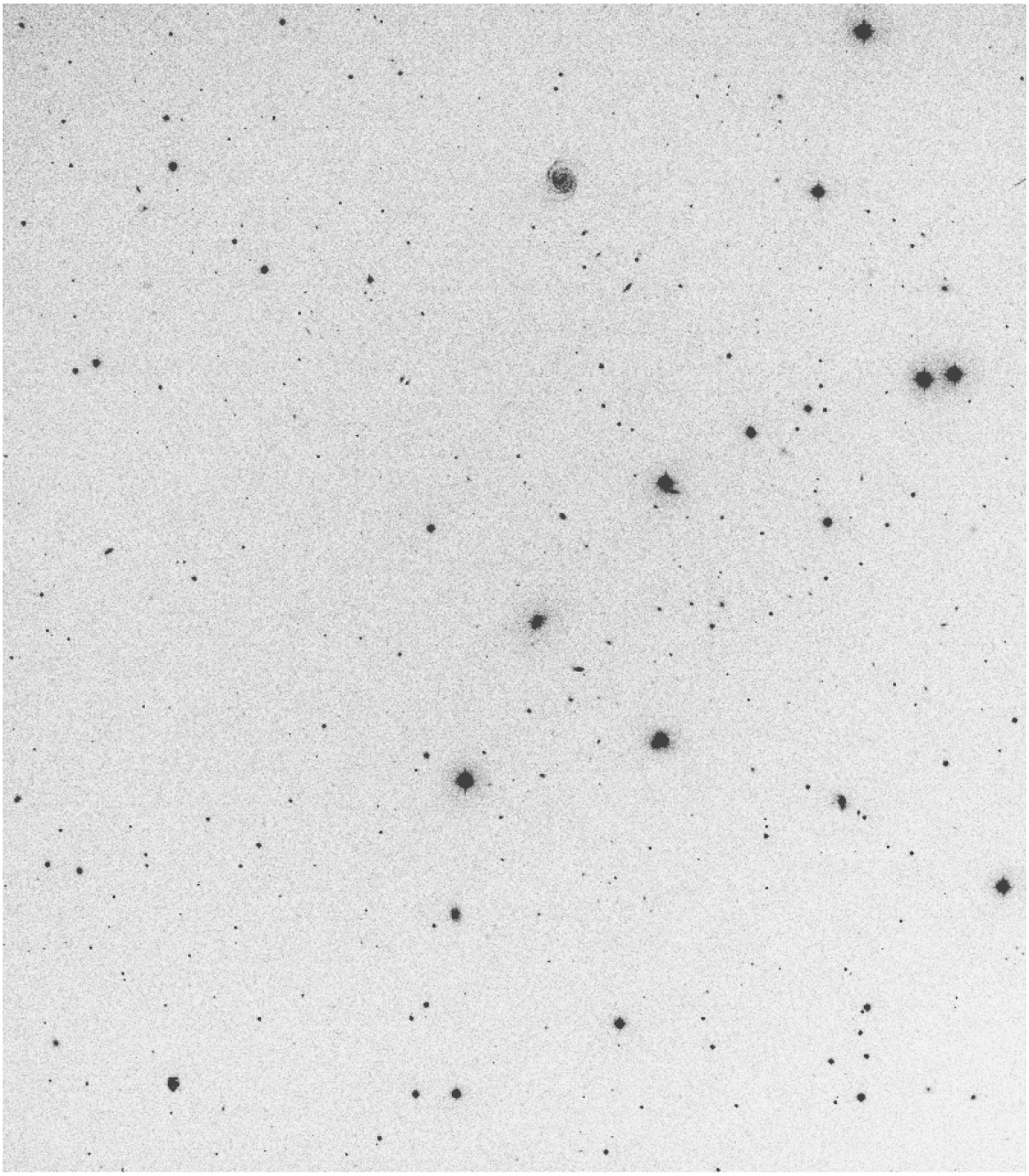

Figure 3.1: Combined u-band image of Abell 1142.

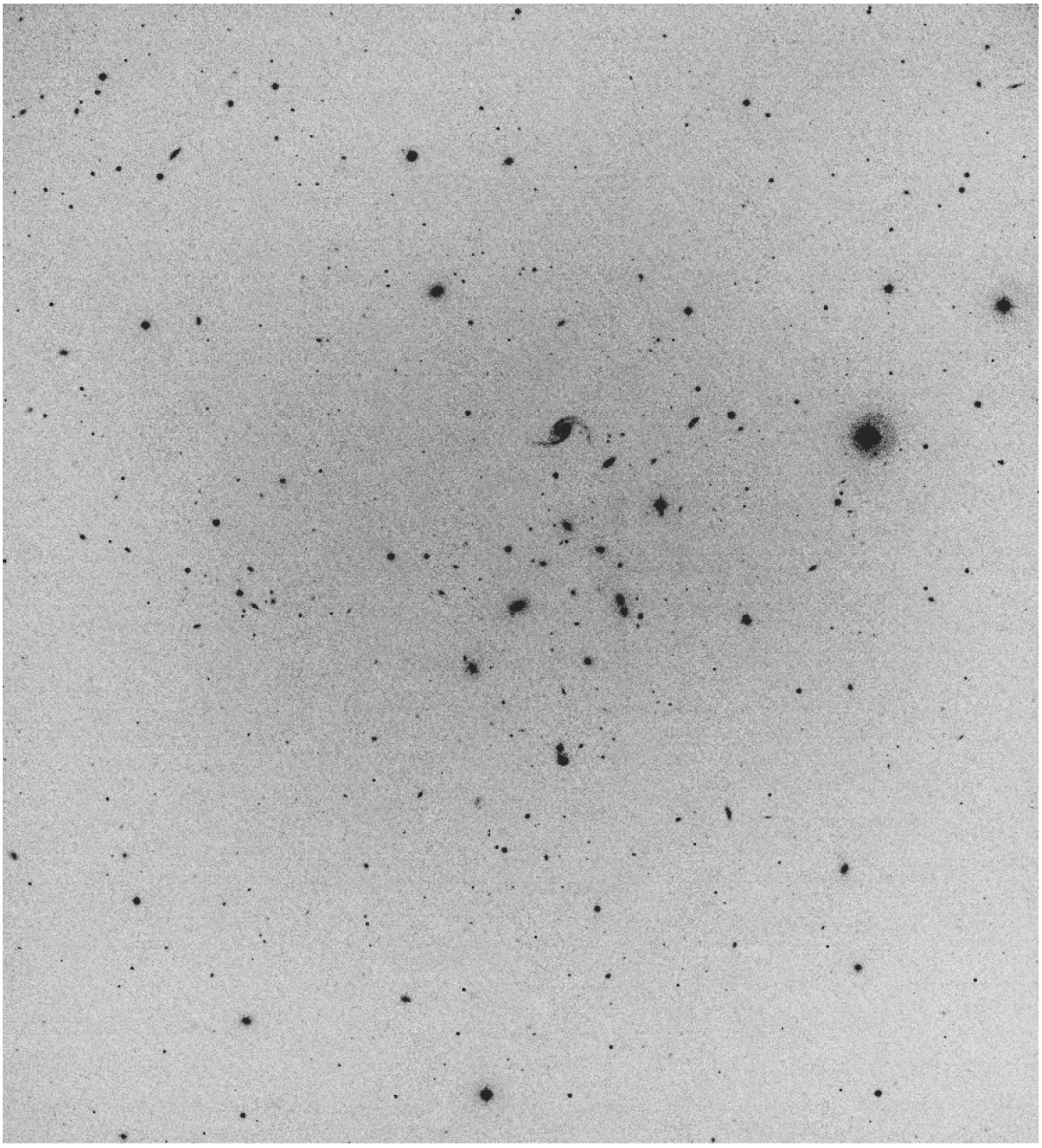

Figure 3.2: Combined u-band image of Abell 1213.

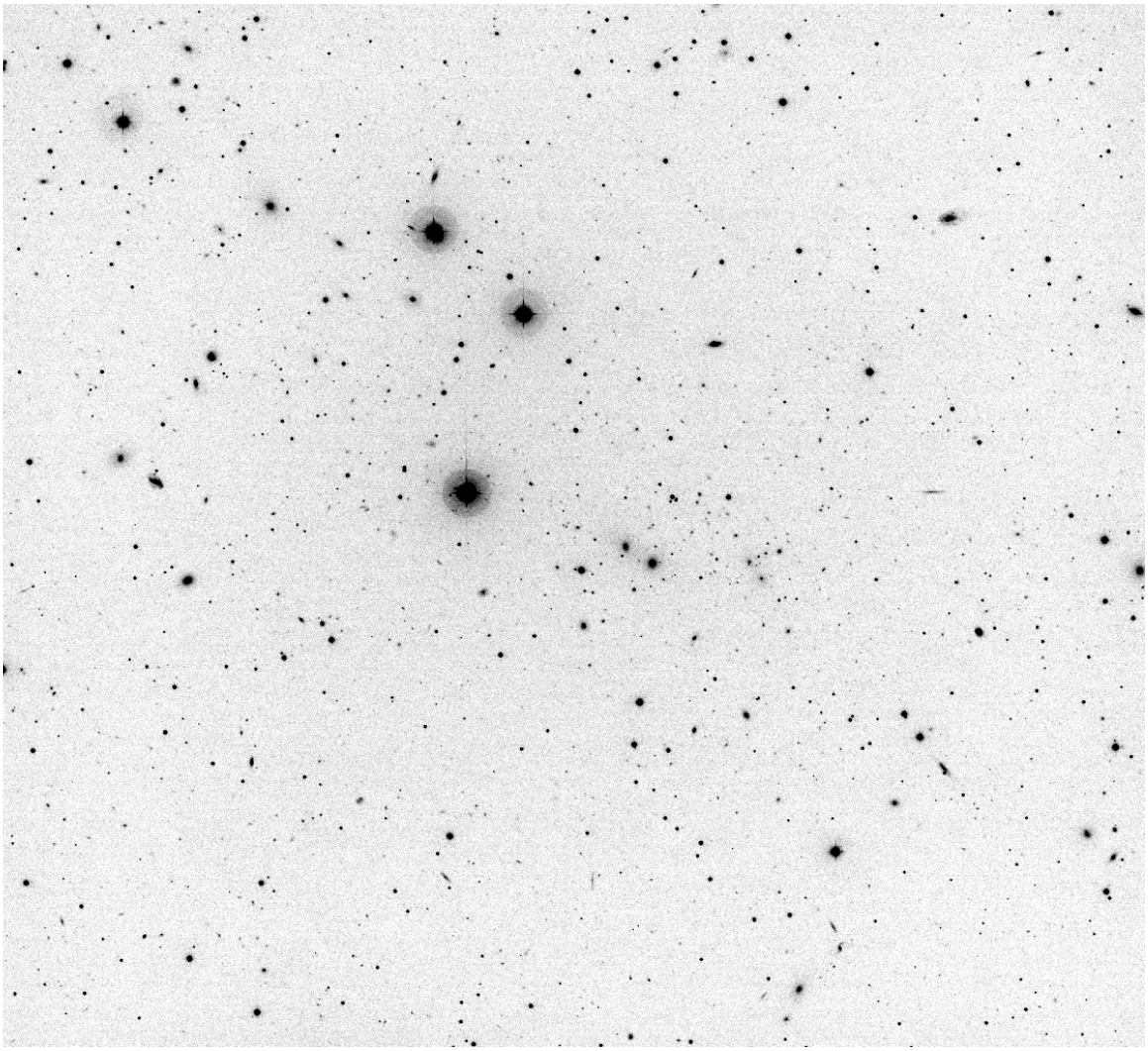

Figure 3.3: Combined u-band image of Abell 2152.

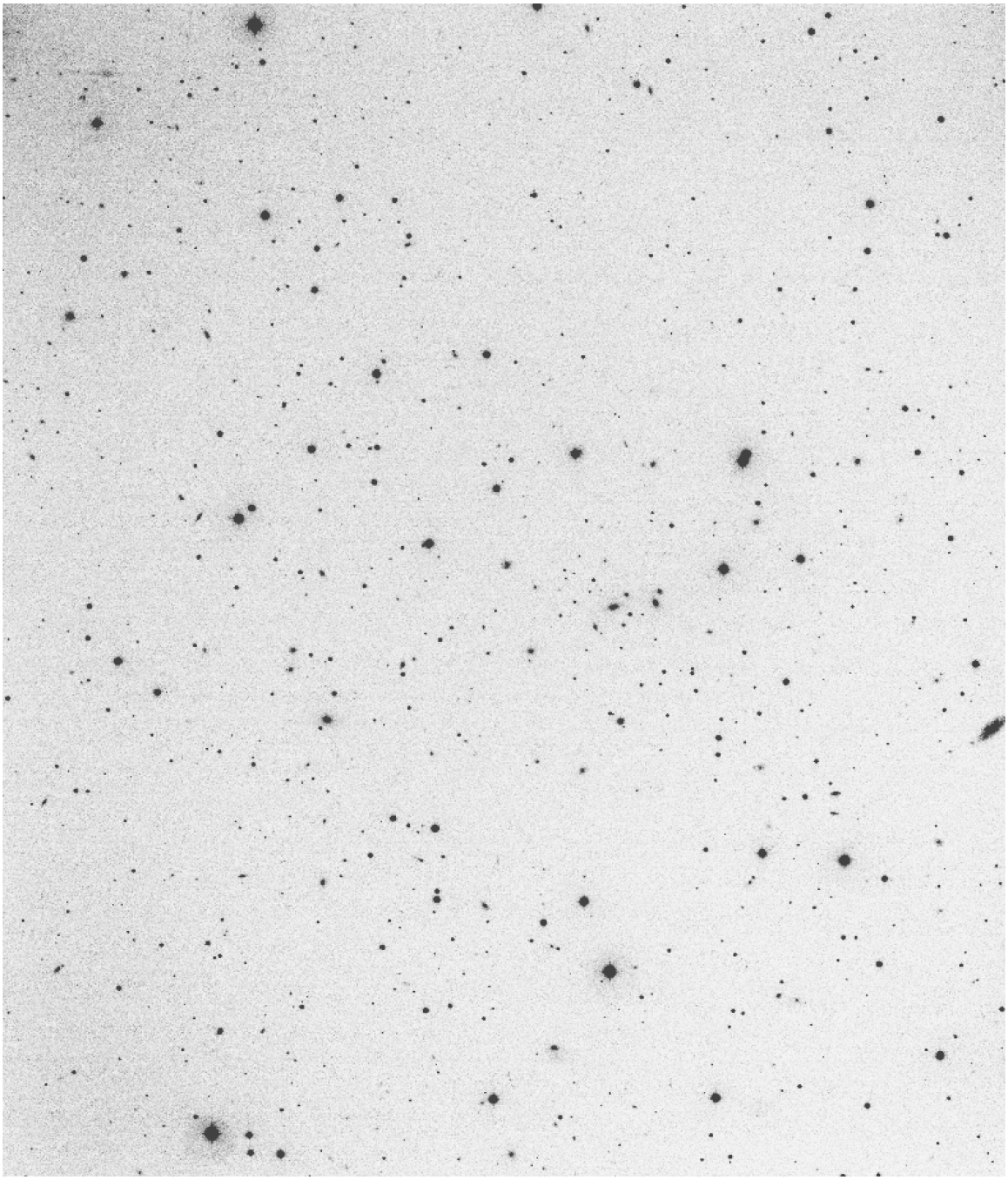

Figure 3.4: Combined u-band image of Abell 2399.

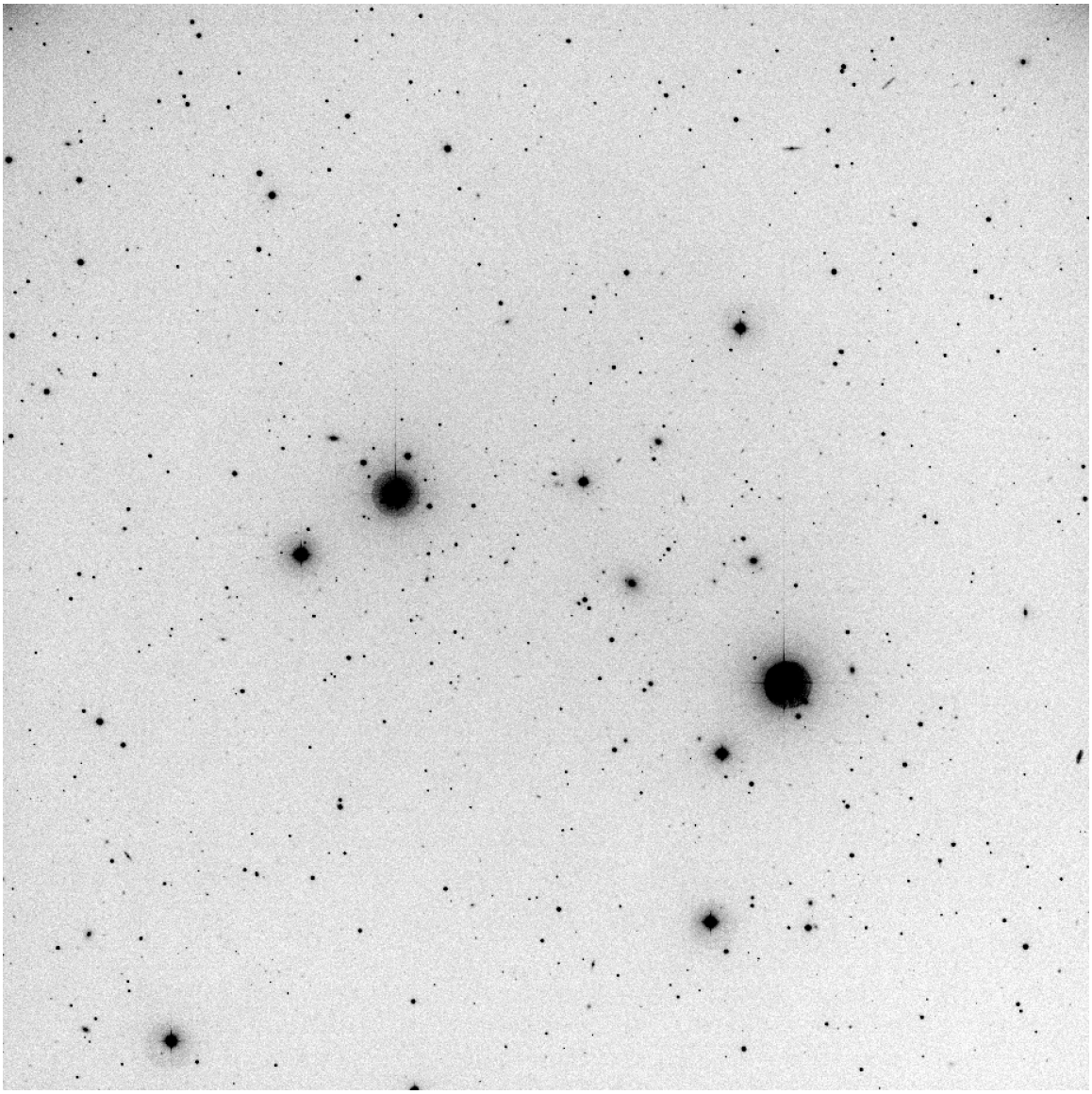

Figure 3.5: Combined u-band image of Abell 2572.

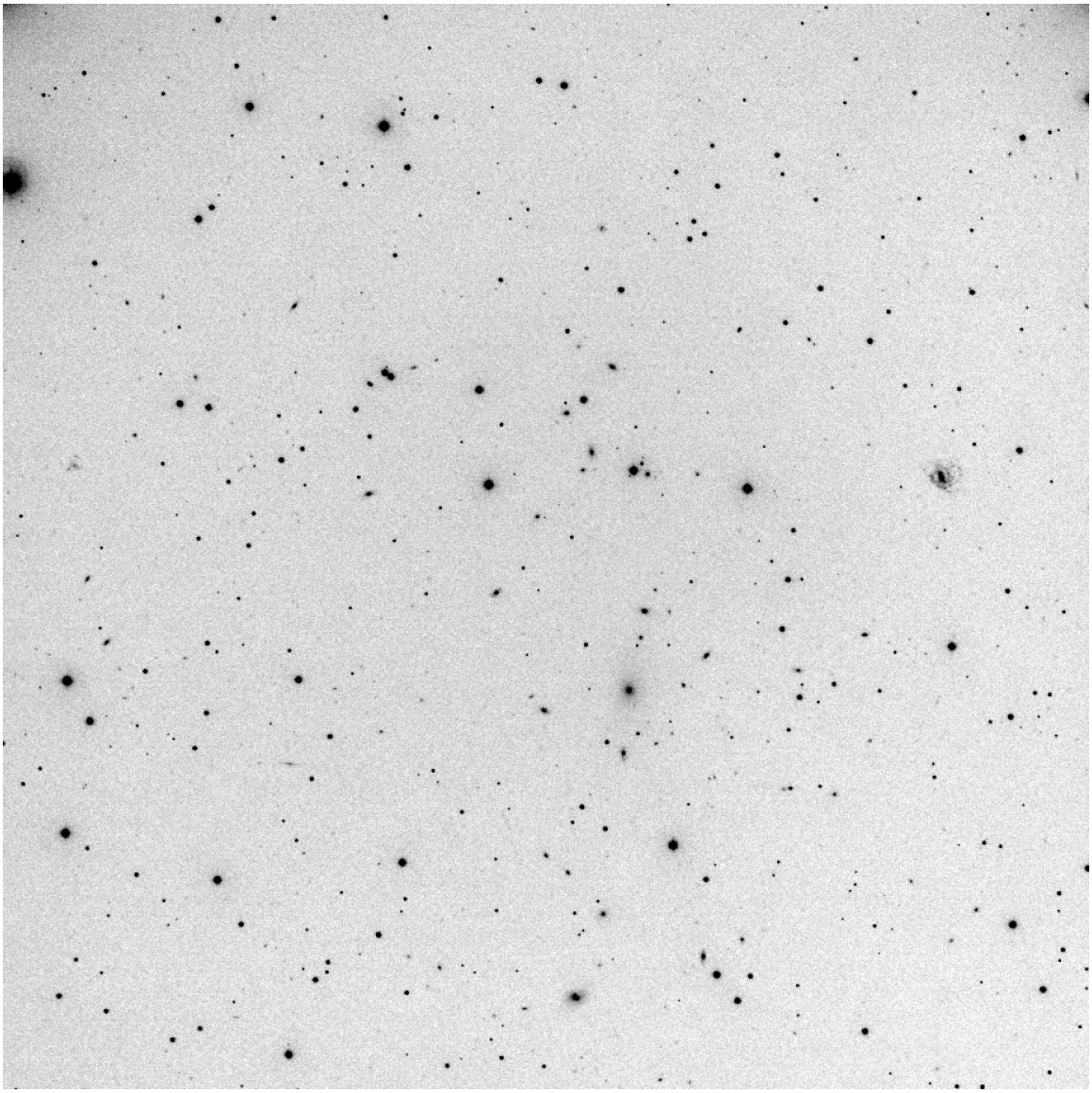

Figure 3.6: Combined u-band image of Abell 2589.

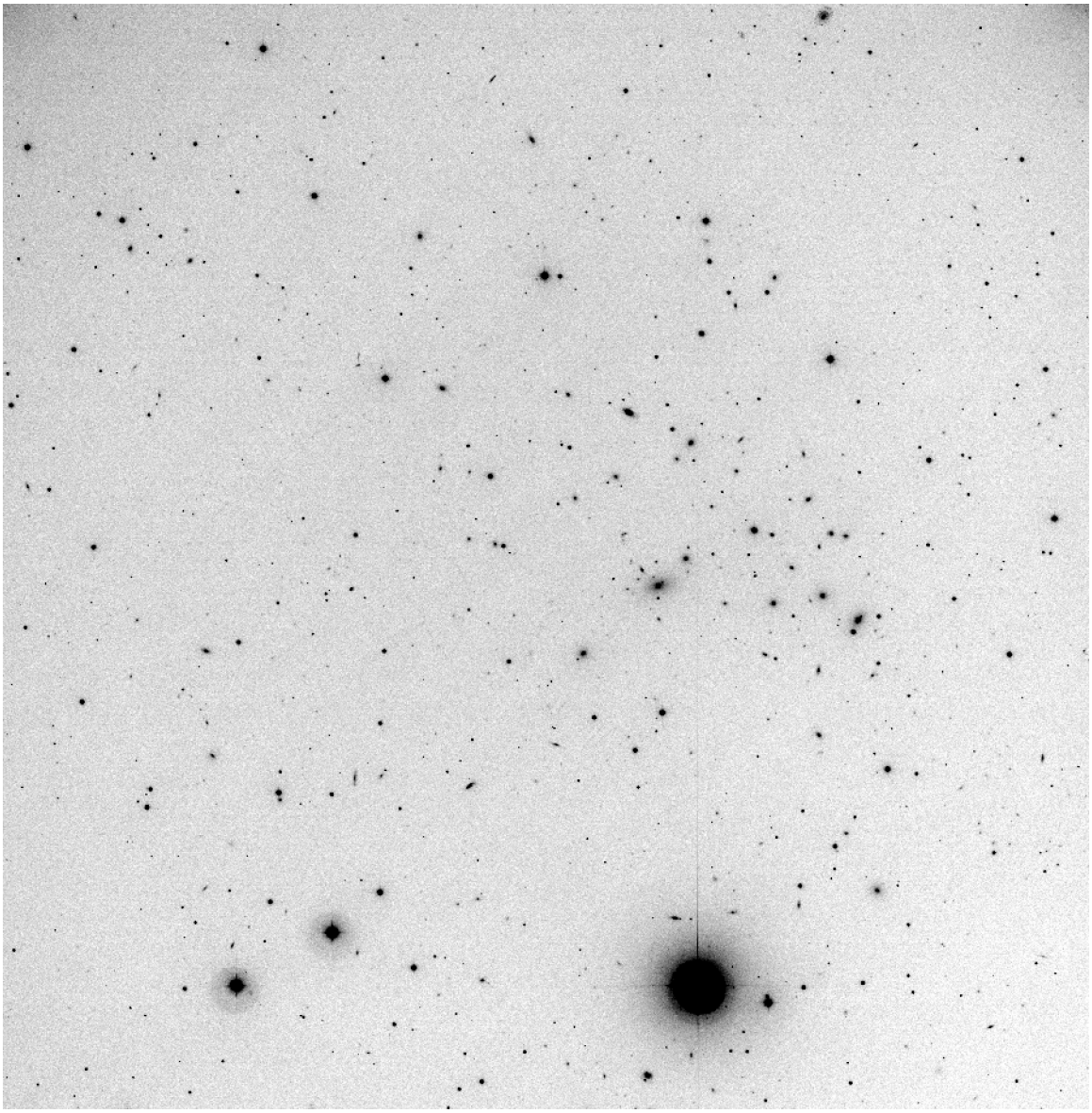

Figure 3.7: Combined u-band image of Abell 2593.

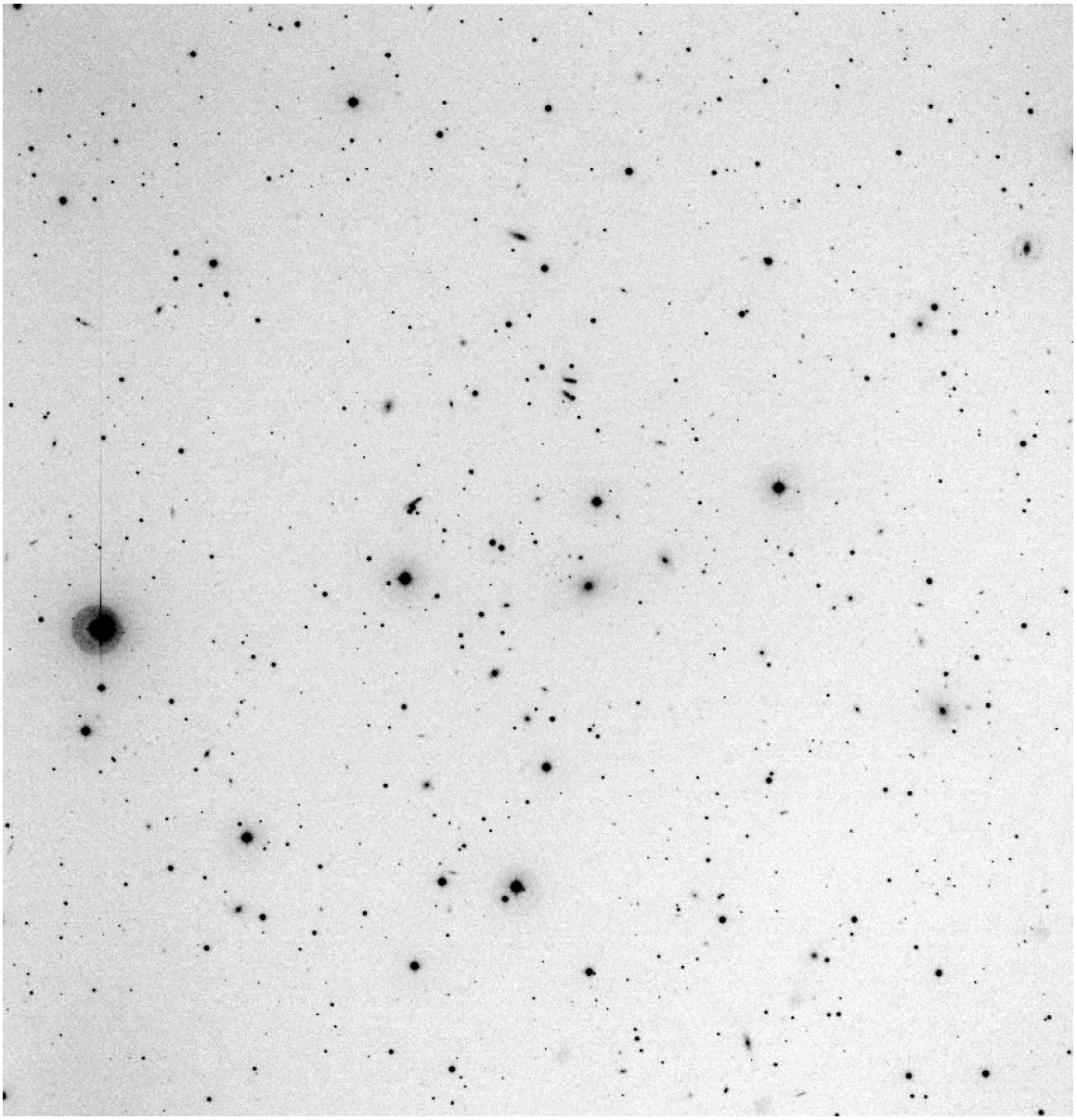

Figure 3.8: Combined u-band image of Abell 260.

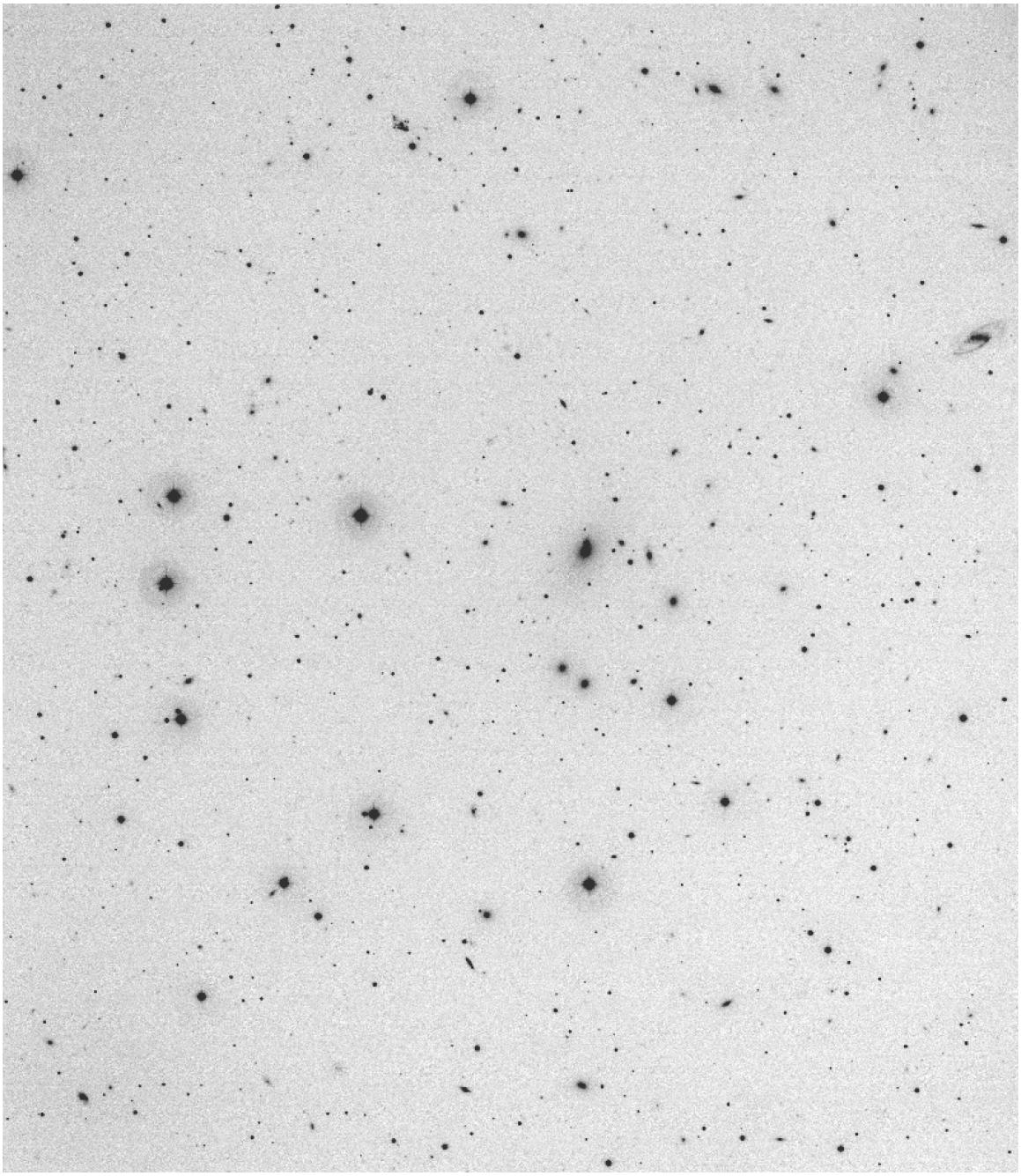

Figure 3.9: Combined u-band image of Abell 2634.

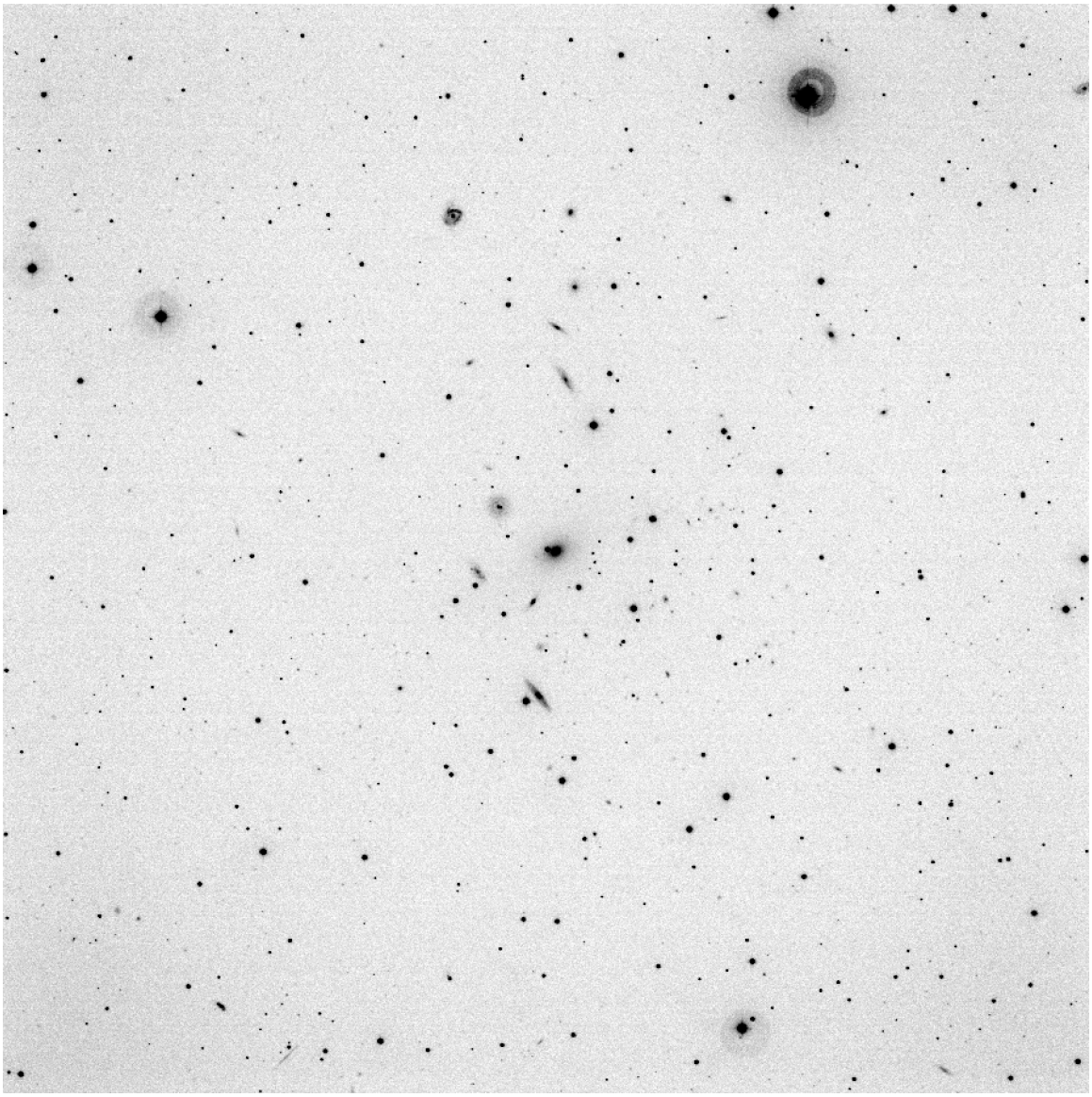

Figure 3.10: Combined u-band image of Abell 2666.

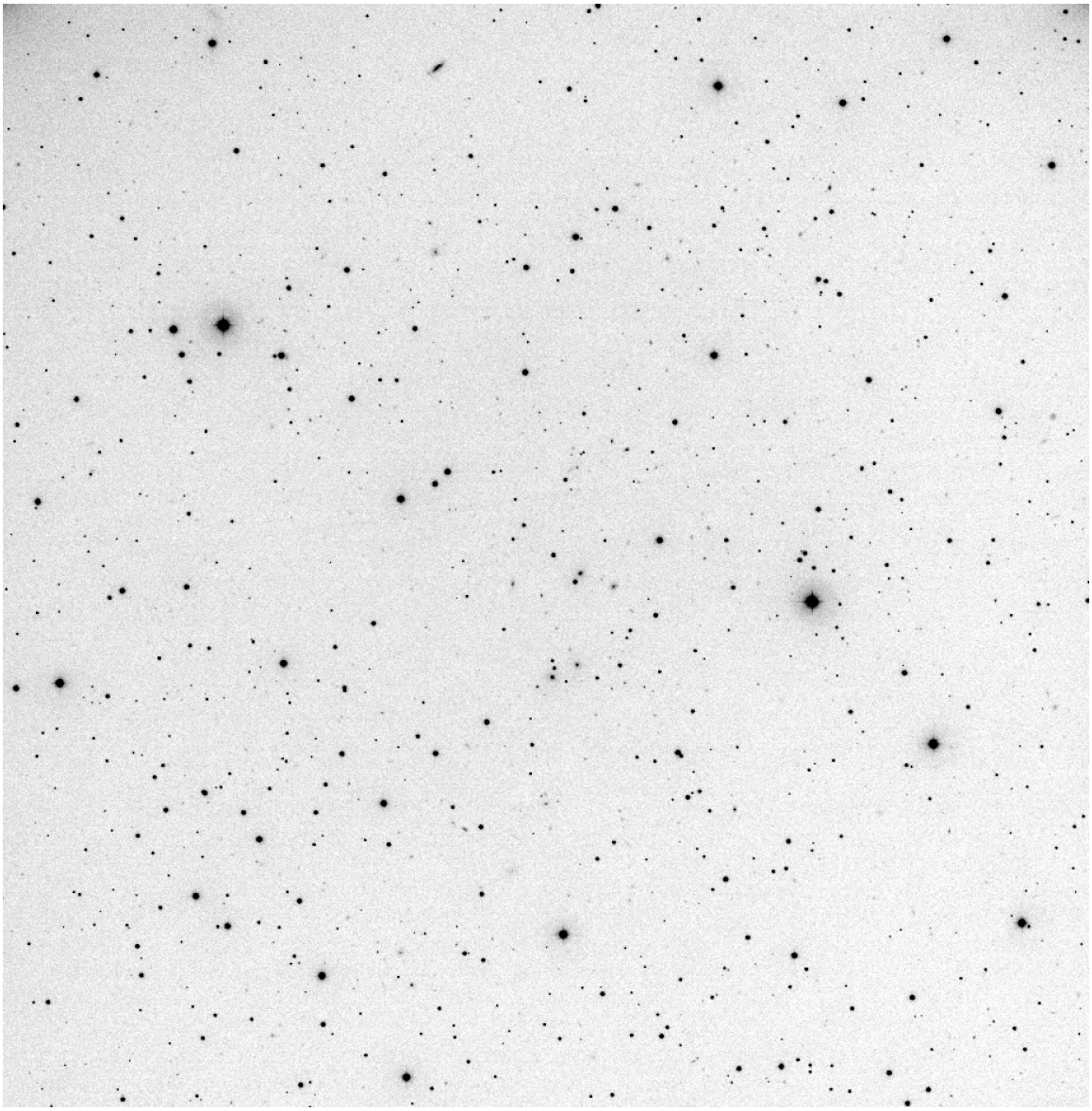

Figure 3.11: Combined u-band image of Abell 582.

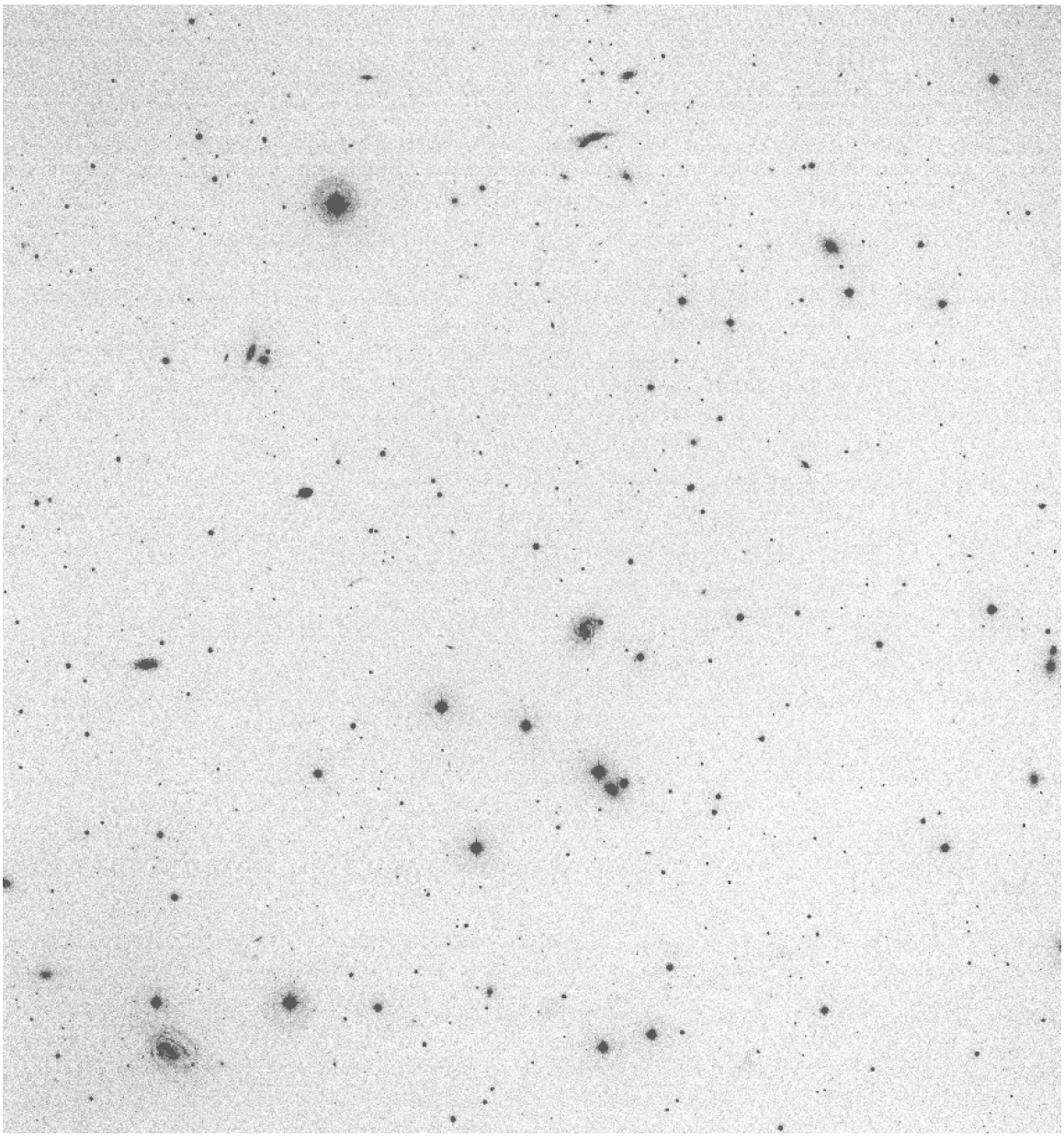

Figure 3.12: Combined u-band image of Abell 634.

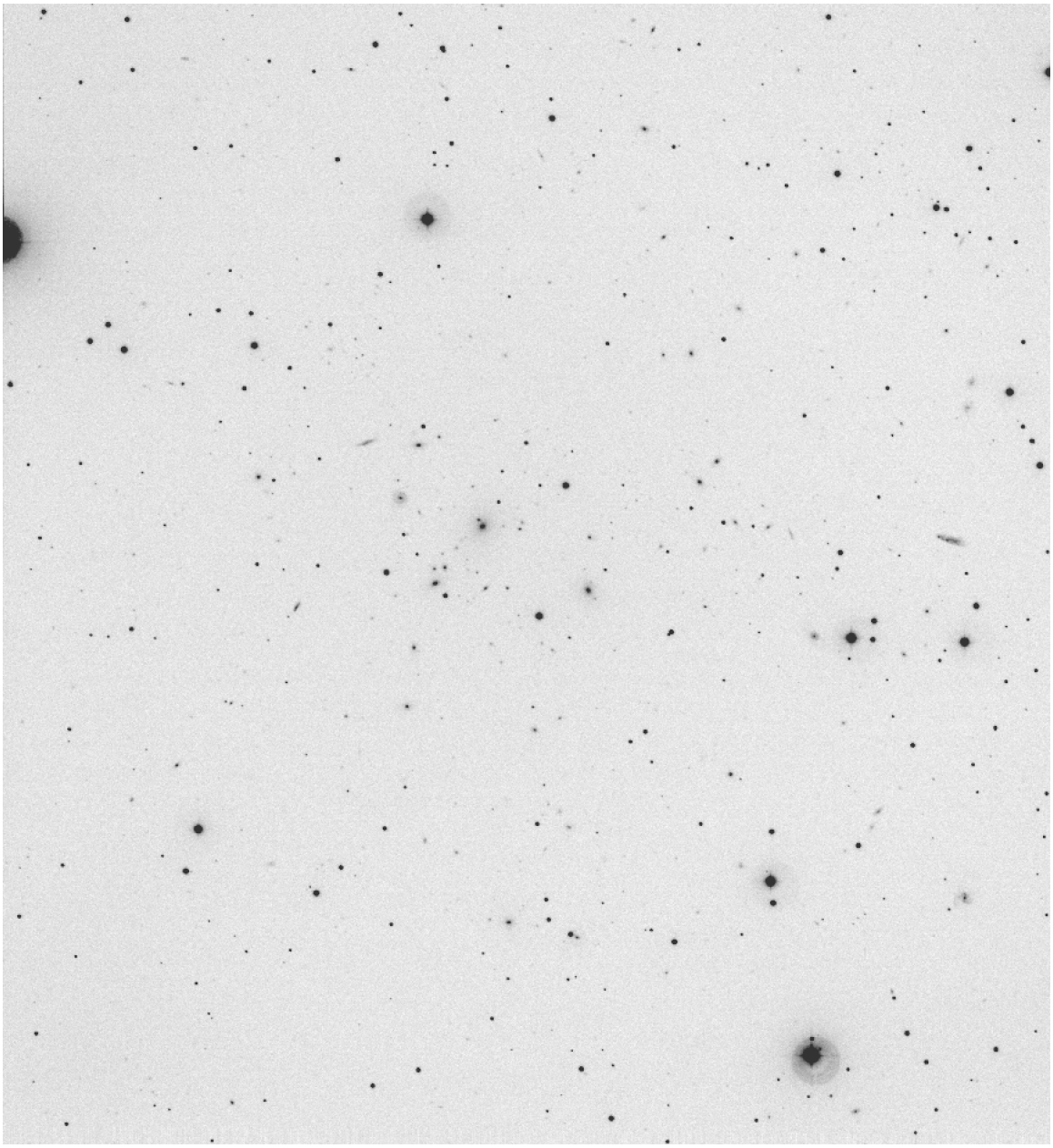

Figure 3.13: Combined u-band image of Abell 671.

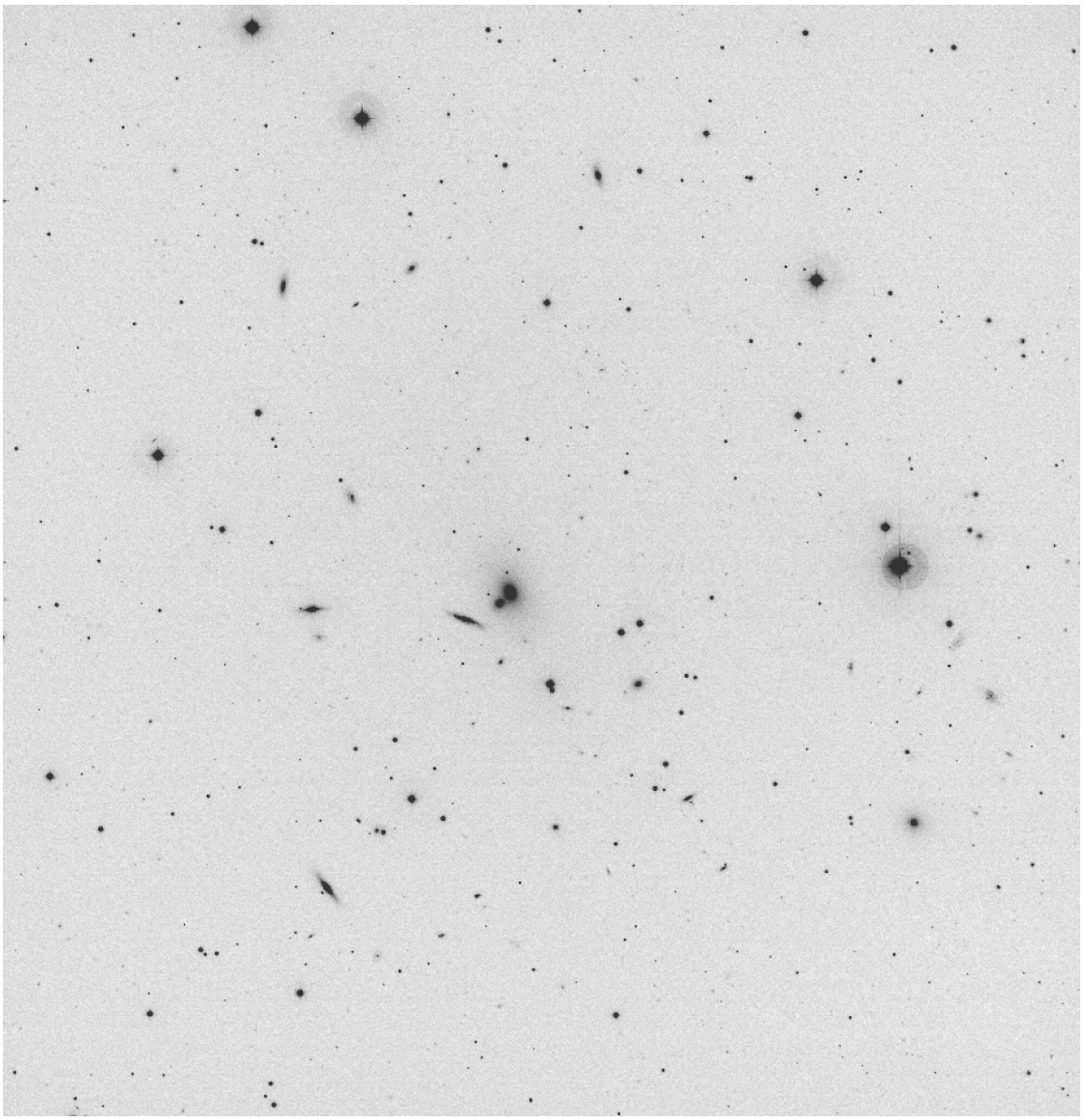

Figure 3.14: Combined u-band image of Abell 779.

3.1.3 Astrometric Calibration

The goal of the astrometric calibration is to generate parameters that are necessary to refine the World Coordinate System (WCS) by accurately mapping pixel coordinates to celestial coordinates (right ascension and declination).

After a successful calibration, WCS information will be stored in the image header using several keywords such as WCSDIM, CTYPE1, CTYPE2, CRPIX1, CRPIX2, CRVAL1, and CRVAL2. WCSDIM gives the dimensionality of the WCS and is equal to two for two-dimensional images. CTYPE1 and CTYPE2 are used to describe the projection used for the coordinate system. The projection describes how pixels in the images are mapped onto the sky. CRPIX1 and CRPIX2 specify the coordinates of the tangent point where the flat CCD surface is positioned on the celestial sphere, while CRVAL1 and CRVAL2 specify the corresponding coordinates on the celestial sphere.

A two-dimensional rotation matrix (R) describes how the CCD image is rotated relative to the axes of the celestial sphere

$$R = \begin{vmatrix} Cos\ \theta & -Sin\ \theta \\ Sin\ \theta & Cos\ \theta \end{vmatrix}, \tag{3.1}$$

and equation 3.2 describes the transformation of CCD pixel coordinates to celestial coordinates

$$a = sRu, \tag{3.2}$$

where $a = (\mathrm{RA} - \mathrm{CRVAL1}, \mathrm{DEC} - \mathrm{CRVAL2})$ and $u = (\mathrm{x} - \mathrm{CRPIX1}, \mathrm{y} - \mathrm{CRPIX2})$. a and u are vectors of the celestial and pixel coordinates relative to the tangent point. s is the angular size of a pixel and R is the rotation of the CCD image relative to

celestial North.[1]

To generate these WCS parameters, each final cluster image was compared with a reference catalog (e.g. USNO-A 2.0) using the DS9 image displayer to match pixel coordinates of, on average, 50 randomly selected, unsaturated stars in the image with their celestial coordinates from the reference catalog. To ensure an accurate WCS solution, it was important to select objects that were distributed over the whole image. Then the `CCMAP` and `CCSETWCS` tasks in IRAF were used to calculate and apply the WCS calibration to the image, respectively.[2]

3.2 Brightest Cluster Galaxy Modeling

In many clusters, there is a dominant, massive galaxy located at the bottom of the cluster gravitational potential well, known as a Brightest Cluster Galaxy. A BCG is mostly a giant elliptical galaxy with an extended halo, named a 'cD' type galaxy. On average, BCGs are surrounded by several other cluster galaxies. Some of these galaxies overlap the extended halo light of the BCG. To accurately measure the magnitude of these galaxies, the BCG and its halo were modeled and subtracted from the parent image. The location of the BCG was obtained by visually inspecting the cluster image, and confirmed by comparing its location with the X-ray centroid of the cluster (Piffaretti et al., 2011). Then the `ELLIPSE` and `BMODEL` tasks in the `STADAS` package of IRAF were used to model the BCG and `IMARITH` was used to subtract the model from the parent image (Jedrzejewski, 1987).

[1] `http://astro.physics.uiowa.edu/~kaaret/2015f_a4850/Lab06_astrometry.html`
[2] `https://lizwehner.wordpress.com/2008/02/13/adding-a-wcs-to-your-fits-image/`

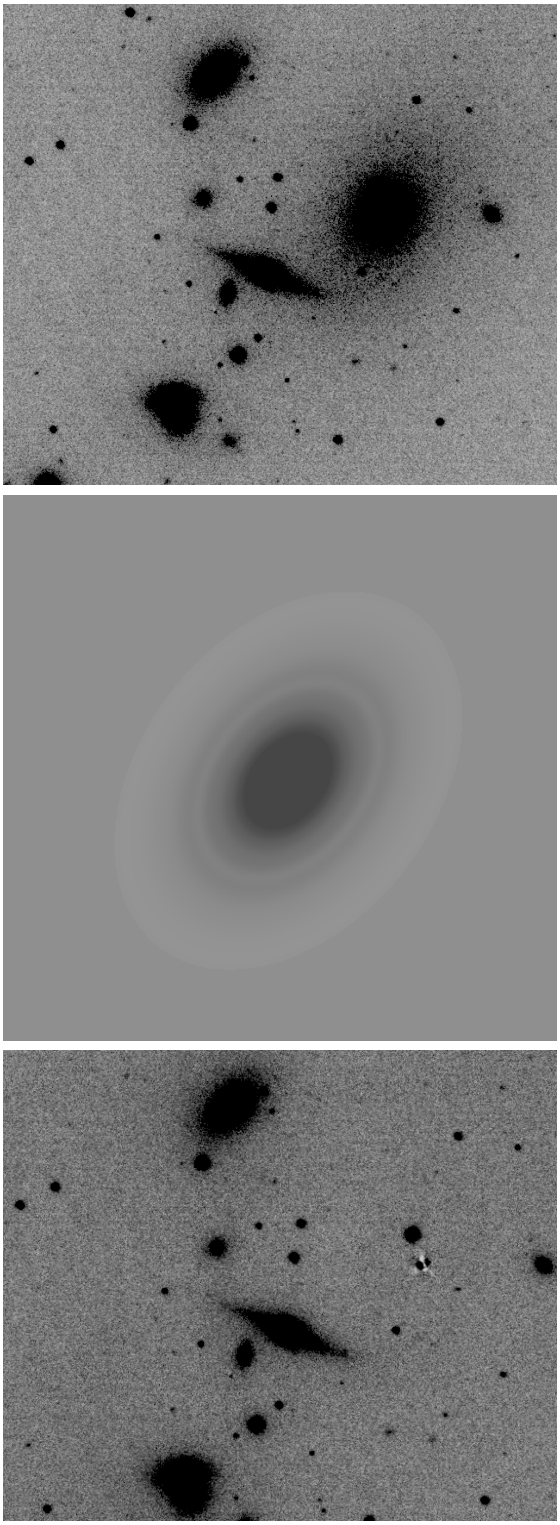

Figure 3.15: The top panel depicts the original cluster image with the BCG (right of center). The middle panel displays the BCG model produced by the `ELLIPSE` and `BMODEL` tasks. The bottom panel shows the BCG-subtracted cluster image.

3.3 Photometry

The Picture Processing Package (PPP) was used as the primary tool for conducting photometric measurements for KPNO u-band data. PPP is a command-based interactive image analysis system that reads FITS files, detects all objects in an image, classifies them into stars and galaxies, and measures instrumental magnitudes (Yee, 1991).

3.3.1 Object Detection

The main object identification routine in PPP works by searching for local maxima in pixel brightness. The first step in object detection using PPP is to smooth the cluster image using a tapered box car filter to reduce the noise level of the background sky. Then, PPP iterates through all the local maximum pixel values and measures the net flux from nine contiguous pixels centered on the peak. The local sky value is derived from the mode of the distribution of pixel values from pixels within a ring around the local maximum with inner and outer radii of five and eleven pixels, respectively. If the object flux is larger than a chosen threshold, it is considered a detection and the integer value of the coordinates of the local maximum is recorded to an object position file. The local sky value is estimated from the mean and median of pixel values within a defined annulus using (Yee, 1991)

$$sky\ value = 2 * median - mean. \tag{3.3}$$

These parameter settings are based on extensive simulations described in Yee (1991).

As a final check, the object position file was overlaid on the image to manually check for false detections, such as bleeding trails from saturated objects, and missed objects near bright stars and galaxies (Fig. 3.16).

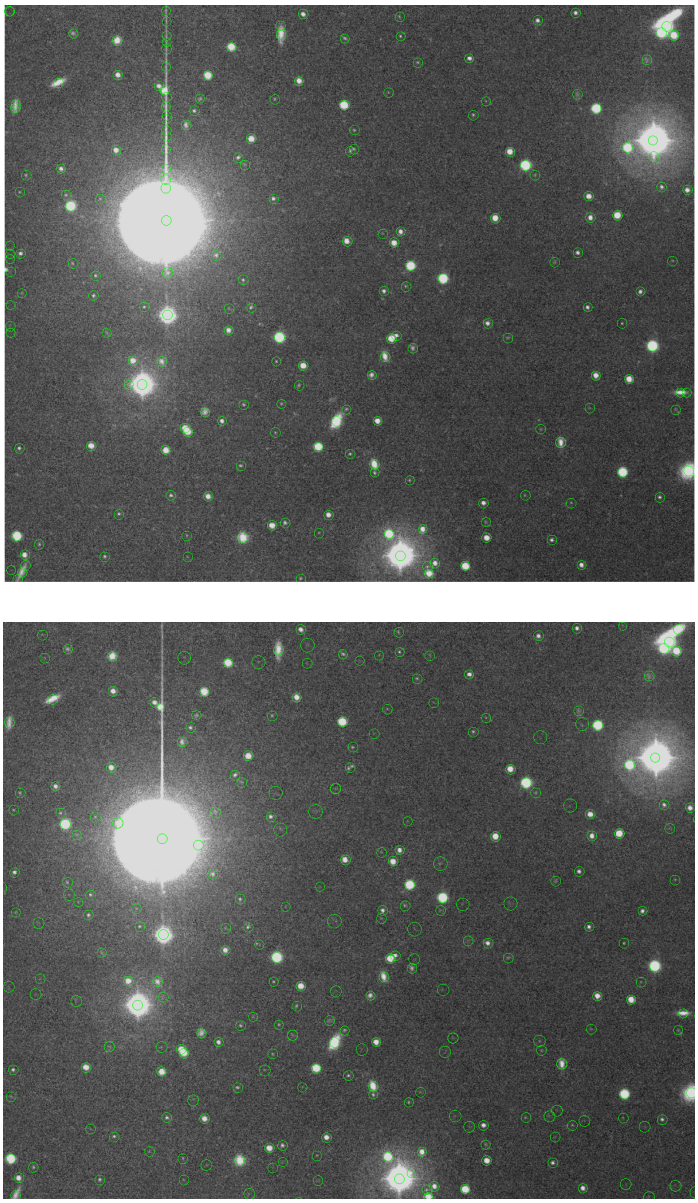

Figure 3.16: A region of a cluster image showing initial detections from PPP (top) and after cleaning for false detections and adding missing objects (bottom).

3.3.2 Photometry in Crowded Fields

Galaxies, even at higher redshifts, usually extend to a size of several arc seconds, and unlike stars, do not have a similar size or shape. In addition, galaxy cluster images are crowded fields (i.e. overlapping galaxies) due to their very own high-density nature.

Thus, an elaborate method is required to measure the total flux of a galaxy in a cluster image. PPP address both of these problems by constructing and analyzing the flux growth curve of an object to perform photometry.

The first step of deriving the growth curve is computing an accurate centroid for each object. An accurate centroid is important since the shape of the growth curve, which is used for classification purposes, can be significantly affected by the choice of the centroid. First, an intensity weighted centroid is computed using a small aperture, typically 1 (or 1.5) FWHM in diameter centered on the integer pixel position. Then the flux contributed by a pixel that is cut by the boundary of the aperture is computed according to the fraction of the pixel that is inside the aperture. This process is repeated with the aperture centered on the last estimated fractional pixel centroid until the X,Y coordinates converge (Yee, 1991). This will ensure a high accurate centroid.

The next step is to create a series of apertures around the centroid to create the growth curve. In order to ensure that light from surrounding objects is not contributing to the flux, all objects that are within twice the radius of the maximum allowable aperture are masked. The master position file was used to determine the candidates for masking. A minimum that is on the line between the neighbor and the object of interest is located. Then a circular mask is created, centered on the neighboring object, with a radius equal to the above minimum plus a predefined additional number of pixels.

After all neighboring objects have been masked, a series of circular concentric apertures, centered on the centroid, are created out to a specified maximum diameter with an increment in diameter of two pixels for successive apertures. Then the growth curve is computed by summing the pixel flux values within each aperture. Circular symmetry was assumed to compensate for the masked area. Although this assumption is ideal for bright disk-like galaxies, in a statistical sense, averaged over a large number

of objects, it should be free of any systematic effects.

The shape of the curve is used to find the optimum diameter/aperture to measure the flux of an object. Each growth curve was examined for deviations from a "normal" object – i.e., one that has a monotonically increasing flux and monotonically decreasing first derivative, and the smallest of the following was considered as the optimal diameter for measuring flux d_{opt}:

1. Maximum allowable diameter.

2. Diameter where the gradient of the growth curve has increased twice in a row.

3. Diameter where there is no decrease in the gradient for two consecutive apertures.

4. Diameter where the growth curve has a downward trend more than expected from noise fluctuations.

The first condition is for normal isolated objects, and the second condition is for growth curves that have unusual fluxes inside the aperture such as from cosmic rays, bad pixels, diffraction spikes, etc. The third and fourth conditions are for isolated faint (small) objects. If the adopted apertures are significantly smaller than the maximum allowable aperture, then a small correction is applied to the total flux to preserve the uniformity of aperture sizes. This is done by extrapolating the growth curve to the maximum allowable aperture size (Fig. 3.17).

After measuring the flux for all objects, PPP remeasures the flux for objects that are classified as brighter galaxies by recomputing the growth curve using a larger maximum aperture.

All flux measurements were converted to instrumental magnitudes using

$$m = m_0 - 2.5 \log(F), \tag{3.4}$$

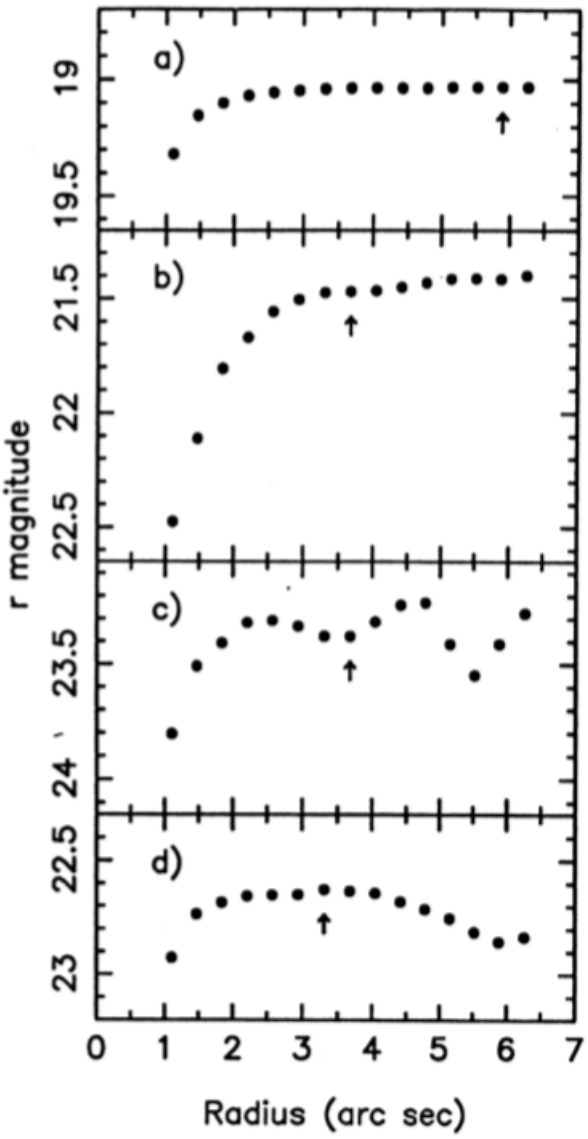

Figure 3.17: Examples of growth curves. (a) Bright star used as one of the reference stars; (b) relatively isolated galaxy; (c) faint galaxy with neighbors; (d) a faint star. The arrow in each panel indicates the adopted aperture (Yee, 1991).

where m is the apparent magnitude, m_0 is the zeropoint and F is the aperture corrected flux. The uncertainty in flux, ΔF, is calculated by

$$\Delta F = \sigma_{sky} N_{pix}^{1/2}, \tag{3.5}$$

where N is the total number of pixels within the aperture, and σ_{sky} is the rms value

per pixel from the local sky.

3.4 Star-Galaxy Classification

After instrumental magnitudes are computed, all objects are classified as either stars (saturated or unsaturated), galaxies, probable galaxies, or defects, by comparing the shape of the growth curve of individual objects to reference stars. More specifically, by computing the classification parameter, C_2, using

$$C_2 = \frac{1}{N_A - 2}\Big(\sum_{i=1}^{N_A}(m_i^* - m_i)\Big) - C_0, \tag{3.6}$$

where N_A is the adopted largest aperture number, m_i and m_i^* are the instrumental magnitudes from the i^{th} aperture of the object and the reference growth curve, respectively, and C_0 is a normalization constant formed by the difference in magnitudes of the object and the reference star within either the first or second aperture.

In general, CCD images have a Point Spread Function (PSF) that varies across the field. Hence, a variable PSF for reference stars would be the ideal choice for the classification process. PPP deals with a variable PSF across the image by using local PSF's as reference for star-galaxy classification. First, PPP picks out a list of non-saturated, isolated stars with d_{opt} equal or close to the maximum allowable aperture. A reference star growth curve is created by averaging growth curves of all candidates. Then the individual growth curves of candidate reference stars are compared with the average. Any object with a growth curve broader than the average curve is rejected and a new average curve is computed. This procedure is repeated until none of the candidates show a significant difference from the average. As a further check, all reference stars were overlaid on the cluster image and each star was visually inspected to confirm they are not saturated, are isolated, and have the expected Gaussian PSF shape. This process also helps to confirm that reference stars are distributed across

the image.

Using the value of C_2, objects are classified into four categories (Yee, 1991):

1. $C_2 \leq -0.15$ are classified as galaxies.

2. $-0.15 < C_2 \leq -0.075$ are considered probable galaxies, and normally assumed to be galaxies.

3. $-0.075 < C_2 \leq 0.1$ are stars.

4. $C_2 > 0.1$ are considered false detections.

The multi-aperture photometry commands create a *'.phm'* file, which contains information for each object such as instrumental magnitude, C_2 value, classification, sky value, number of neighbors, etc. It also produces a plot of C_2 vs instrumental magnitude for all objects in an image (Fig. 3.19). Deviations from the expected shape of the plot (based on simulations) help detect incorrect values for input PPP parameters (Fig. 3.18) or errors in basic calibration (Fig. 3.19).

Faint objects in the halo of bright stars, galaxies or diffraction spikes, or two objects that are close together, are subjected to misclassifications. These type of objects can be mostly found just below the stellar sequence (narrow, horizontal sequence at $C_2 = 0.0$; Figure 3.20) of the C_2 vs instrumental magnitude plot. This region was manually checked and objects were reclassified when appropriate.

For each cluster, photometry steps were performed on both cluster images (with and without the BCG) and the BCG measurements were transferred to the *.phm* file of the BCG subtracted image using its PPP number.

At brighter magnitudes, C_2 separates stars and galaxies very accurately (Fig. 3.20), but at fainter magnitudes C_2 values of stars and galaxies start to merge. This merging is due to faint galaxies being smaller and less well-resolved, as well as a lower signal-to-noise (S/N) ratio, which prevents the growth curve from being computed for large diameters. Since a large increase in the star count is not expected at

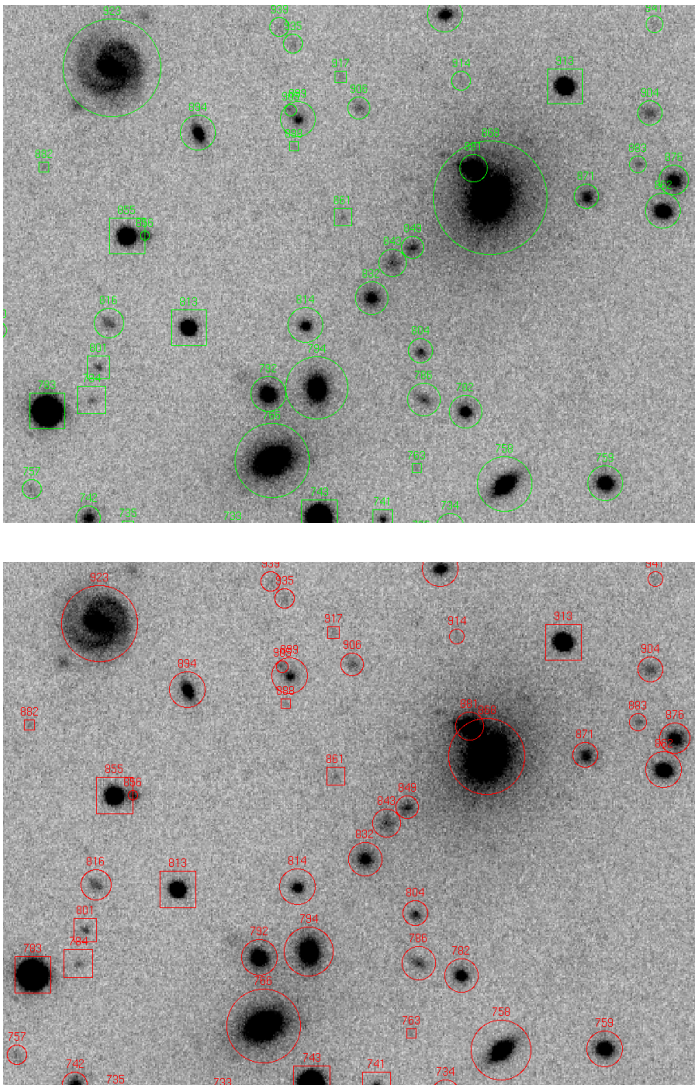

Figure 3.18: Two panels show two different adopted apertures for each object, which are generated using different values for PPP parameters. For the top panel, the adopted aperture for some objects doesn't contain all of the flux, but for the bottom panel, all the flux is within the adopted aperture. Circle apertures represent galaxies and square apertures represent stars or noise detections.

fainter magnitudes, a variable classifier can be applied to select a statistical sample of galaxies.

The variable classifier computes the modal values of C_2 in magnitude bins, excluding saturated and bright stars. A curve which defines the ridge line of the distribution

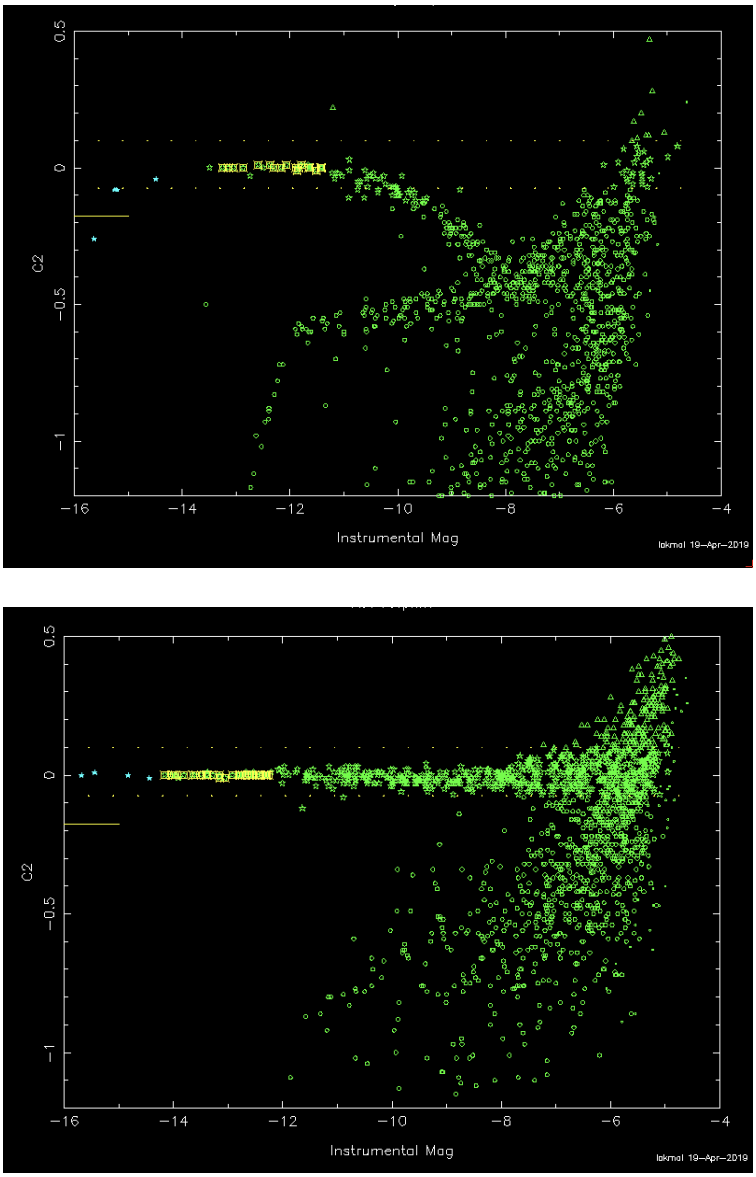

Figure 3.19: C_2 vs instrumental magnitude plot for the Abell 671 cluster image; top panel with a pre-processing error (before stacking, three of the raw images were not bias and flat field corrected); bottom panel without any error.

of points on the C_2 magnitude plane (solid green curve on Fig 3.20) is generated by heavily smoothing the modal values as a function of magnitude. Then a second curve is defined based on rms values (σ) of C_2 within each magnitude bin. Simulations suggest that the second curve is usually between 1.0 and 1.5σ above the ridge line. For this research, a second curve is defined 1.2σ above the ridge line. Objects with

$C_2 > -0.075$ but below the 1.2σ curve are classified as galaxies.

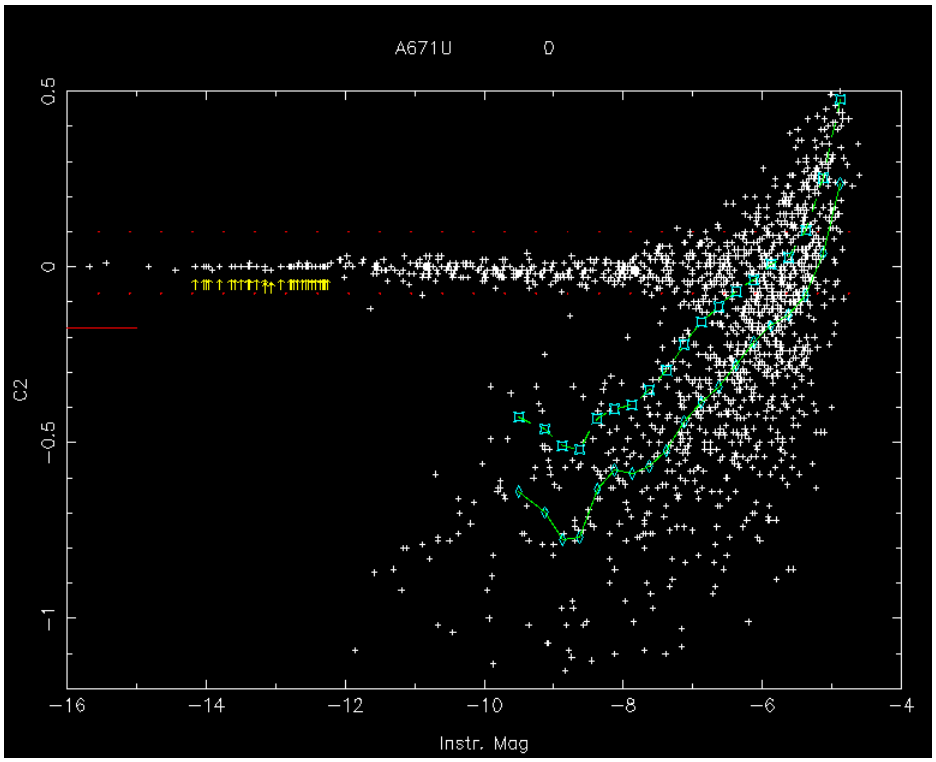

Figure 3.20: C_2 vs instrumental magnitude plot for Abell 671 cluster image with variable classifier. Objects around $C_2 = 0$ are considered to be stars. Yellow arrows represent reference stars. The lower green ridgeline curve is generated by heavily smoothing the modal values as a function of magnitude, and the upper dashed green curve is defined based on the rms values (σ) of C_2 (1.2σ for this study). Objects above the 1.2σ curve are, statistically, classified as stars and objects below the curve are classified as galaxies.

3.4.1 Photometric Zero Point

The photometric zero point (ZP) is defined as the magnitude of an object that produces one count per second. A count is the analog-to-digital unit (ADU) number assigned to each pixel in an image. The ZP calibrates the relationship between the instrumental magnitude and a standard photometric magnitude system. Following recommendations on the SDSS website, SDSS `cModelMag` u-band magnitudes were

used as the standard magnitude system for this study. The `cModelMag` of an object is derived from a composite flux of an exponential and de Vaucouleurs profiles that best fits the object.[3]

SDSS magnitudes are 'almost' calibrated to the AB magnitude system, by which a magnitude 0 object should have the same counts as a source of $f_\nu = 3631\ Jy$, where f_ν is the spectral flux density.[4] Hence calibrated u-band magnitudes of WIYN 0.9m sample are assumed to be AB magnitudes. The AB magnitude system is defined by (Fukugita et al., 1996)

$$m = -2.5\ log_{10}\ f_\nu(ergs\ s^{-1}\ cm^{-2}\ Hz^{-1}) - 48.60. \tag{3.7}$$

3.4.2 Zero Point Calibration

The instrumental magnitude of each galaxy was matched to the corresponding SDSS u-band magnitude, using its celestial coordinates, to obtain the magnitude difference. The instrumental magnitude ZP was adjusted using the median of the magnitude difference for all matching galaxies. Once an appropriate ZP adjustment had been made to instrumental magnitudes, each final cluster catalog was compared with the SDSS catalog to confirm that the magnitude offset was zero (Fig. 3.21). The magnitudes from SDSS were corrected for galactic dust using Schlegel et al. (1998), therefore the calibrated ZP includes an extinction correction (see section 3.9). The uncertainty in the ZP was determined by taking the median absolute deviation of the magnitude differences. The resulting magnitude zero points are tabulated in Table 3.1.

3.4.3 Completeness Limit

The magnitude depth of each cluster was checked to determine the faintest magnitude observed within the completeness limit. This was determined by binning all galaxies

[3] `https://www.sdss.org/dr12/algorithms/magnitudes/`
[4] `https://www.sdss.org/dr14/algorithms/fluxcal/`

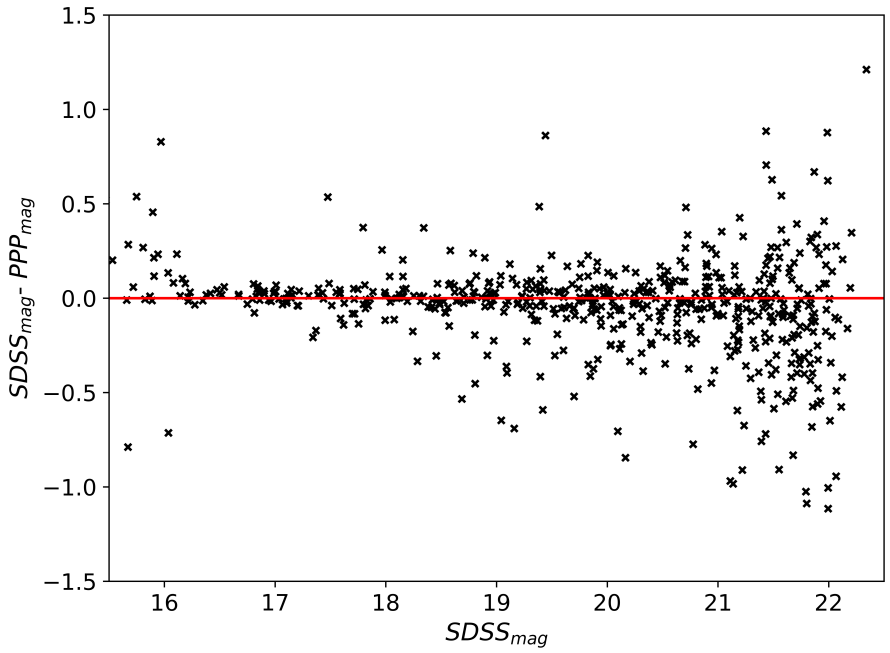

Figure 3.21: Difference between extinction-corrected u-band SDSS magnitudes and PPP magnitudes for objects in the Abell 2589 cluster, after applying appropriate ZP correction. The red horizontal line is plotted at zero magnitude difference as a reference.

in 0.1 magnitude bins and calculating the number of galaxies in each bin. The number of galaxies per bin is expected to increase as a power-law with decreasing brightness. However, beyond a certain faint magnitude limit, galaxy counts will start decreasing as the observations become more incomplete. This magnitude limit depends on the telescope, detector, integration time, seeing, etc. To ensure 100% completeness, the catalog is considered complete 0.8 magnitude brighter than the turnover magnitude (Fig. 3.22). The choice of 0.8 magnitude was made to try to probe as deep into the dwarf population as possible while maintaining 100% completeness for magnitudes brighter than the adopted limit (Barkhouse et al., 2007).

Table 3.1: Zero points and the 100% completeness limit (m_{uCL}) for u-band data from the WIYN 0.9m cluster sample.

Cluster	Zero Point(u-band)	m_{uCL}
A1142	21.00 ± 0.14	22.80
A1213	21.10 ± 0.15	22.40
A2152	21.42 ± 0.09	22.40
A2399	21.07 ± 0.09	22.00
A2572	20.85 ± 0.07	22.50
A2589	21.25 ± 0.09	22.00
A2593	21.10 ± 0.09	23.10
A260	20.98 ± 0.12	22.20
A2634	21.36 ± 0.09	22.20
A2666	20.82 ± 0.07	22.50
A582	21.00 ± 0.08	22.20
A634	20.58 ± 0.08	22.00
A671	20.92 ± 0.07	21.80
A779	21.33 ± 0.16	22.40

3.5 Cluster Dynamical Radius

Most studies define a "cluster" based on the total area covered by the telescope detector or by using a specific physical length (Barkhouse et al., 2007). Since galaxy clusters vary in size and richness, to fairly compare cluster properties, each cluster needs to be scaled according to its mass (Rude et al., 2020). A dynamical radius calculated for each cluster, r_{200}, was used as a normalization factor to compare cluster characteristics. This normalized dynamical radius will allow us to compare properties

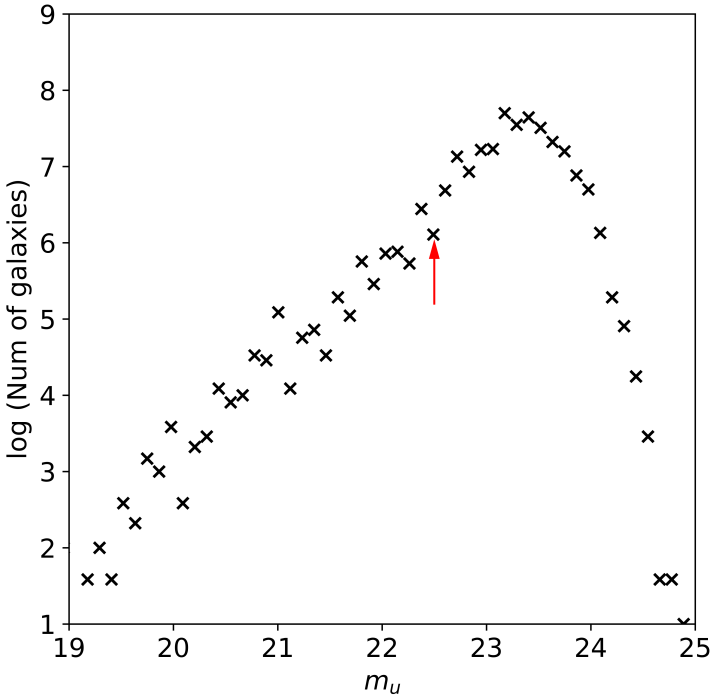

Figure 3.22: u-band completeness limit for Abell 779 is defined as 0.8 magnitude brighter than the turnover point. The red arrow indicates the adopted 100% magnitude completeness limit.

of galaxy clusters as a function of cluster-centric radius in a more robust way.

The r_{200} radius is defined as the radius of a sphere within which the average density is 200 times the critical density of the Universe and is expected to contain most of the virialized mass of a cluster (Barkhouse et al., 2007). The critical density, ρ_c, is given by

$$\rho_c = \frac{3H^2}{8\pi G}, \tag{3.8}$$

where H and G are the Hubble and gravitational constants, respectively. The r_{200} values are calculated using the average cluster velocity dispersion, σ_v, (Demarco et al., 2010)

$$r_{200} = \frac{\sqrt{3}\sigma_v}{10H(z)}, \tag{3.9}$$

where the Hubble parameter $H(z)$ is given by:

$$H(z) = H_0\sqrt{\Omega_m(1+z)^3+\Omega_\Lambda}. \tag{3.10}$$

Velocity dispersion measurements for all clusters (Table 3.2) are available in the literature (Lauer et al., 2014; Cava et al., 2009; Castagné et al., 2012; Popesso et al., 2007; Tovmassian & Andernach, 2012; Rude et al., 2020; White et al., 1997).

3.6 Cluster Red-Sequence

As mentioned in Chapter I, the red-sequence of a color-magnitude diagram (CMD) is defined by the passively evolving cluster galaxy population, and it tends to become bluer towards fainter magnitudes. This property can be quantified by measuring the slope of a linear fit to the red-sequence. The cluster red-sequence was used in this study to statistically remove projection effects (i.e. non-cluster galaxies that are projected onto the 2-D cluster image) and select the cluster galaxy population. This method requires two filters that bracket the 4000 Å break. The 4000 Å break is a spectral feature that represents a strong change in flux for early-type galaxies due to the blanket absorption of high energy radiation from metals in the stellar atmosphere of stellar populations that lack blue hot stars.

3.6.1 Red-Sequence Fitting

u-band data of galaxies selected from the WIYN 0.9m sample were matched with extinction corrected r-band data from SDSS to construct the color-magnitude diagram of each cluster (Fig. 3.23). Each red-sequence was measured via a linear fit to color-magnitude data. This fit was carried out on galaxies within a radius of 0.5 r/r_{200} of the cluster center. This cutoff radius will minimize background galaxy contamination.

A histogram of the number of galaxies versus color was constructed for each cluster

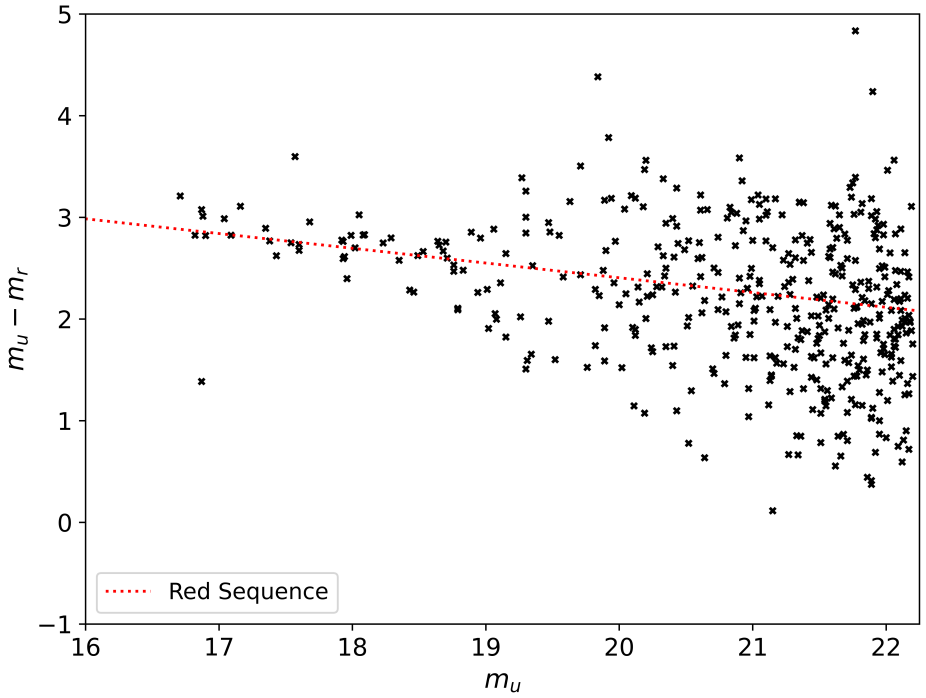

Figure 3.23: Color-magnitude diagram for Abell 2634 with the red-sequence delineated by the dotted line

by rectifying the red-sequence for galaxies brighter than $M_u = -14$. The rectification process is done by translating and rotating the red-sequence so that the red-sequence is centered on a color of zero (Fig. 3.24). An additional background histogram was constructed using the same procedure on a background field composed using nine background fields from Rude et al. (2020). The background histograms were scaled by the ratio of the cluster area to the total background area, and then subtracted from the cluster histograms. Finally, a Gaussian function was fit to each net cluster count histogram using the Marquardt-Levenberg method[5] to determine the dispersion of the CMR (Table 3.2). The histograms with the Gaussian overlaid are shown in Figs. 3.25 – 3.28.

From the dispersion of the CMR (σ), an appropriate color cut was chosen to

[5] `http://gnuplot.sourceforge.net/docs_4.2/node82.html`

separate galaxies into red and blue galaxy samples. These color cuts will ensure that the inclusion of background galaxies is kept to a minimum. Galaxies found within $\pm 3\sigma$ of the red-sequence are considered red color galaxies and are dominated, morphologically, by early-type galaxies. Since cluster blue galaxies occupy the region blueward of the red-sequence, galaxies within -3σ and -8σ of the red-sequence are considered as blue galaxies, and are comprised mainly of late-type galaxies.

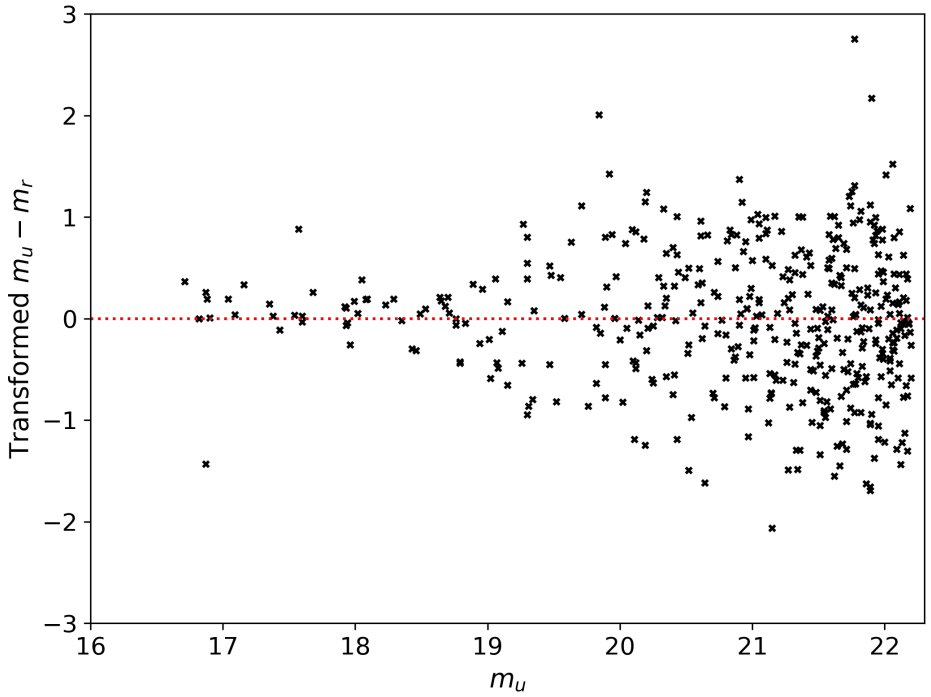

Figure 3.24: Rectified color-magnitude diagram for Abell 2634. The color and magnitude of each object have been translated and rotated so that the red-sequence slope is zero. The red horizontal line is plotted at $m_u - m_r = 0$ as a reference.

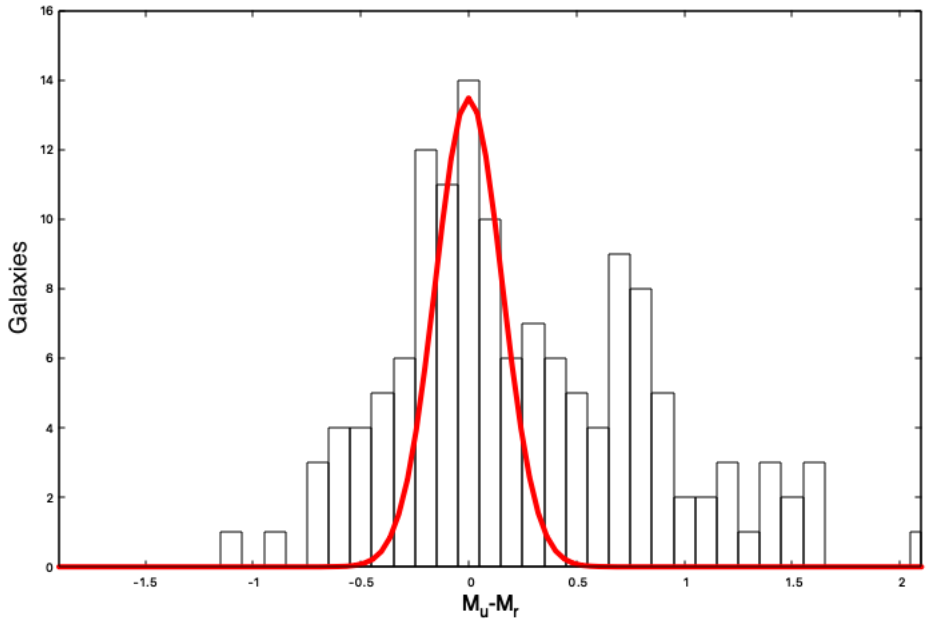

Figure 3.25: Background corrected color histogram for galaxies in Abell 1142.

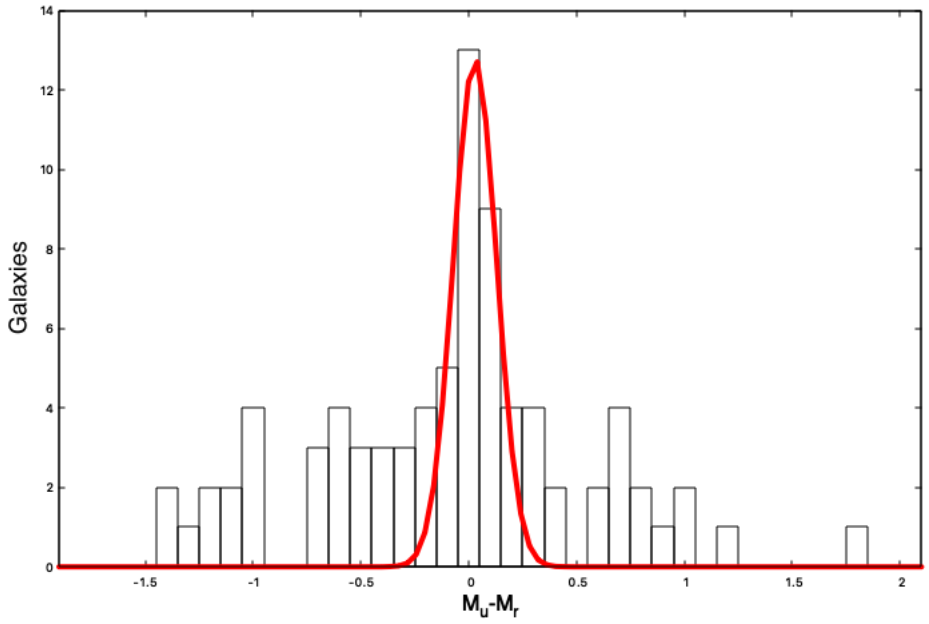

Figure 3.26: Background corrected color histogram for galaxies in Abell 2666.

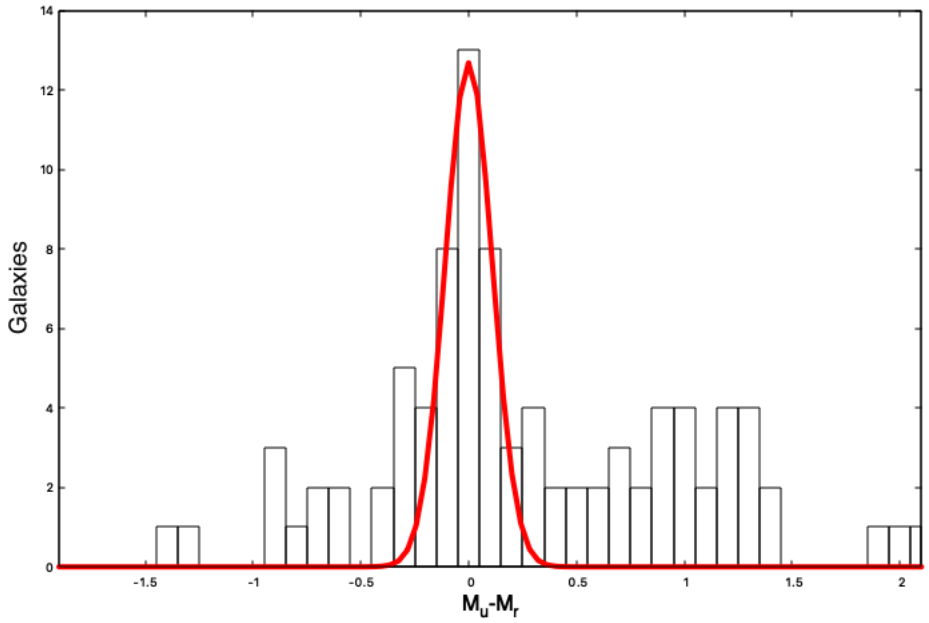

Figure 3.27: Background corrected color histogram for galaxies in Abell 582.

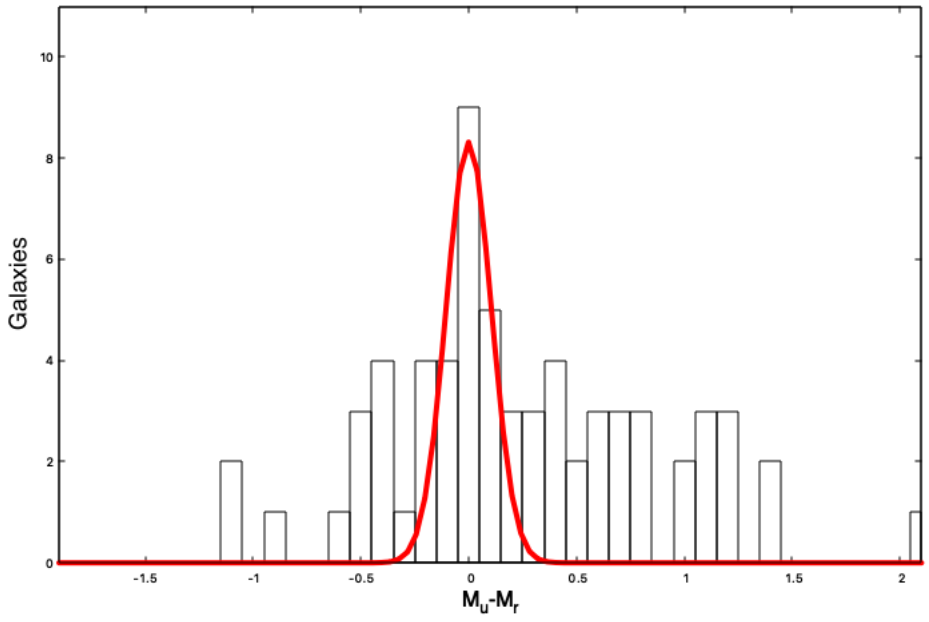

Figure 3.28: Background corrected color histogram for galaxies in Abell 634.

Barkhouse et al., Valentinuzzi et al., Rude et al. used B-R vs R, B-V vs V, and u-r vs r color-magnitude diagrams, respectively, to fit and measure the dispersion of the CMR. These measurements are available in the literature and were used to select

cluster galaxies.

CMR dispersion measurements for ten clusters of the WIYN 0.9m sample were available in Barkhouse et al. and Valentinuzzi et al. studies. Due to the low scattering of the CMR in B-R and B-V colors compared to u-r, dispersion measurements from the above-mentioned studies were used for these ten clusters. A catalog matching algorithm with a three-arcsecond search radius was used to find matching galaxies in each u-band catalog.

3.7 SDSS Spectroscopic Data

Spectral data for all clusters were available from the SDSS, along with redshifts of galaxies. An upper (z_{max}) and a lower limit (z_{min}) for redshift were derived using the recessional velocity and the velocity dispersion of each cluster (equations 3.12 and 3.13). Galaxies (both blue and red color) within this range were classified as cluster galaxies.

The recession velocity of each cluster was calculated using

$$z = \sqrt{\frac{1 + v/c}{1 - v/c}} - 1, \tag{3.11}$$

where z is the redshift of the cluster, and v is the recessional velocity. Following guidelines of Bayliss et al. (2017), the maximum ($v_{max} = v + 3\sigma_v$) and the minimum ($v_{min} = v - 3\sigma_v$) recession velocities were used to calculate the upper and the lower limit of the redshift for each cluster based on

$$z_{max} = \sqrt{\frac{1 + v_{max}/c}{1 - v_{max}/c}} - 1, \tag{3.12}$$

$$z_{min} = \sqrt{\frac{1 + v_{min}/c}{1 - v_{min}/c}} - 1. \tag{3.13}$$

Table 3.2: Measured properties of the cluster sample

Cluster	σ_v (km/s)	Refs [a]	r_{200} (Mpc)	σ	z_{max}	z_{min}
A1142[b]	757 ± 44	L14	1.843	0.155	0.0428	0.0271
A119[d]	901 ± 40	L14	2.184	0.188	0.0538	0.0349
A1213[c]	572 ± 43	L14	1.385	0.073	0.0428	0.0271
A1291[d]	724 ± 53	L14	1.749	0.098	0.0592	0.0439
A1413[c]	1196 ± 89	DC12	2.761	0.076	0.1576	0.1298
A147[d]	621 ± 79	L14	1.506	0.086	0.0505	0.0375
A154[c]	988 ± 146	L14	2.373	0.115	0.0742	0.0531
A1569[c]	622[e]	L14	1.487	0.067	0.0807	0.0673
A160[d]	784 ± 111	C09	1.901	0.102	0.0496	0.0379
A1650[c]	799 ± 87	P07	1.901	0.084	0.0926	0.0752
A1656[c]	1035 ± 25	L14	2.534	0.056	0.0338	0.0126
A1668[d]	654[e]	S99	1.571	0.081	0.0710	0.0572
A168[d]	625 ± 36	L14	1.515	0.137	0.0513	0.0382
A1775[c]	568 ± 60	L14	1.359	0.071	0.0782	0.0659
A1795[d]	861 ± 56	L14	2.069	0.065	0.0717	0.0533
A1831[d]	1176 ± 111	L14	2.826	0.102	0.0756	0.0505
A1913[c]	636 ± 130	L14	1.536	0.047	0.0595	0.0461
A1920[b]	562 ± 84	T12	1.306	0.078	0.1375	0.1246
A193[d]	776 ± 62	L14	1.878	0.601	0.0568	0.0405
A1940[b]	785[e]	S99	1.816	0.07	0.1492	0.1309
A1983[d]	541 ± 27	L14	1.311	0.08	0.0508	0.0395
A1991[d]	604 ± 57	L14	1.455	0.077	0.0646	0.0517
A2022[c]	607 ± 74	L14	1.462	0.07	0.0643	0.0514
A2029[c]	1222 ± 75	L14	2.914	0.08	0.0921	0.0655

Table 3.2: (continued)

Cluster	σ_v (km/s)	Refs[a]	r_{200} (Mpc)	σ	z_{max}	z_{min}
A2100[b]	582[e]	R20	1.337	0.072	0.1599	0.1462
A2107[b]	629 ± 46	L14	1.527	0.051	0.0476	0.0345
A2124[d]	596 ± 58	C09	1.430	0.092	0.0753	0.0582
A2147[b]	821[e]	S99	1.999	0.0777	0.0436	0.0265
A2149[d]	330 ± 46	P07	0.792	0.089	0.0691	0.0615
A2152[c]	456 ± 62	L14	1.107	0.08	0.0458	0.0363
A2169[d]	524 ± 60	C09	1.262	0.071	0.0639	0.0531
A2199[b]	780 ± 52	R20	1.904	0.105	0.0381	0.0220
A21[c]	621[e]	S99	1.469	0.126	0.1015	0.0878
A2244[c]	1240[e]	S99	2.931	0.073	0.1106	0.0832
A2255[c]	1266[e]	S99	3.017	0.073	0.0942	0.0666
A2356[c]	716 ± 85	P07	1.675	0.061	0.1261	0.1099
A2399[d]	713 ± 27	L14	1.717	0.129	0.0655	0.0504
A2440[c]	957[e]	S99	2.269	0.088	0.1015	0.0804
A2457[d]	642 ± 53	L14	1.545	0.075	0.0663	0.0526
A2572[d]	593 ± 36	L14	1.440	0.078	0.0465	0.0341
A2589[d]	872 ± 60	L14	2.117	0.073	0.0505	0.0323
A2593[d]	644 ± 23	L14	1.563	0.076	0.0480	0.0346
A260[c]	754 ± 74	L14	1.835	0.093	0.0442	0.0285
A2622[d]	860 ± 121	L14	2.067	0.124	0.0712	0.0529
A2626[d]	648 ± 53	L14	1.564	0.093	0.0610	0.0473
A2634[c]	919 ± 45	L14	2.242	0.047	0.0409	0.0219
A2657[d]	807 ± 52	L14	1.960	0.071	0.0489	0.0321
A2665[d]	771[e]	AVG	1.859	0.08	0.0638	0.0475

Table 3.2: (continued)

Cluster	σ_v (km/s)	Refs[a]	r_{200} (Mpc)	σ	z_{max}	z_{min}
A2666[b]	377 ± 47	L14	0.921	0.999	0.0307	0.0230
A2670[c]	963 ± 34	L14	2.299	0.094	0.0867	0.0658
A351[b]	510 ± 118	P07	1.197	0.08	0.1168	0.1053
A362[b]	758[e]	R20	1.714	0.102	0.1933	0.1748
A582[b]	324 ± 56	L14	0.780	0.109	0.0616	0.0548
A602[d]	796 ± 61	L14	1.915	0.09	0.0690	0.0520
A634[b]	331 ± 25	L14	0.809	0.105	0.0299	0.0231
A646[c]	738 ± 96	P07	1.718	0.13	0.1355	0.1186
A655[b]	736 ± 78	P07	1.714	0.084	0.1355	0.1186
A671[d]	850 ± 33	L14	2.055	0.077	0.0592	0.0413
A690[c]	546 ± 46	L14	1.302	0.091	0.0847	0.0729
A76[b]	492 ± 74	R20	1.195	0.074	0.0461	0.0359
A779[c]	450 ± 23	L14	1.102	0.109	0.0271	0.0179
A795[b]	778 ± 61	R20	1.803	0.083	0.1450	0.1271
A84[c]	769[e]	W97	1.812	0.097	0.1116	0.0945
A85[d]	1009 ± 31	L14	2.434	0.073	0.0658	0.0444
A957[d]	772 ± 52	L14	1.871	0.062	0.0531	0.0369
A98N[b]	690[e]	R20	1.625	0.093	0.1117	0.0963
A98S[b]	812[e]	R20	1.912	0.089	0.1131	0.0950
A999[c]	286[e] ± 25	L14	0.697	0.085	0.0353	0.0293
IIZW108[d]	549 ± 42	C09	1.332	0.074	0.0548	0.0440
MKW3s[d]	539 ± 58	C09	1.306	0.123	0.0504	0.0391
RX0058[d]	696 ± 119	C09	1.682	0.098	0.0537	0.0403
RX1022[d]	582 ± 91	C09	1.396	0.164	0.0552	0.0430

Table 3.2: (continued)

Cluster	σ_v (km/s)	Refs[a]	r_{200} (Mpc)	σ	z_{max}	z_{min}
Z2844[d]	529 ± 84	C09	1.281	0.073	0.0557	0.0444
Z8852[d]	696 ± 67	C09	1.689	0.091	0.0480	0.0321

[a] Reference for the velocity dispersion: W97 – White et al. (1997); S99 – Struble & Rood (1999); P07 – Popesso et al. (2007); C09 – Cava et al. (2009); DC12 – (Castagné et al., 2012); T12 – Tovmassian & Andernach (2012); L14 – Lauer et al. (2014); R20 – Rude et al. (2020); AVG –average velocity distribution of the Valentinuzzi et al. (2011) sample.

[b] u-r color was used for CMD

[c] B-R color was used for CMD

[d] V-R color was used for CMD

[e] No published uncertainty values

3.8 Cluster Distances

The luminosity distance – the distance based on the change in the brightness of a uniformly emitting source (i.e. a star) – to each cluster was calculated using its redshift

$$D_L(z) = (1+z)^2 \, D_A(z), \tag{3.14}$$

where $D_L(z)$ and $D_A(z)$ are the luminosity distance and the angular-diameter distance, respectively. The distance to an object based on its change in angular size is defined as the angular diameter distance and is expressed as

$$D_A(z) = \frac{cz}{H_0(1+z)}, \tag{3.15}$$

where H_0 is the Hubble constant, and c is the speed of light in a vacuum (Wright, 2006). The absolute magnitude of a galaxy in a cluster was calculated using

$$M = m - (5 \log D_L(z) - 5) - \mu - K, \tag{3.16}$$

where M is the absolute magnitude (defined as the apparent magnitude that an object would have at a distance of 10 pc = 3.26 light-years), m is the apparent magnitude, μ is the extinction, and K is the K-correction (defined in section 3.10). Since galaxies in a particular cluster are all at approximately the same distance from the observer, individual galaxy distance measurements (using redshift) are not necessary.

3.9 Extinction Correction

Heavy elements present in stellar dust are believed to be produced in dense, relatively cool environments such as the atmosphere of red giant stars, and injected into the ISM through stellar winds and explosions. These heavy elements are reprocessed in the ISM to form dust grains (Schlafly & Finkbeiner, 2011). Dust grains will absorb and scatter light from a distant source and make the source appear dimmer and redder to the observer. These effects are known as extinction and interstellar reddening, respectively. Due to the general size of dust grains, shorter wavelengths, such as UV and blue, get absorbed and scattered more efficiently than red light (Schneider, 2007).

Since both interstellar reddening and extinction are the result of light interacting with dust grains, one can calculate the amount of extinction by measuring the reddening of an object

$$A(X) = R(X) \times E(B - V), \tag{3.17}$$

where $A(X)$ is the extinction of a passband X, E(B-V) is the color excess or the reddening of the object, and $R(X)$ is a proportionality constant, defined as extinction in X-band relative to E(B-V) (Yuan et al., 2013).

The full-sky dust maps produced by Schlegel et al. (1998) were used in this study to correct UV and u-band magnitudes for galactic extinction; the extinction due to

light passing through the Milky Way. For u-band data, the extinction correction for each cluster was obtained from NED. These values are derived based on $R(V) = 3.1$ using the reddening values from Schlegel et al. (1998). UV magnitudes were corrected for galactic extinction using R(FUV) = 8.24 and R(NUV) = 8.2 as used in Wyder et al. (2007) and E(B-V) values from Schlegel et al. (1998).

The main source of uncertainty in estimating the SFR of a galaxy, especially at short wavelengths, is the internal extinction of the host galaxy. Internal extinction is highly uncertain due to how it changes between different galaxy types and luminosity.

WISE W4 data was used to correct the GALEX FUV and NUV luminosities (in units of $erg\ s^{-1}$) for dust extinction following the procedure outlined in Cortese (2012)

$$L(FUV)_{corrected} = L(FUV) + 3.89 \times L(W4), \tag{3.18}$$

$$L(NUV)_{corrected} = L(NUV) + 2.26 \times L(W4). \tag{3.19}$$

No correction for galactic extinction was applied to WISE data since it is typically < 0.01 magnitude. No correction for internal extinction was applied to the u-band and WISE data. Since the primary goal of this study is to compare the relative differences in the SFR rather than calculate absolute values, these assumptions will have a minimum effect on the final results of this study.

3.10 K-correction

Due to the expansion of the Universe, the measured light of a galaxy at a given wavelength is redshifted with respect to the rest-frame wavelength. In order to compare galaxies at various redshifts, this effect must be corrected by applying a wavelength-dependent k-correction to each galaxy's magnitude. Chilingarian et al. (2010) used a two-dimensional polynomial as a function of redshift and color to estimate k-corrections. This procedure was used in this study to calculate k-corrections

Table 3.3: The polynomial coefficients used in the u-band K-correction calculation using u-r color. Values were obtained from `http://kcor.sai.msu.ru/`

$a_{x,y}$	y=0	1	2	3
x=0	0	0	0	0
1	10.3686	-6.12658	2.58748	-0.299322
2	-138.069	45.0511	-10.8074	0.95854
3	540.494	-43.7644	3.84259	0
4	-1005.28	10.9763	0	0
5	710.482	0	0	0

for each galaxy in the UV and u passbands. The form of the correction is given by

$$K_q(z, m_{f_1} - m_{f_2}) = \sum_{x=0}^{N_z} \sum_{y=0}^{N_c} a_{x,y}\ z^x\ (m_{f1} - m_{f2})^y, \tag{3.20}$$

where K_q is the K-correction for filter q, z is the spectroscopic redshift, $a_{x,y}$ are polynomial coefficients, and m_{f_1} and m_{f_2} are apparent magnitudes in filters f_1 and f_2, respectively. N_z and N_c are empirically selected polynomial powers in the redshift and color dimensions, respectively.

K-corrections for u-band data were calculated using the u-r color of each cluster galaxy, the redshift of the cluster, and polynomial coefficients given in Table 3.3. The same procedure was used to calculate k-corrections for GALEX FUV and NUV data using FUV-u and NUV-r colors along with polynomial coefficients in Tables 3.4 and 3.5. No K-correction was applied to WISE data since it is negligible.

3.11 Flux and Luminosity Calculations

The extinction and k-corrected apparent magnitudes of each passband were converted into flux densities using the definition of the AB magnitude (equation 3.7) of an object

Table 3.4: The polynomial coefficients used in the FUV passband K-correction calculation using FUV-u color. Values were obtained from `http://kcor.sai.msu.ru/`

$a_{x,y}$	y=0	1	2	3
x=0	0	0	0	0
1	-1.67589	0.447786	0.369919	-0.0954247
2	2.10419	6.49129	-2.54751	0.177888
3	15.6521	-32.2339	4.4459	0
4	-48.3912	37.1325	0	0
5	37.0269	0	0	0

Table 3.5: The polynomial coefficients used in the NUV passband K-correction calculation using NUV-r color. Values were obtained from `http://kcor.sai.msu.ru/`

$a_{x,y}$	y=0	1	2	3
x=0	0	0	0	0
1	2.2112	-1.2776	0.219084	0.0181984
2	-25.0673	5.02341	-0.759049	-0.0652431
3	115.613	-5.18613	1.78492	0
4	-278.442	-5.48893	0	0
5	261.478	0	0	0

$$f_\nu = 3631 \times 10^{-23} \times 10^{-0.4m} \quad \frac{\text{ergs}}{\text{sec cm}^2 \text{ Hz}}, \tag{3.21}$$

where f_ν is the flux density in frequency units and m is the apparent AB magnitude (Brown et al., 2017). f_ν was converted to the line flux (F_λ) in wavelength units by using

$$F_\lambda = f_\nu \frac{c}{\lambda} \quad \frac{\text{ergs}}{\text{sec cm}^2}, \tag{3.22}$$

where c is the speed of light and λ is the central wavelength of the filter.

All u-band and GALEX magnitudes are AB magnitudes. Since WISE magnitudes are given in the Vega magnitude system (magnitude system derived from the spectrum of the bright star Vega), they were recalibrated to the AB magnitude system using the method used in Jarrett et al. (2011).

For each passband, the line flux was converted to luminosity using

$$L_\lambda = F_\lambda \times 4\pi D_L^2 \quad \frac{\text{ergs}}{\text{sec}}. \tag{3.23}$$

Chapter IV

RESULTS

4.1 Introduction

In order to investigate how the cluster environment affects galaxy evolution, the star formation rate of cluster galaxies was measured and presented as a function of normalized cluster-centric radius (r/r_{200}) for multiple passband data. To better understand these effects, cluster galaxies were divided into two color bins, red and blue (see section 3.6.1). Additionally, to understand the effect of the high-density cluster environment on star formation in galaxies of different masses, the SFR of low-mass dwarf galaxies and high-mass giant galaxies was explored.

For all passbands, cluster galaxies from the 74-cluster sample were stacked in order to measure the radial dependence of star formation. All radial distances were calculated using the cluster center defined as the centroid of the BCG and normalized with respect to r_{200}. The median value of star formation was calculated and plotted for five equal-sized cluster-centric radial bins between $0.0 \leq r/r_{200} \leq 1$. The median absolute deviation (MAD) values were used to estimate the size of error bars in each radial bin.

4.1.1 Giant and Dwarf Galaxies

An important aspect of this study is to explore any differences in star formation between giant and dwarf galaxies as a function of cluster-centric radius. To this end, cluster galaxies were separated into giants and dwarfs based on the absolute r-

band magnitude, M_r. Following the classification used in Rude et al. (2020), galaxies brighter than $M_r = -19.5$ were classified as giants and those having a brightness $M_r \geq -19.5$ (i.e. lower luminosity) are categorized as dwarfs (Fig. 4.1).

Recall that redshift measurements derived using SDSS spectroscopic data were used in this study to select cluster galaxies. SDSS spectroscopic surveys target non-stellar objects with well-measured photometry brighter than $\mathrm{r}_{petro} = 17.7$, where r_{petro} is the r-band Petrosian magnitude of the object.[1] This limit is equal to a median absolute magnitude of $M_r = -19.29$, calculated using the median redshift of the cluster sample used in this study ($\mathrm{z}_{median} = 0.0567$). Since the spectroscopic data samples a low number of dwarf galaxies, the dwarf-giant selection criteria is biased against dwarf galaxies. This is evident by the low number of dwarf galaxies with SDSS spectra present in the galaxy sample used in this study (see Fig. 4.1).

[1] `https://www.sdss.org/dr16/algorithms/magnitudes/`

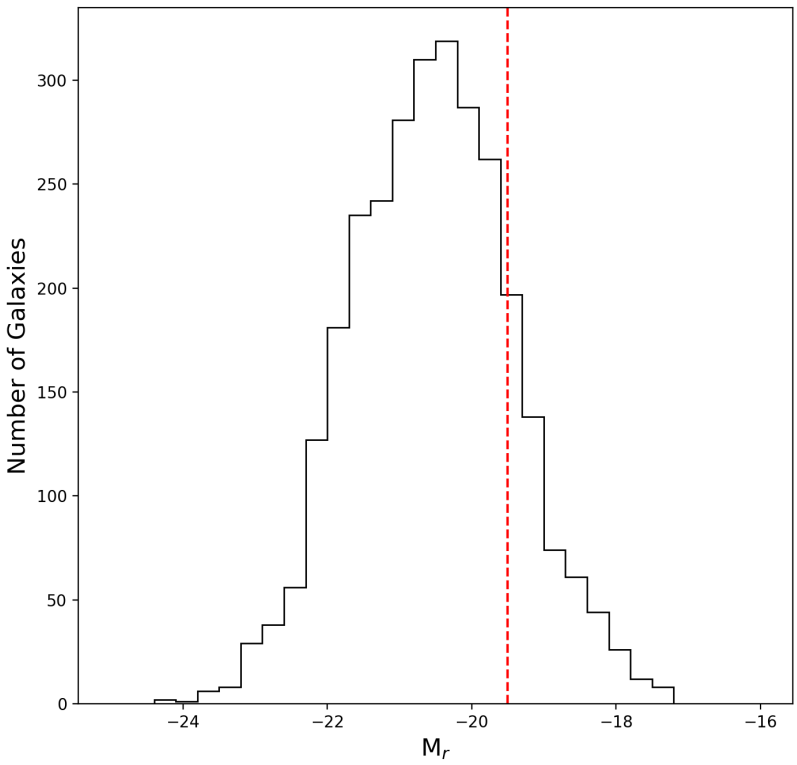

Figure 4.1: Division of galaxies into giants and dwarfs. The red dashed vertical line represents the $M_r = -19.5$ divide between giant and dwarf galaxies.

4.2 u-band Star Formation Rate

The u-band SFR, $\psi(u)$, for both blue and red cluster galaxies was calculated using the calibration derived by (Moustakas et al., 2006)

$$\psi(u)\ (M_\odot\ \mathrm{yr}^{-1}) = (1.4 \pm 1.1) \times 10^{-43}\ L(u)\ \ \mathrm{ergs\ s}^{-1}, \tag{4.1}$$

where $L(u)$ is the extinction and k-corrected u-band luminosity of a cluster galaxy. Following the same guidelines used for the well-known Kennicutt (1998) relations of SFRs, this calibration assumes a solar metallicity and a Salpeter IMF (see section 1.5) with lower and upper mass cutoffs of 0.1 and 100 $M_\odot$. The median SFR value

for each radial bin was plotted as a function of cluster-centric radius for both red and blue galaxies (Fig. 4.2).

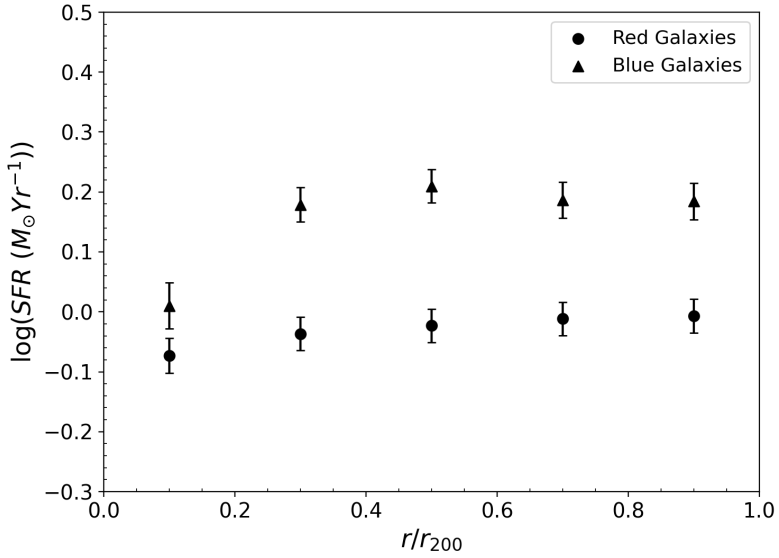

Figure 4.2: Logarithmic value of u-band SFR for red and blue cluster galaxies as a function of normalized cluster-centric radius. Each marker represents the median value for each $r/r_{200} = 0.2$ radial bin. Vertical error bars represent 20% of the MAD of each data point.

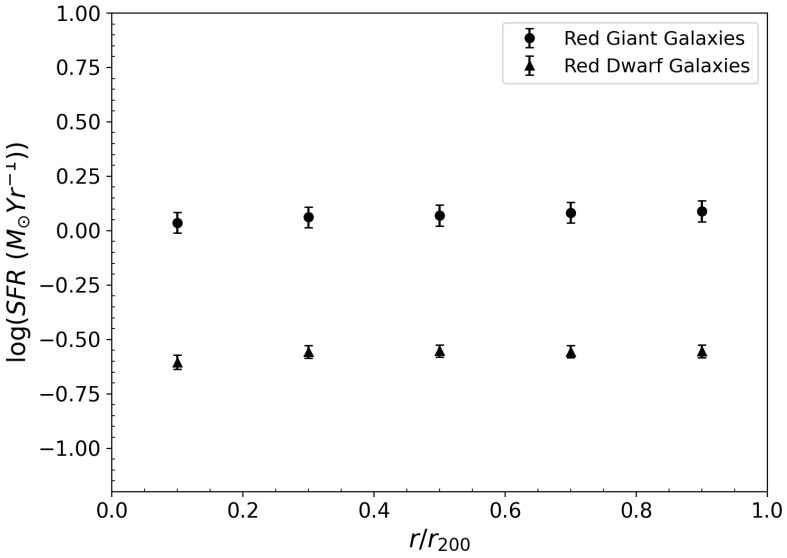

Figure 4.3: Logarithmic value of u-band SFR for red giant and dwarf galaxies as a function of normalized cluster-centric radius. Vertical error bars represent 20% of the MAD of each data point.

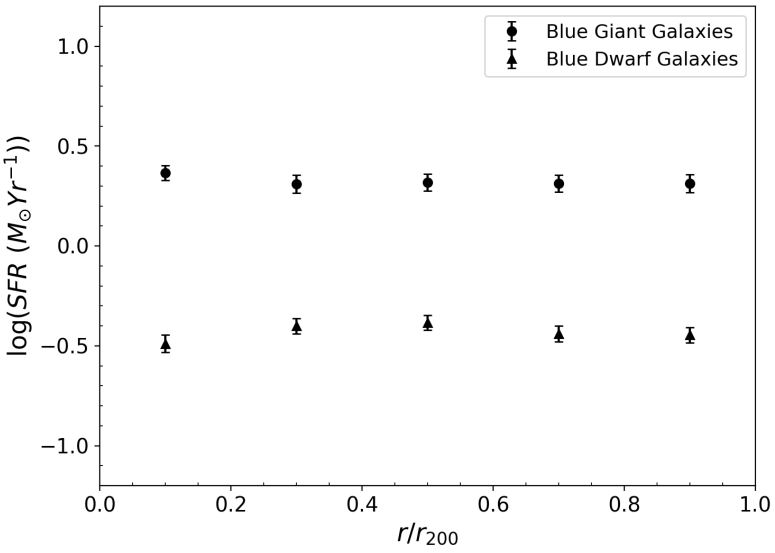

Figure 4.4: Logarithmic value of u-band SFR for blue giant and dwarf galaxies as a function of normalized cluster-centric radius. Vertical error bars represent 20% of the MAD of each data point.

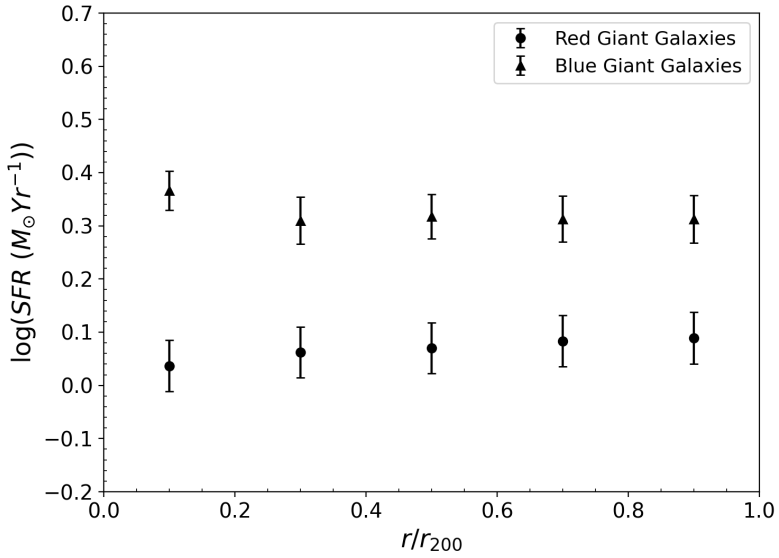

Figure 4.5: Logarithmic value of u-band SFR for red and blue giant galaxies as a function of normalized cluster-centric radius. Vertical error bars represent 20% of the MAD of each data point.

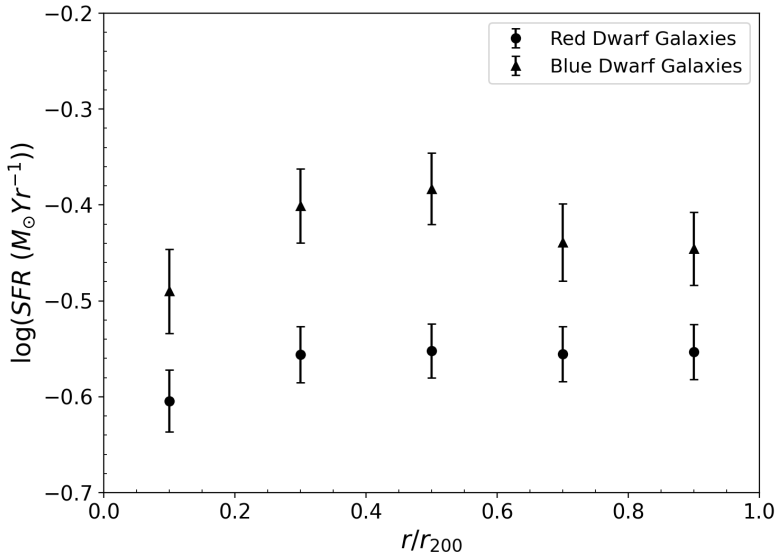

Figure 4.6: Logarithmic value of u-band SFR for red and blue dwarf galaxies as a function of normalized cluster-centric radius. Vertical error bars represent 20% of the MAD of each data point.

Since blue galaxies have more star-forming gas, they are expected to have higher star formation activity compared to red galaxies. Figure 4.2 clearly shows a decrease in the SFR towards the center of the cluster for both blue and red galaxies, with the blue galaxy SFR decreasing more compared to red galaxies. For example, for the two inner-most radial bins, the SFR slope for the blue galaxies depicted in Fig. 4.2 is ~ 4.6 times steeper than for the red galaxies. This decrease in SFR towards the cluster core can be explained by the increasing density of the ICM and ram-pressure stripping of star forming gas, especially in blue galaxies.

The comparison of the SFR of giant and dwarf galaxies shows that giants have more star formation activity than dwarfs at all cluster-centric radii (Figs. 4.3 and 4.4). This is due to giants having more star forming gas overall than dwarf galaxies. Compared to giant galaxies, both red and blue dwarf galaxies experience a greater decrease in the SFR towards the high-density cluster core (Figs. 4.5 and 4.6). Due to their low mass, dwarf galaxies would be more susceptible to the effects of increasing ram-pressure towards the cluster core. The drop in the SFR in blue dwarf galaxies towards the cluster core is consistent with the fact that dwarf galaxies can be easily tidally disrupted, and lose their star-forming gas as they fall into the inner cluster region (see Chapter V). This is supported by the fact that the SFR slope for the blue dwarfs is ~ 2 steeper than for the red dwarfs for the two inner-most radial bins (see Fig. 4.6).

4.3 UV Star Formation Rate

The SFR for GALEX FUV and NUV bands were calculated using the calibrations derived by (Iglesias-Páramo et al., 2006)

$$log(SFR_{NUV})\ (M_{\odot}\ \mathrm{yr}^{-1}) = log(L_{NUV}(L_{\odot})) - 9.33, \tag{4.2}$$

$$log(SFR_{FUV})\ (M_{\odot}\ \mathrm{yr}^{-1}) = log(L_{NUV}(L_{\odot})) - 9.51, \tag{4.3}$$

where $L(NUV)$ and $L(FUV)$ are the extinction and k-corrected NUV and FUV luminosities of a cluster galaxy in units of solar luminosity. These calibrations also assume a solar metallicity and a Salpeter IMF with lower and upper mass cutoffs of 0.1 and 100 $M_{\odot}$.

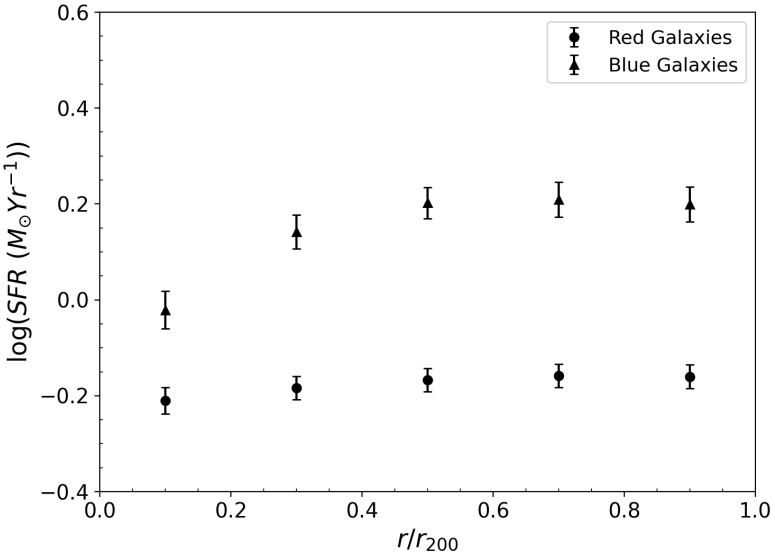

Figure 4.7: Logarithmic value of GALEX NUV band SFR for red and blue cluster galaxies as a function of normalized cluster-centric radius. Vertical error bars represent 20% of the MAD of each data point.

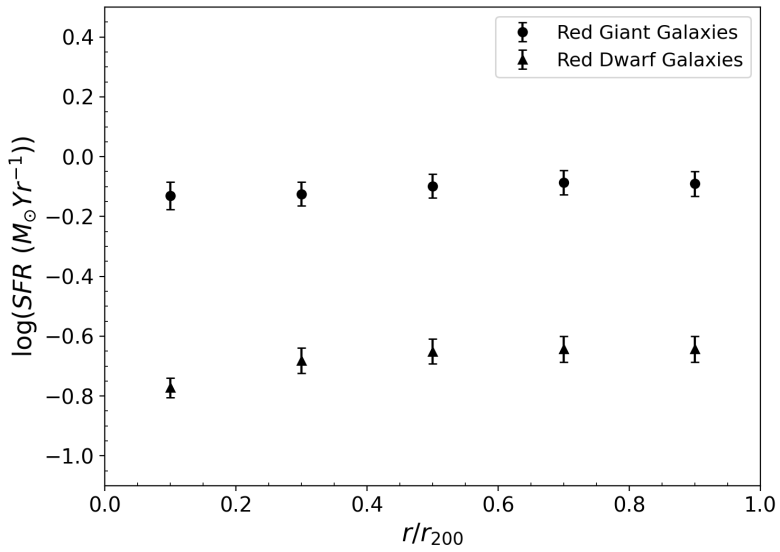

Figure 4.8: Logarithmic value of GALEX NUV band SFR for red giant and dwarf galaxies as a function of normalized cluster-centric radius. Vertical error bars represent 20% of the MAD of each data point.

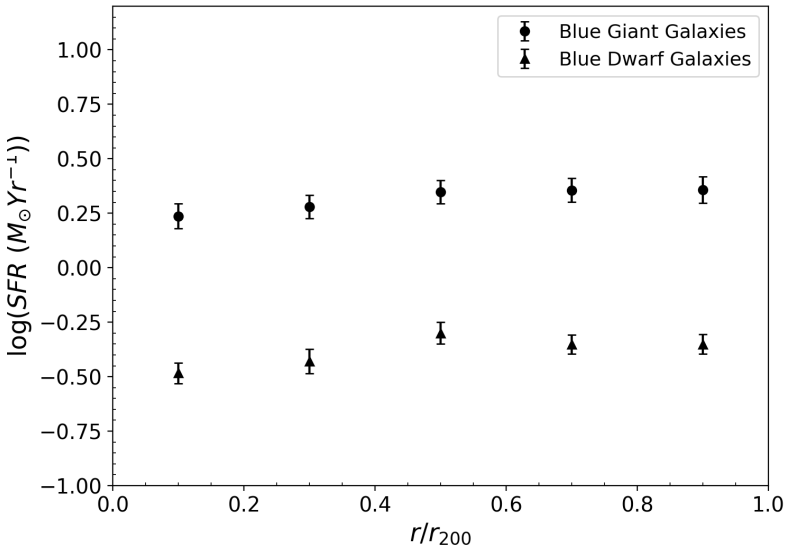

Figure 4.9: Logarithmic value of GALEX NUV band SFR for blue giant and dwarf galaxies as a function of normalized cluster-centric radius. Vertical error bars represent 20% of the MAD of each data point.

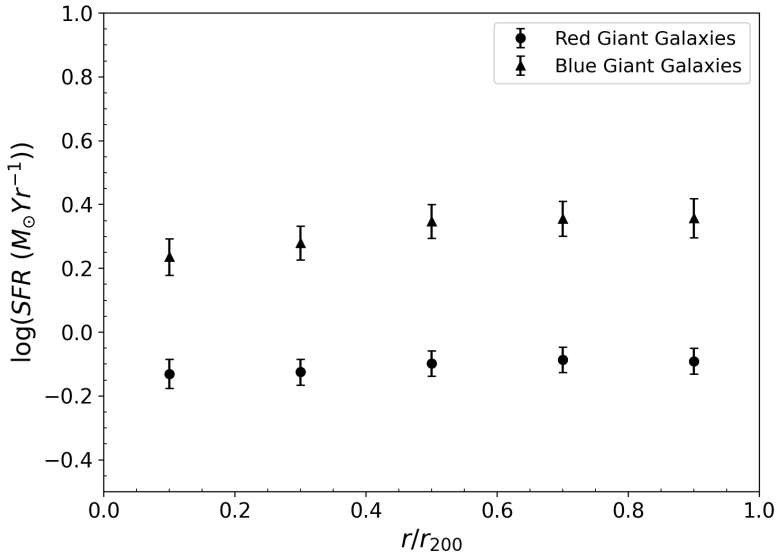

Figure 4.10: Logarithmic value of GALEX NUV band SFR for red and blue giant galaxies as a function of normalized cluster-centric radius. Vertical error bars represent 20% of the MAD of each data point.

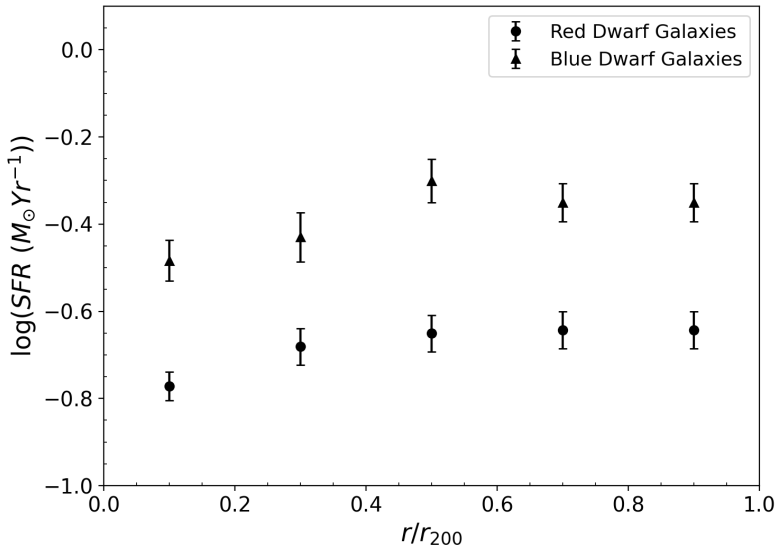

Figure 4.11: Logarithmic value of GALEX NUV band SFR for red and blue dwarf galaxies as a function of normalized cluster-centric radius. Vertical error bars represent 20% of the MAD of each data point.

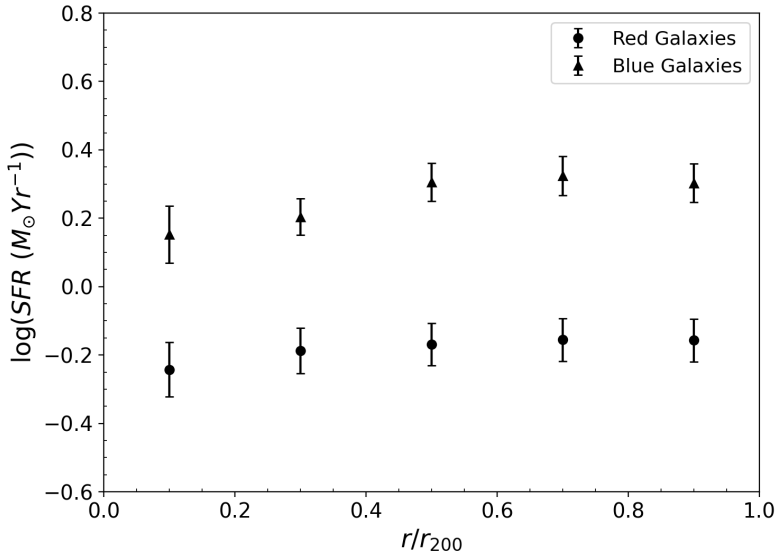

Figure 4.12: Logarithmic value of GALEX FUV band SFR for red and blue cluster galaxies as a function of normalized cluster-centric radius. Vertical error bars represent 20% of the MAD of each data point.

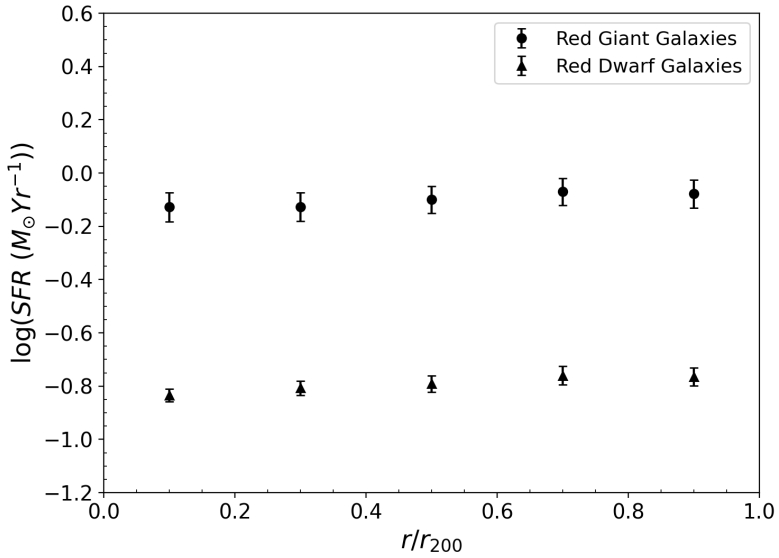

Figure 4.13: Logarithmic value of GALEX FUV band SFR for red giant and dwarf galaxies as a function of normalized cluster-centric radius. Vertical error bars represent 20% of the MAD of each data point.

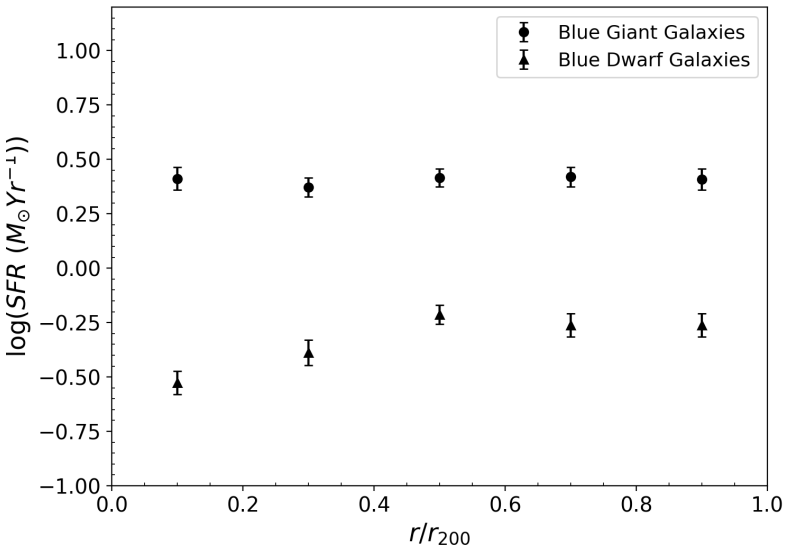

Figure 4.14: Logarithmic value of GALEX FUV band SFR for blue giant and dwarf galaxies as a function of normalized cluster-centric radius. Vertical error bars represent 20% of the MAD of each data point.

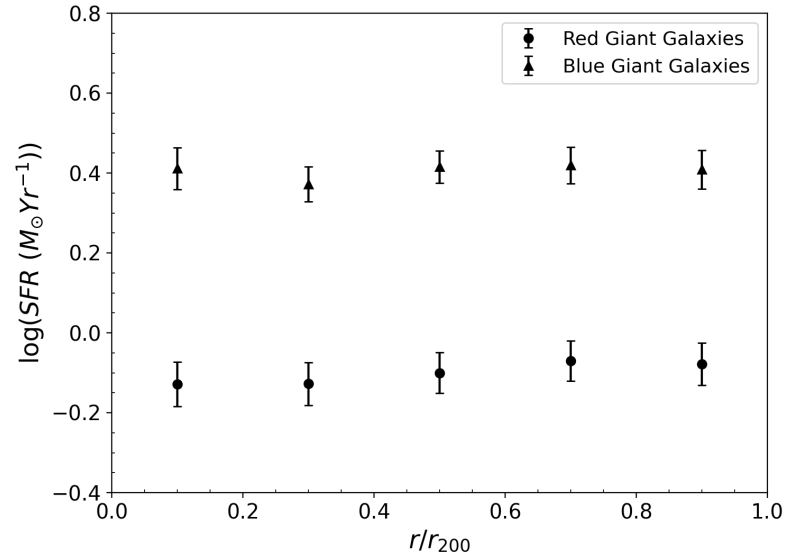

Figure 4.15: Logarithmic value of GALEX FUV band SFR for red and blue giant galaxies as a function of normalized cluster-centric radius. Vertical error bars represent 20% of the MAD of each data point.

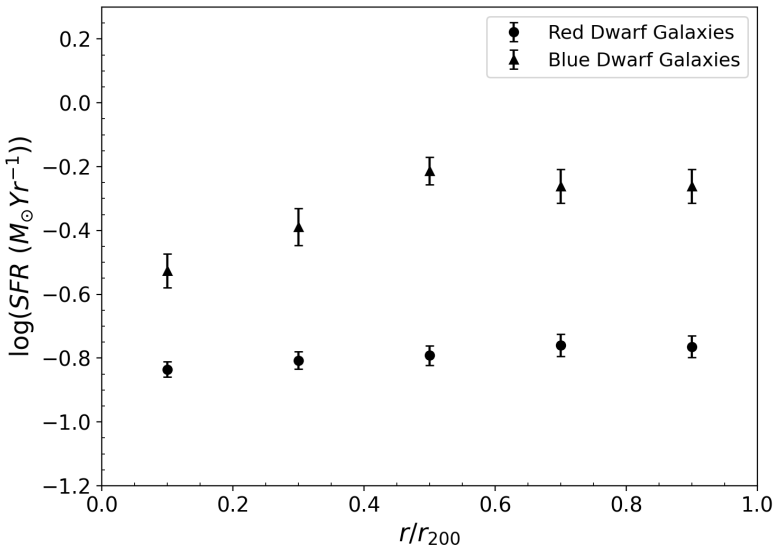

Figure 4.16: Logarithmic value of GALEX FUV band SFR for red and blue dwarf galaxies as a function of normalized cluster-centric radius. Vertical error bars represent 20% of the MAD of each data point.

For both FUV and NUV passbands, the change in SFR is consistent with what was observed in the u-band. A drop in the SFR for the inner cluster region was observed, with blue dwarf galaxies losing their star-forming gas faster compared to red galaxies (Figs. 4.7 - 4.16). Implications of these results are fully discussed in Chapter V.

4.4 IR Star Formation Rate

The SFR for WISE W3 and W4 bands, $\psi(W3)$ and $\psi(w4)$, were calculated using the calibrations derived by (Lee et al., 2013)

$$\psi(W3)\ (M_\odot\ \mathrm{yr}^{-1}) = (1.64 \pm 0.11) \times 10^{-9}\ L_{W3}(L_\odot), \tag{4.4}$$

$$\psi(W4)\ (M_\odot\ \mathrm{yr}^{-1}) = (1.59 \pm 0.11) \times 10^{-9}\ L_{W4}(L_\odot), \tag{4.5}$$

where $L(W3)$ and $L(W4)$ are WISE W3 and W4 luminosities of a cluster galaxy in solar luminosity units. These calibrations also assume a solar metallicity and a Salpeter IMF with lower and upper mass cutoffs of 0.1 and 100 $M_{\odot}$.

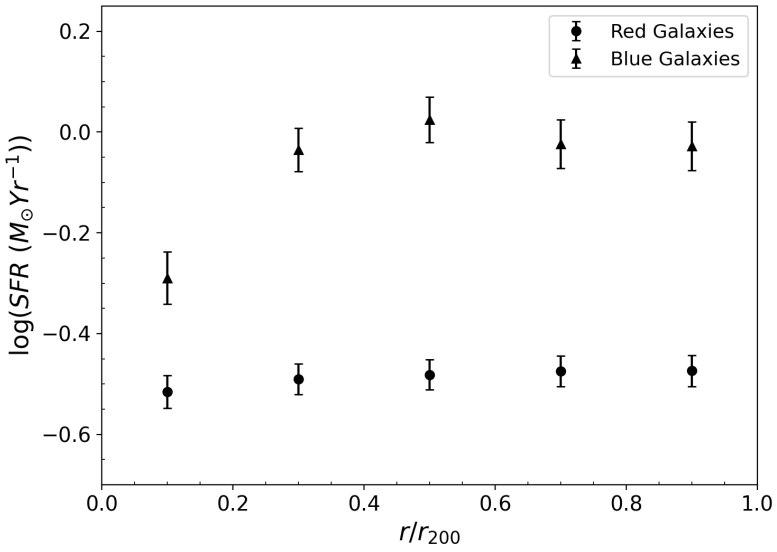

Figure 4.17: Logarithmic value of WISE W3 band SFR for red and blue cluster galaxies as a function of normalized cluster-centric radius. Vertical error bars represent 20% of the MAD of each data point.

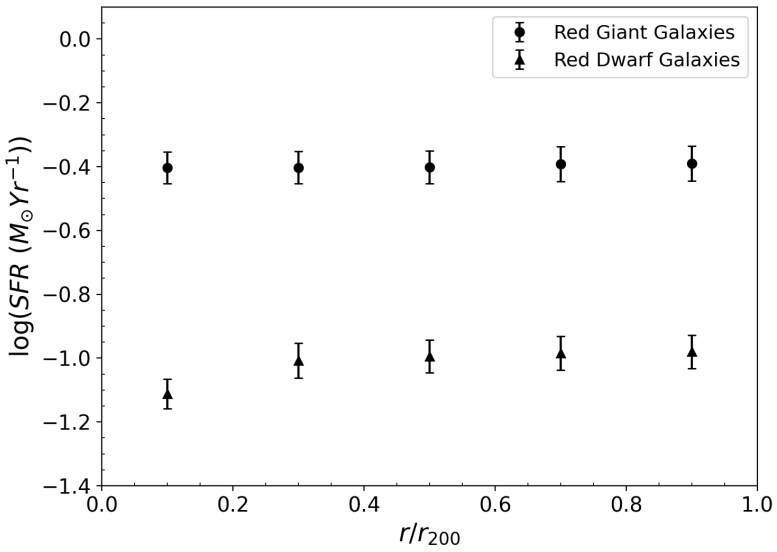

Figure 4.18: Logarithmic value of WISE W3 band SFR for red giant and dwarf galaxies as a function of normalized cluster-centric radius. Vertical error bars represent 20% of the MAD of each data point.

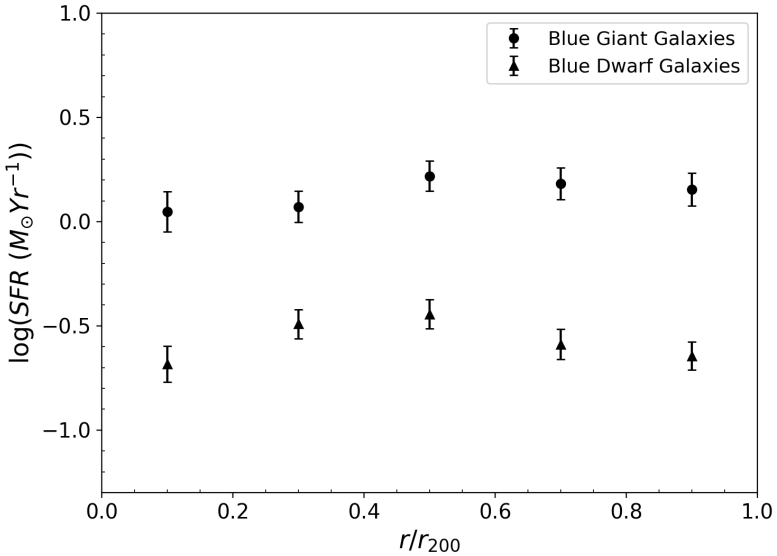

Figure 4.19: Logarithmic value of WISE W3 band SFR for blue giant and dwarf galaxies as a function of normalized cluster-centric radius. Vertical error bars represent 20% of the MAD of each data point.

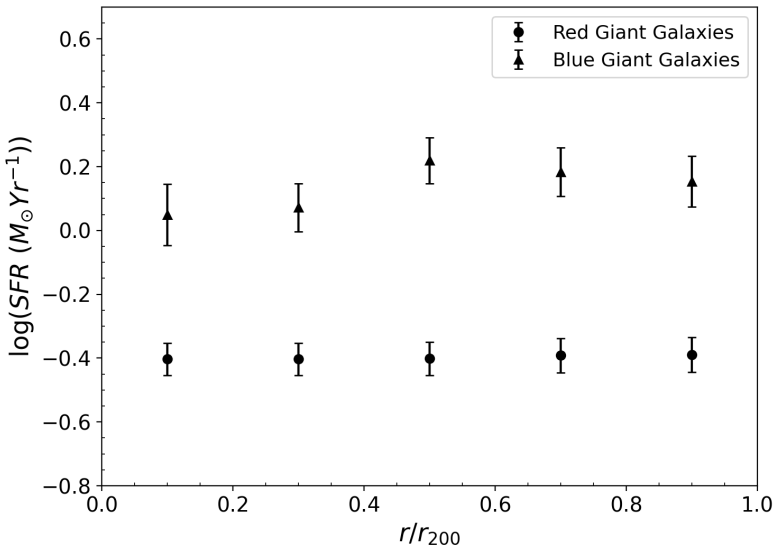

Figure 4.20: Logarithmic value of WISE W3 band SFR for red and blue giant galaxies as a function of normalized cluster-centric radius. Vertical error bars represent 20% of the MAD of each data point.

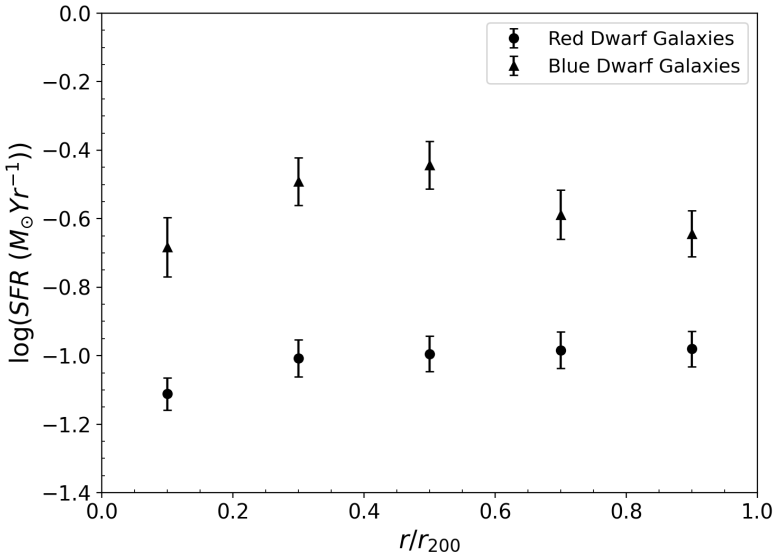

Figure 4.21: Logarithmic value of WISE W3 band SFR for red and blue dwarf galaxies as a function of normalized cluster-centric radius. Vertical error bars represent 20% of the MAD of each data point.

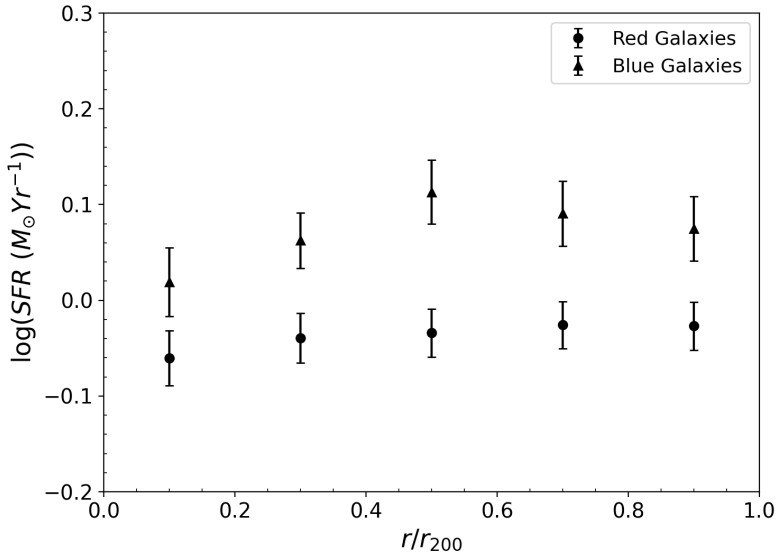

Figure 4.22: Logarithmic value of WISE W4 band SFR for red and blue cluster galaxies as a function of normalized cluster-centric radius. Vertical error bars represent 20% of the MAD of each data point.

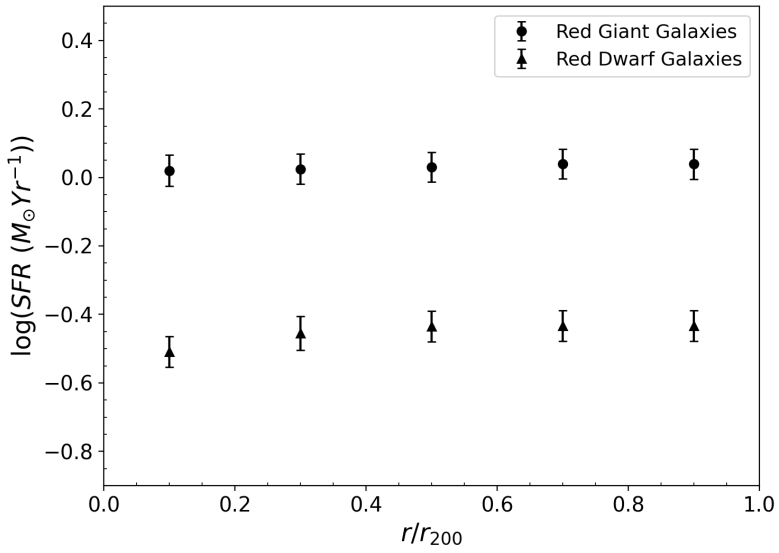

Figure 4.23: Logarithmic value of WISE W4 band SFR for red giant and dwarf galaxies as a function of normalized cluster-centric radius. Vertical error bars represent 20% of the MAD of each data point.

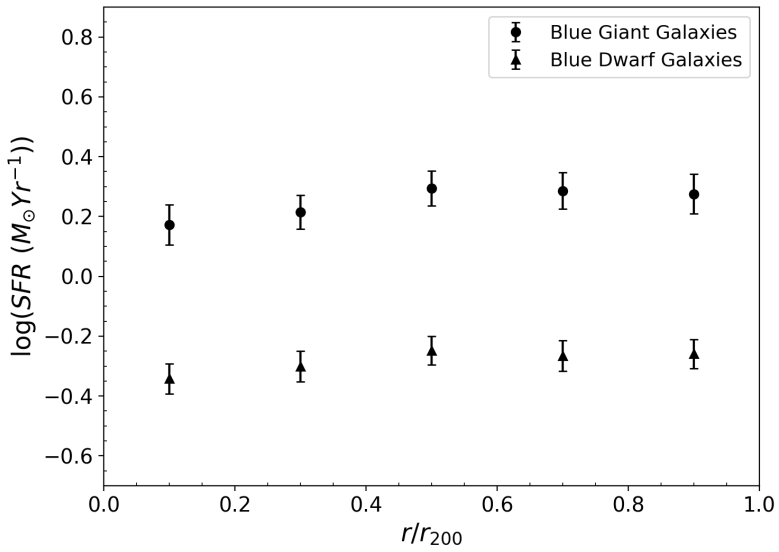

Figure 4.24: Logarithmic value of WISE W4 band SFR for blue giant and dwarf galaxies as a function of normalized cluster-centric radius. Vertical error bars represent 20% of the MAD of each data point.

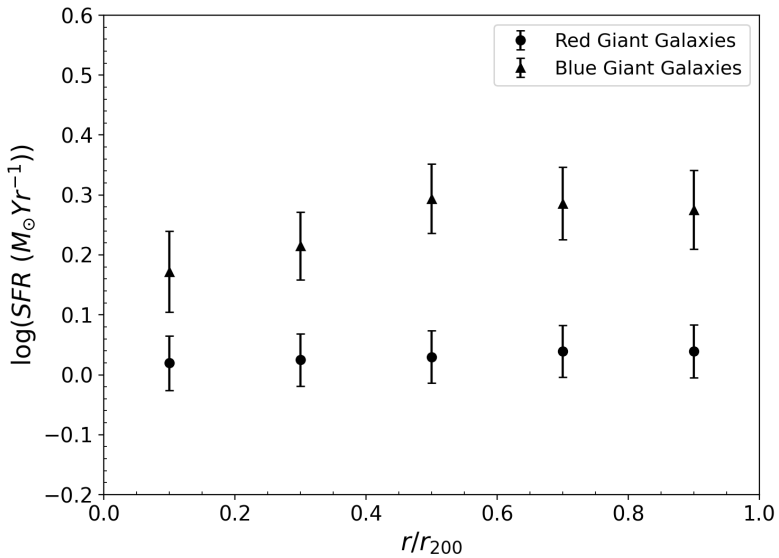

Figure 4.25: Logarithmic value of WISE W4 band SFR for red and blue giant galaxies as a function of normalized cluster-centric radius. Vertical error bars represent 20% of the MAD of each data point.

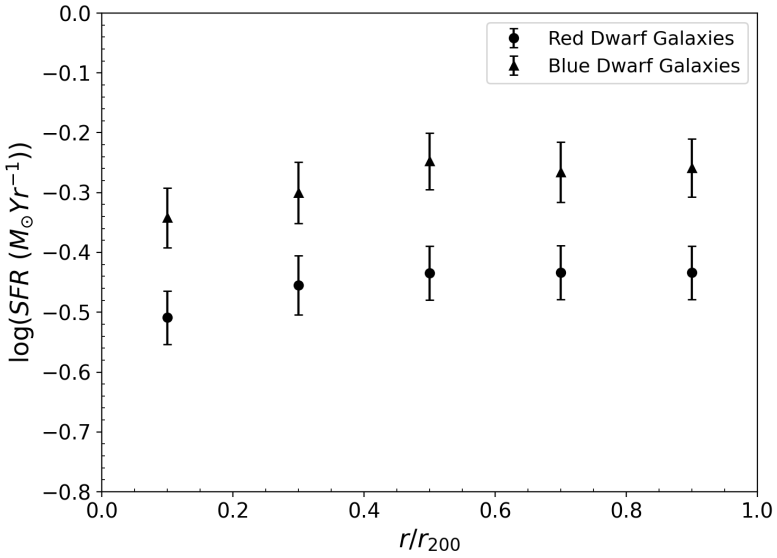

Figure 4.26: Logarithmic value of WISE W4 band SFR for red and blue dwarf galaxies as a function of normalized cluster-centric radius. Vertical error bars represent 20% of the MAD of each data point.

Similar to what was observed in u-band and GALEX passbands, both W3 and W4 SFR measurements decreased in the inner cluster region, with blue dwarf galaxy SFR decreasing more compared to red galaxies (Figs. 4.17 - 4.26).

Chapter V

DISCUSSION

5.1 Introduction

The UV, u-band, and FIR luminosities of star-forming galaxies are closely related to recent star formation: most of the UV photons are originally emitted by younger O, B type stars, but many of these photons are reprocessed by the dust present in galaxies and re-emitted at FIR wavelengths. SFR estimators based on the UV and u-band luminosities suffer from dust attenuation (u-band is less dust biased compared to UV), and it has to be corrected in order to properly trace star formation activity. Though FIR observations are less effected by dust biases, the efficiency of using FIR luminosities as a SFR tracer depends on factors such as escape fraction and dust heating from old stars (Iglesias-Páramo et al., 2006). Hence, neither of these passbands alone can provide a complete measurement of the star formation activity within a cluster.

5.2 Star Formation in Galaxy Clusters

The main goal of this dissertation is to study the SFR of cluster galaxies as a function of cluster-centric radius using multi-wavelength data to investigate how the cluster environment affects galaxy evolution. Though the change in star formation with radius has been the subject of several studies (Gómez et al., 2003; Taranu et al., 2014), they are limited to using one or two passbands for a relatively small sample of

clusters, and do not sample the dwarf galaxy population. In this study, I present a multi-wavelength analysis of the SFR of 74 low redshift galaxy clusters as a function of normalized cluster-centric radius. To further understand these effects, cluster galaxies are divided into two bins using: 1) color (red and blue) and 2) luminosity (giants and dwarfs).

As shown in Figures 4.2, 4.7, 4.12, 4.17, and 4.22, a decrease in the SFR was observed towards the cluster center in all passbands, with the blue galaxy SFR decreasing more than the red galaxies. A similar decrease of SFR towards the cluster center was observed in Balogh et al. (2000), Gómez et al. (2003), and Mahajan et al. (2012), for the combined cluster galaxy population.

Using Hα observations of 10 low-redshift galaxy clusters conducted at the KPNO 4-m telescope, Vithanage (2018) found indications of quenching of star formation towards the cluster center, especially for dwarf galaxies. Very little change in the SFR with cluster-centric radius was observed for giant galaxies (Fig. 5.1). This may be due to a selection bias introduced by Vithanage (2018) selecting galaxies within $\pm 3\sigma$ of the red sequence as cluster galaxies, and thus excluding high star forming galaxies that occupy the region $> 3\sigma$ blueward of the red-sequence.

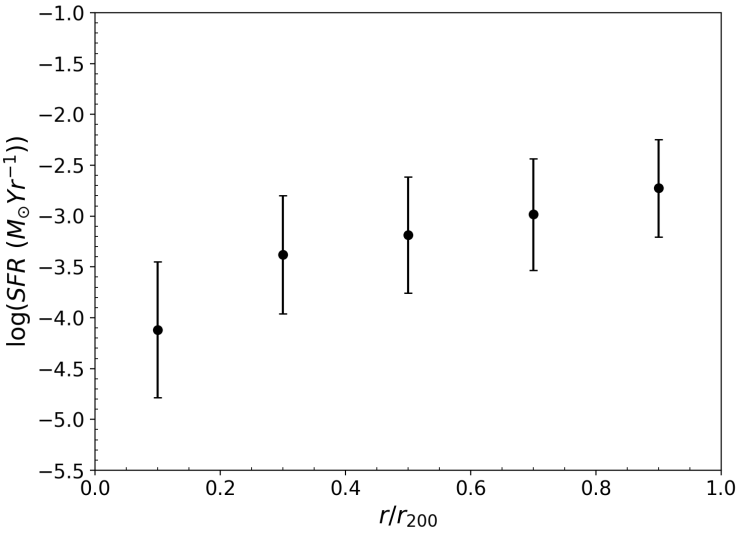

(a)

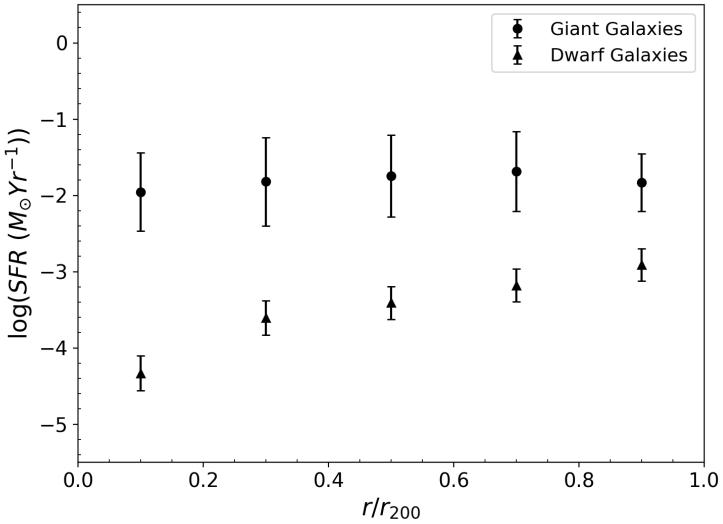

(b)

Figure 5.1: Hα SFR as a function of cluster-centric radius from Vithanage (2018) for (a) total cluster galaxy population and (b) for giant and dwarf galaxies.

Using SDSS spectroscopic data, Mahajan et al. (2012) studied the star formation activity of galaxies in 107 nearby clusters ($0.02 \leq z \leq 0.15$). They found the mean SFR of galaxies declines towards the cluster core, while the star formation in the

cluster outskirts ($1 - 2\ r/r_{200}$) was enhanced. Mahajan et al. separated their sample into two categories: clusters with at least one starburst galaxy (log SFR/$M^* \geq -10\ yr^{-1}$ and SFR $\geq 10 M_\odot$ yr^{-1}) and clusters without such galaxies, where M^* is the stellar mass. For both categories, they found that the SFR decreases towards the cluster center, with clusters with no starburst galaxies showing a lower SFR at all cluster-centric radii (Fig. 5.2). A comparison with my results show a noticeable difference. Mahajan et al. analyzed the SFR of only bright galaxies, defined as galaxies with $M_r < -20.5$, and no consideration was given to the location of these galaxies relative to the red-sequence (i.e. no color separation). The results of my study show that blue dwarf galaxies are most responsible for the decrease in the SFR towards the cluster center. Hence, it is important to consider radial gradients of dwarf and giant galaxies separately, along with their color.

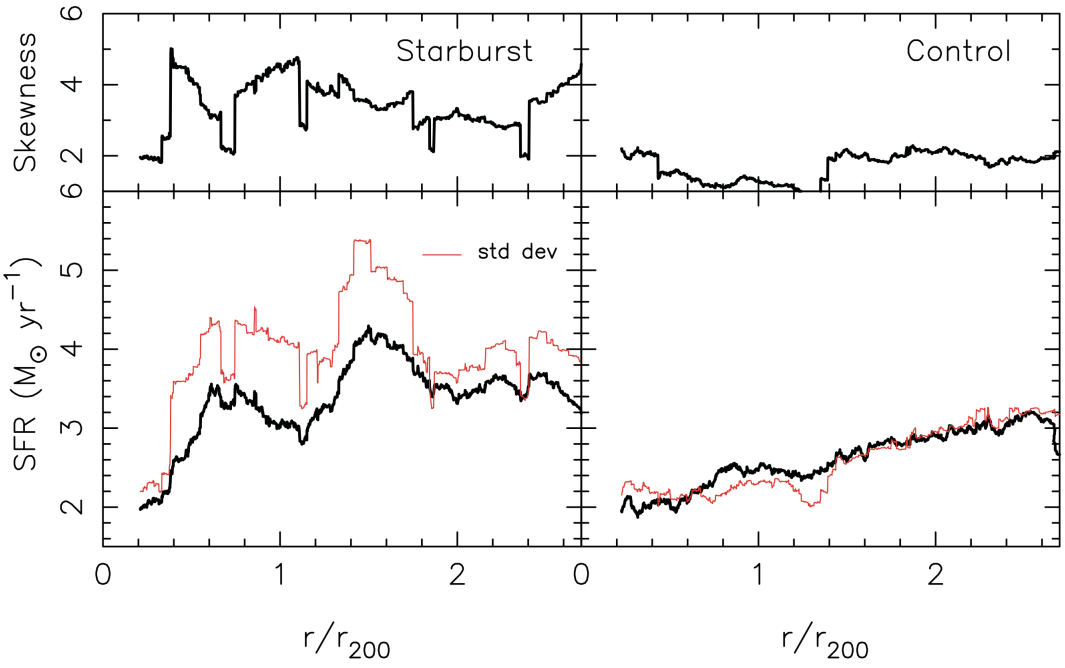

Figure 5.2: The mean (thick line, bottom panel), skewness (upper panel), and the standard deviation (thin red, bottom panel) in SFR of galaxies in starburst (left) and non-starburst (right) clusters as a function of scaled cluster-centric radius (Mahajan et al., 2012). The decrease in the SFR towards the cluster center is apparent. Also, in general, the mean SFR of non-starburst clusters is lower than that of starburst clusters.

A study conducted by Balogh et al. (2000), which used galaxy spectra of 15 low-redshift X-ray luminous clusters from the Canadian Network for Observational Cosmology (CNOC) survey, and a spectroscopic study by Gómez et al. (2003) using the SDSS early data release, found a decline in the SFR towards the cluster center (Figures 5.3 and 5.4). It is important to note that both studies only analyzed bright galaxies ($M_r \leq -19.5$ for Balogh et al. and $M_r < -20.45$ for Gómez et al.) and each galaxy sample was selected without regards to galaxy color. Thus, a decrease in the SFR toward the high-density cluster core region for giant galaxies is not unexpected given that the sample contains galaxies with a large range of star formation activity.

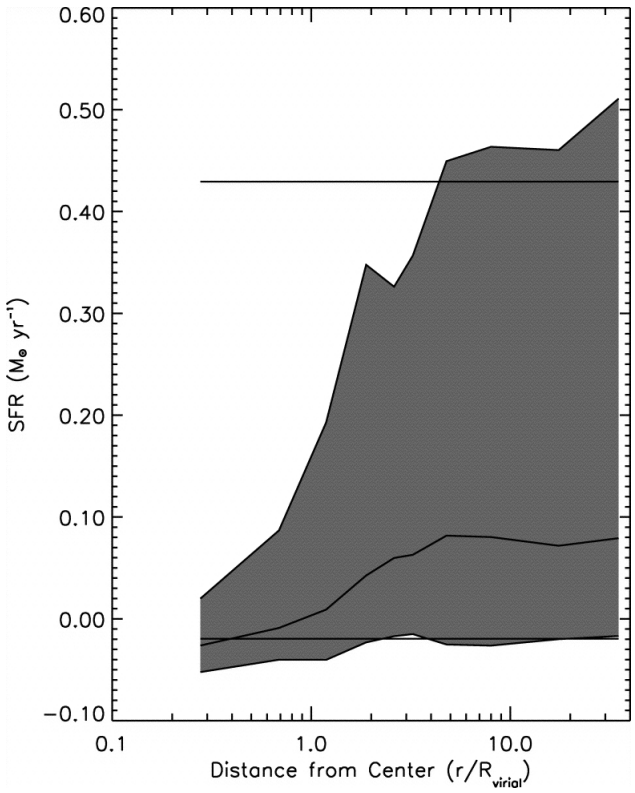

Figure 5.3: SFR as a function of normalized cluster centric radius from Gómez et al. (2003). Shaded area is the distribution of SFR values and line inside the middle is the median values. Top and bottom straight lines are the 75th and 25th percentile of the SFR.

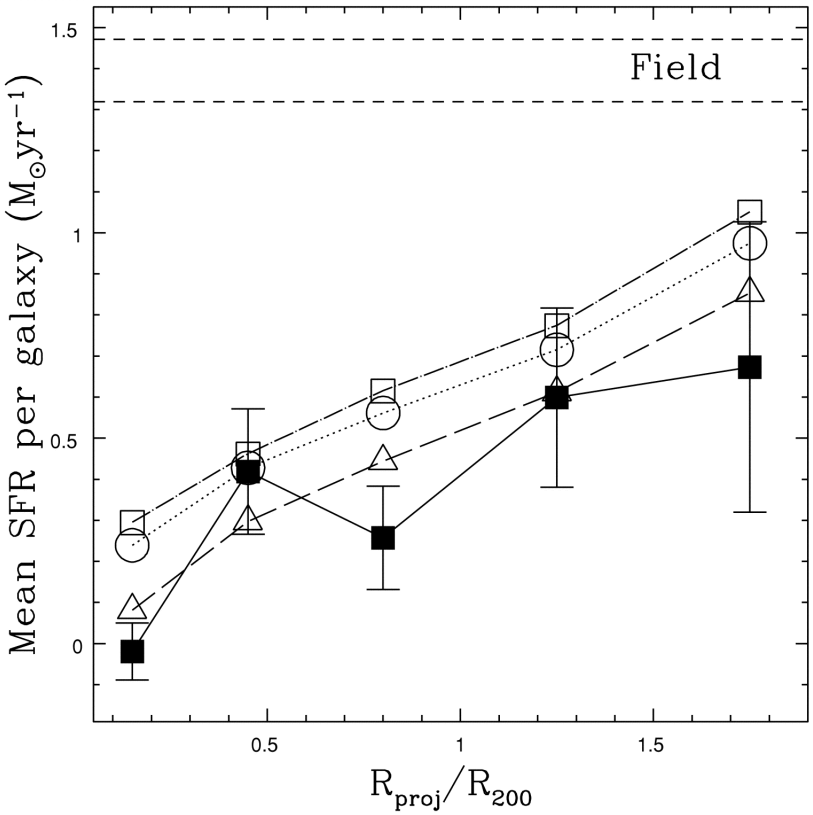

Figure 5.4: SFR as a function of cluster-centric radius from Balogh et al. (2000). CNOC data are marked in black squares. The open symbols represent numerical simulations using different galaxy accretion models.

In addition to the overall decline in the SFR with decreasing cluster-centric radius, Balogh et al. (2000) found a slight enhancement of star formation at $r/r_{200} \sim 0.5$. There is marginal evidence for such an enhancement in my sample. But, due to the large uncertainties as indicated by the scattering of the data, and the low number of galaxies with flux measurements (e.g. dwarf galaxies), statistically, the SFR for radius $> 0.5\ r/r_{200}$ is constant. More data are necessary to reduce uncertainties and see if this trend holds true for radii $> 0.5\ r/r_{200}$. Also, the enhancement observed in Balogh et al. may be due to the rich nature of the cluster sample used in their study, in the sense that a greater incidence of galaxy-galaxy interaction and higher ram pressure may cause star formation to be enhanced before it is truncated once gas is removed from various cluster galaxies. Balogh et al. used three different

models to describe galaxy accretion into the cluster environment to help explain the enhancement and general decline of the SFR with decreasing cluster-centric radius (Fig. 5.4). No enhancement was found for these models, while a larger relative drop of the SFR for the central cluster region was observed for the CNOC data compared to numerical simulations.

5.2.1 GALEX–SDSS–WISE Legacy Catalog

Spectral energy distribution (SED) fitting is becoming a widely used technique for deriving galaxy properties. The GALEX–SDSS–WISE Legacy Catalog contains physical properties of galaxies, such as stellar mass and current SFR, with a redshift range of $0.01 < z < 0.30$, and an r-band magnitude < 18 (Salim et al., 2016) ($M_r \sim -19$ using the median redshift of my cluster sample). The GSWLC uses the Code Investigating GALaxy Emission (CIGALE) software package to perform galaxy SED fits. CIGALE compares model fluxes with observed fluxes and uses a χ^2 minimization to select the best fit model to calculate physical properties of galaxies (Yang et al., 2020).

There are two versions of the catalog: GSWLC-1 and GSWLC-2. GSWLC-1, described in Salim et al. (2016), calculates SFRs using UV/optical SED fitting. In GSWLC-2, the mid-IR flux from the WISE W4 passband (or W3, if W4 data is not available) is used in the SED fitting procedure jointly with UV/optical photometry to derive more accurate SFRs (Salim et al., 2018).

GSWLC-2 data are available for 58 clusters used in this study, and was used as a tool to compare findings. Each cluster galaxy was searched for in GSWLC-2 using a three arcsecond search radius to compensate for small WCS offsets. In the case of multiple matching objects, the SFR measurements from the closest positional match were used. Following the same procedure used for photometric data, SFRs derived using SED fitting were plotted as a function of normalized cluster-centric radius for

all galaxies (Figures 5.5 - 5.9).

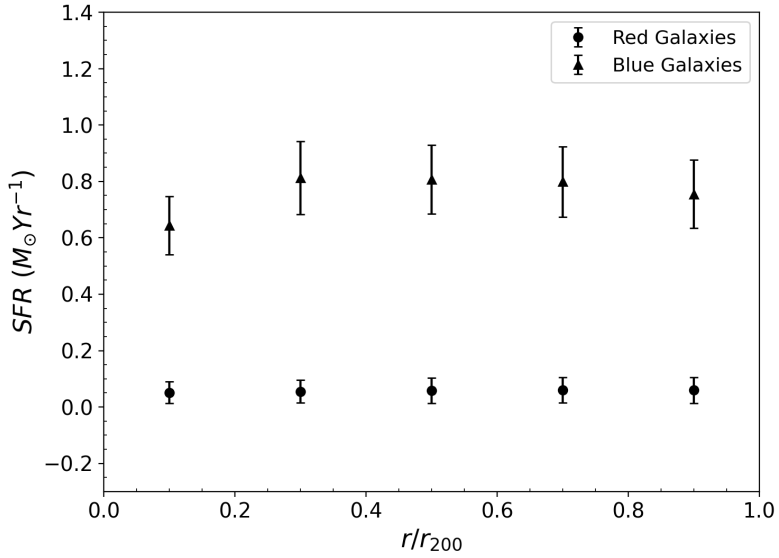

Figure 5.5: GSWLC SFR of red and blue cluster galaxies as a function of normalized cluster-centric radius. Vertical error bars represent 20% of the MAD of each data point.

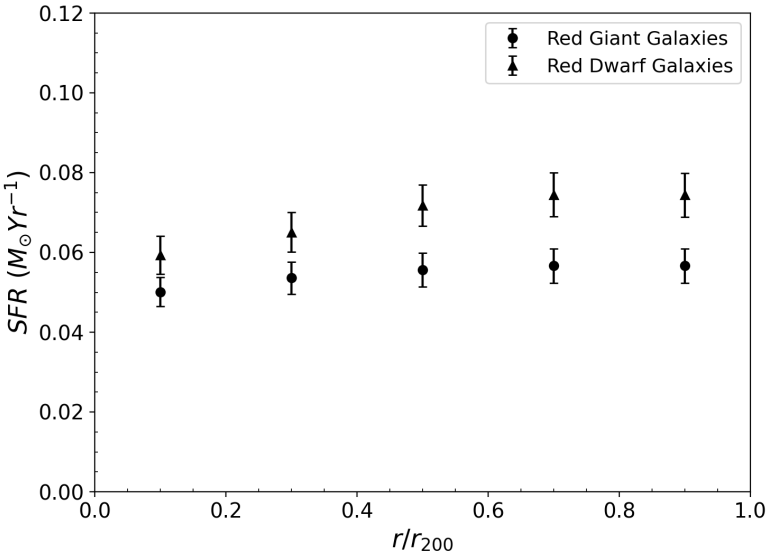

Figure 5.6: GSWLC SFR of red giant and dwarf galaxies as a function of normalized cluster-centric radius. Vertical error bars represent 20% of the MAD of each data point.

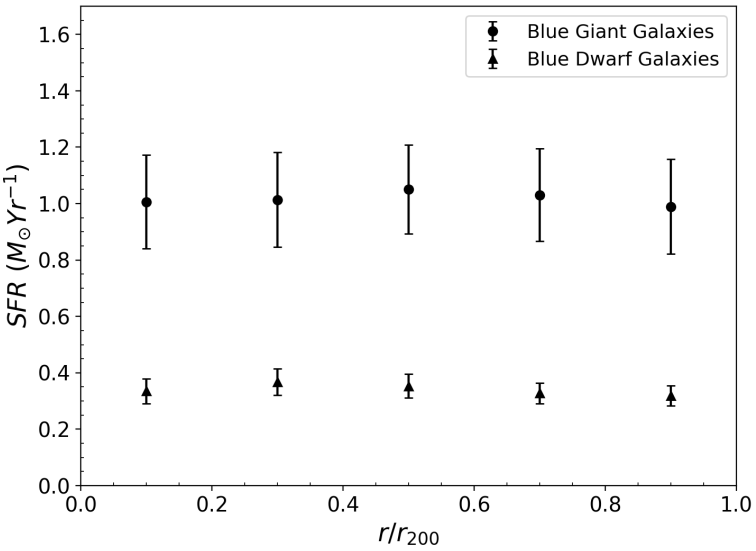

Figure 5.7: GSWLC SFR of blue giant and dwarf galaxies as a function of normalized cluster-centric radius. Vertical error bars represent 20% of the MAD of each data point.

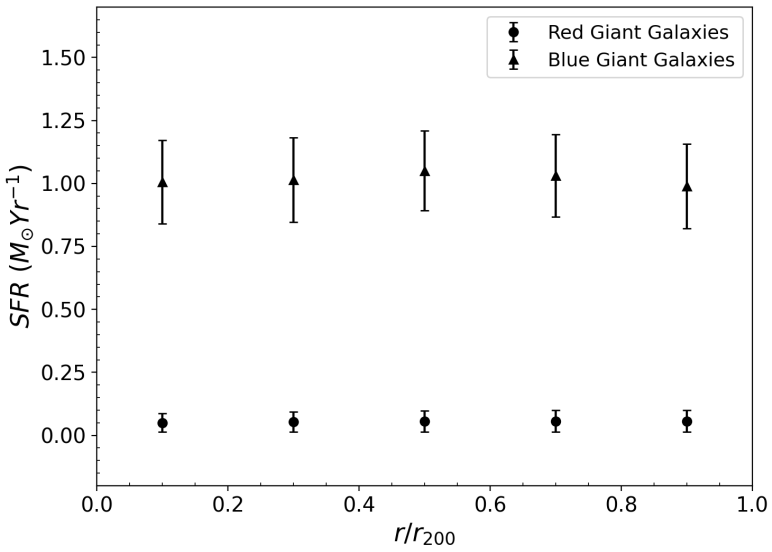

Figure 5.8: GSWLC SFR of red and blue giant galaxies as a function of normalized cluster-centric radius. Vertical error bars represent 20% of the MAD of each data point.

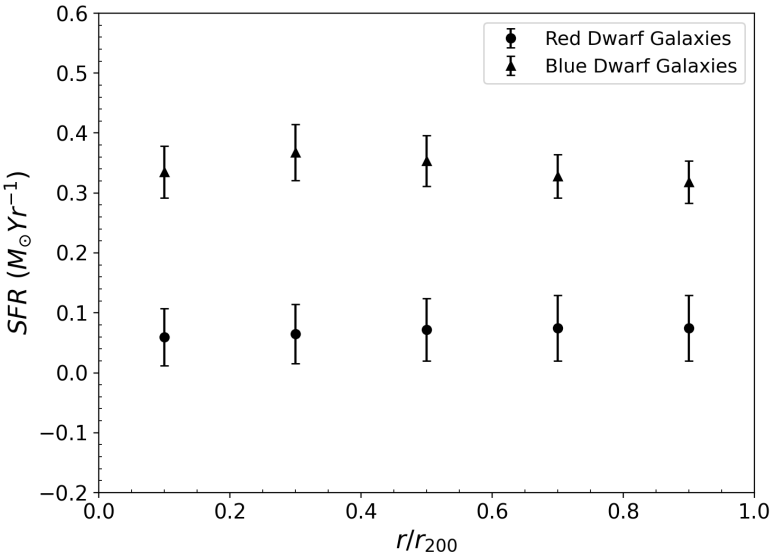

Figure 5.9: GSWLC SFR of red and blue dwarf galaxies as a function of normalized cluster-centric radius. Vertical error bars represent 20% of the MAD of each data point.

Similar to what was observed for the photometrically determined SFR, GSWLC SFR measurements decreased towards the cluster center. Also, as expected, giant galaxies have a higher SFR than dwarf galaxies at all cluster-centric radii. However, due to the relatively low number of matching objects (65% on average), especially for dwarf galaxies, the decrease towards the cluster center is less significant compared to photometrically-derived SFRs.

5.3 Cluster Environment and Star Formation

As mentioned in chapter I, the physical conditions present in a high-density cluster environment, such as ram pressure stripping, galaxy harassment, and galaxy strangulation, can affect the SFR in cluster galaxies.

Ram pressure is proportional to the ISM density and the relative velocity of a galaxy (equation 1.4). Due to the deep gravitational potential well associated with the cluster's central region, the density of the ICM and the relative velocity of a galaxy increases towards the cluster center. This also implies that ram pressure increases towards the center of the cluster. Hence, an increase in ram pressure can influence the SFR when a galaxy moves towards the dense central region. If ram pressure overcomes the self-gravity that attracts the ISM to the host galaxy, the gas will be torn away from the galaxy, thus quenching star formation. Several studies have suggested that this effect has the greatest impact on dwarf galaxies due to their low mass (Marcolini et al., 2003; Vithanage, 2018; Rude et al., 2020). The quenching of star formation towards the cluster core was observed for all passband data used in this study. The larger drop in the SFR toward the central cluster region for dwarfs compared to giant galaxies, supports the idea that ram pressure is a dominant mechanism in changing star formation activity towards the cluster center.

In addition to ram pressure stripping, galaxy harassment can also affect star formation in clusters, especially towards the cluster core. Galaxy harassment depends

on collisional frequency, the strength of individual collisions, and the distribution of mass within galaxies (Boselli & Gavazzi, 2006). Although the duration of the interactions might be short due to high relative velocities, the frequency of interactions are maximum in the central cluster region. Multiple encounters will heat the ISM of the host galaxy, causing it to expand. Due to their different potential distributions, effects of galaxy harassment should be less pronounced for giant galaxies compared to dwarfs. As a combined result of galaxy-galaxy and galaxy-cluster gravitational interactions, galaxy harassment might also be effective in the cluster outskirts (Boselli & Gavazzi, 2006). For example, the abundance of dwarf ellipticals can be explained by galaxy harassment transforming loosely bound low-mass galaxies into dwarf ellipticals by interacting with a more massive galaxy (see section 1.4.3).

Since the central accumulation of gas and the heating of molecular clouds, increase the probability of cloud-cloud encounters in galaxies, the enhancement of star formation is also expected. This is known to be an important mechanism in low- and intermediate-density environments (Mahajan et al., 2012). At the same time, Bialas et al. (2015) found evidence that the harassment mechanism becomes more efficient for galaxies with orbital perigee close to the cluster center. According to published results (Balogh et al., 2000), an enhancement of star formation is more likely to happen at $(r/r_{200}) \geq 0.5$. As mentioned in the previous section, more data are required to see if this result holds true for the galaxy sample used in this study.

Galaxy starvation or strangulation was proposed by Larson et al. (1980) to explain the transformation of spirals into S0 galaxies. Spiral galaxies are believed to be embedded in an extended gas reservoir that feeds star formation. Since the gas reservoir is loosely bound to the galaxy, it can be easily removed preventing further infall of gas into the galaxy. Using numerical simulations, Bekki et al. (2002) showed that even if a spiral orbits a cluster with a pericenter distance ~ 3 times larger than the cluster core radius, it will lose $\sim 80\%$ of its halo gas via stripping within a few Gyrs.

Such gas removal results mainly from the hydrodynamical interaction between the halo gas and the ICM. Eventually, the spiral structure will become less pronounced, and the galaxy will become a disk-dominated S0-type galaxy. Gas strangulation happens over a longer time scale (a few Gyrs) compared to ram pressure stripping ($\sim$ 50 Myr), and is found to be more effective in the outskirts of clusters compared to the central cluster region.

Chapter VI

SUMMARY AND FUTURE WORK

6.1 Summary

Multi-wavelength observations at UV, u-band and IR wavelengths of 74 low-redshift galaxy clusters were used to study the SFR of cluster galaxies as a method of understanding the effects of cluster environment on the evolution of galaxies. The KPNO 0.9m+HDI telescope/detector was used to obtain u-band observations of 14 galaxy clusters. This dataset was supplemented by 18 clusters from the study of Barkhouse et al. (2007), 10 cluster from Omizzolo et al. (2014), 13 clusters from Rude et al. (2020), and 19 cluster from Valentinuzzi et al. (2011).

The IRAF software package was used to perform bias and flat field calibrations for KPNO 0.9m data. IRAF was also used to make final cluster images by combining individual exposures of the same cluster. The BCG in each cluster was modeled using the `ELLIPSE` and `BMODEL` tasks in IRAF, and removed for accurate photometric measurements of neighboring galaxies. Object detection, classification, and magnitude measurements were completed using PPP. Object magnitudes were transformed to the AB magnitude system by calibrating with respect to galactic-extinction corrected u-band magnitudes from the SDSS. The completeness limit of the cluster galaxy sample was determined using the turnover magnitude of the galaxy counts. The red-sequence for each cluster was fit with a straight line, and the dispersion of the red-sequence was used to separate cluster galaxies into red and blue color bins. Redshift measurements obtained from the SDSS spectroscopic data were used to select cluster galaxies.

Final cluster galaxy catalogs were matched with archival data from GALEX and WISE satellites to measure fluxes at UV and IR wavelengths, respectively. GALEX data were corrected for galactic extinction using dust maps developed by Schlegel et al. (1998), and for internal extinction following Cortese (2012). u-band and GALEX data were k-corrected based on redshift and color (Chilingarian et al., 2010). No extinction or k-corrections were applied to WISE data since these corrections are negligible.

Cluster luminosity distances were calculated following the procedure used in Wright (2006). The r_{200} dynamical radius was calculated for each cluster using published cluster velocity dispersions. This radius was used to normalize radius-dependent star formation gradients from the center of each cluster. Extinction and k-corrected apparent magnitudes of each passband were converted into line fluxes using the definition of AB magnitude (Brown et al., 2017).

The u-band, UV, and IR SFR of blue and red galaxies were calculated using calibrations derived by Moustakas et al. (2006), Iglesias-Páramo et al. (2006), and Lee et al. (2013), respectively, and plotted as a function of normalized cluster-centric radius. The cluster galaxy sample was analyzed separately for dwarf and giant galaxies. Indications of the quenching of star formation towards the cluster center was observed, with blue dwarf galaxies losing a higher fraction of their star-forming gas compared to red galaxies. Ram pressure stripping was identified as a dominant mechanism for quenching star formation towards the cluster core, while other mechanisms such as galaxy harassment and starvation were found to be more effective outside the cluster core.

Changes in the SFR with cluster-centric radius were compared with published results from Balogh et al. (2000), Gómez et al. (2003), Mahajan et al. (2012) and Vithanage (2018). The decline of the SFR towards the cluster center was consistent with these published studies. However, Balogh et al. (2000), Gómez et al. (2003), and Mahajan et al. (2012) results are based on a sample of giant galaxies with no color

separation and thus are not directly comparable to my results. Using Hα observations, Vithanage (2018) found evidence for the quenching of star formation in dwarf galaxies towards the cluster center, but very little change in the SFR with cluster-centric radius was observed for giant galaxies. Photometrically derived SFR measurements were compared with SFR measurements derived using UV, optical, and mid-IR SED fitting, and were found to be consistent.

6.2 Future Work

Though the use of spectroscopic data of galaxies help to better determine cluster membership, it is biased against selecting dwarf galaxies due to their faint magnitudes. A large telescope is required to measure the dwarf galaxy population with a high enough signal-to-noise ratio so that star-forming emission lines are adequately sampled to determine line fluxes and redshift. Telescopes, such as the Thirty Meter Telescope (TMT)[1], will be available in the future to conduct detailed spectroscopic studies of star formation in nearby galaxy clusters. Extending multi-wavelength observations to fainter luminosities as the technology advances, and conducting detailed investigations of the star formation aspect of cluster dwarf galaxies, is extremely important since low-mass galaxies are an excellent probe in helping us to understand important physical processes at work in the galaxy cluster environment.

6.2.1 Red-Sequence Spiral Galaxies

Examination of the morphology of galaxies occupying the cluster red-sequence indicates that a small fraction ($\sim 10\%$) are spirals. For spiral galaxies to be red in color like ellipticals/S0s at a similar luminosity, and thus to be found in the red-sequence, they either have been stripped of their star-forming gas at an earlier epoch or contain a larger than normal fraction of dust. Preliminary analysis conducted using WISE

[1] `https://www.tmt.org`

magnitudes for 422 face-on spiral galaxies, indicates that red-sequence spirals do not contain a large fraction of dust. In fact, red-sequence spirals are similar in color (W1-W2 vs.W2-W3) to E/S0 galaxies while non-red-sequence spirals concentrate at the "blue-end" of the spiral sequence (Figs. 6.1 and 6.2). This supports the idea that red-sequence spiral galaxies are passively evolving like E/S0 systems (Kausher et al. 2022 (in preparation)).

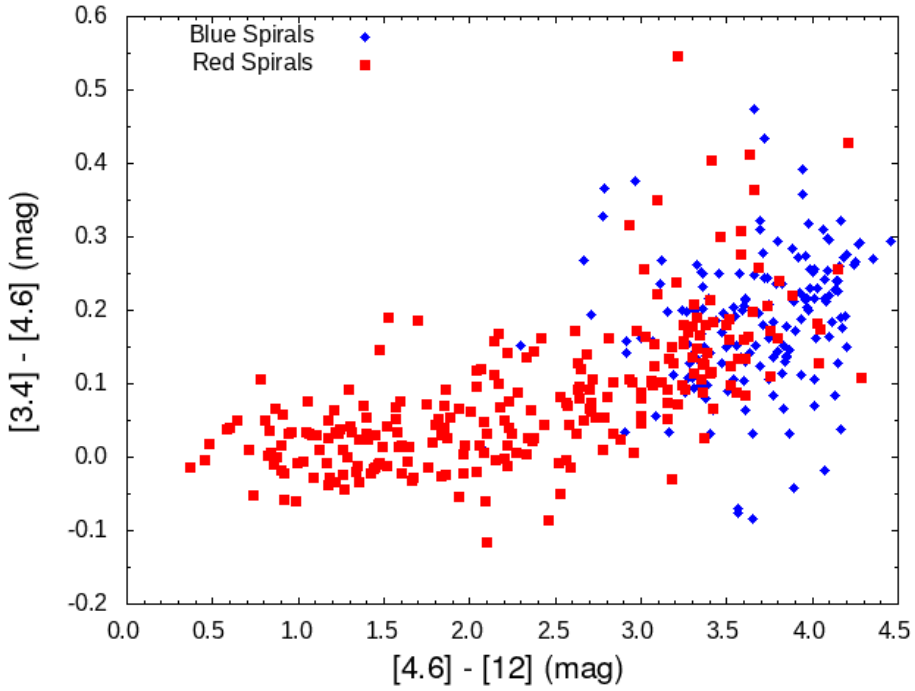

Figure 6.1: WISE color-color plot of red-sequence and non-red-sequence spiral galaxies. Numbers in square brackets are the central wavelengths, in microns, of WISE filters.

One possibility for such a suppression of star formation in red cluster spirals can be feedback from AGN heating (Bower et al., 2006). WISE data of galaxies can be used to select galaxies that have a high probability of containing an AGN (Toba et al., 2015). These galaxies can then be isolated when looking for non-AGN factors that could quench star-formation in the remaining red-sequence spiral galaxy population. GALEX FUV and NUV flux measurements have also been used to help select non-

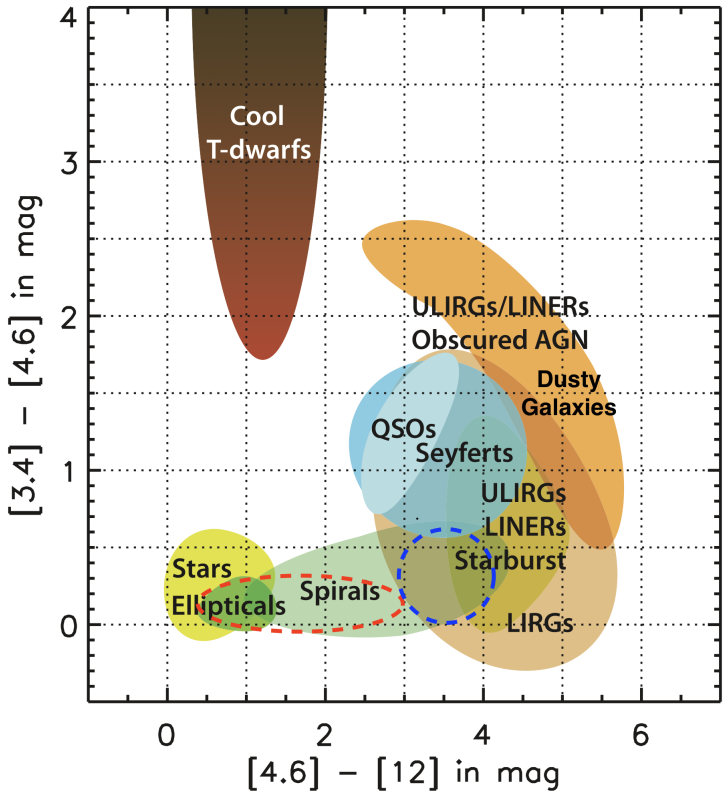

Figure 6.2: WISE color-color diagram adopted from Wright et al. (2010) overlaid with our galaxy sample. Red- and blue-dashed regions represent red-sequence and non-red-sequence spirals, respectively. Note that, red, dusty galaxies are located towards the middle-right and do not overlap with the red-sequence spirals.

AGN galaxies (Ramos Padilla et al., 2020). Exploring the use of UV-IR color-color data created by matching GALEX and WISE data can help select AGN galaxies and determine their impact on star formation.

REFERENCES

Abell G. O., 1958, ApJS, 3, 211

Abell G. O., 1962, in *IAU Symp.* p. 213

Abraham R. G., van den Bergh S., 2001, Science, 293, 1273

Balogh M. L., Navarro J. F., Morris S. L., 2000, AJ, 540, 113

Barkhouse W. A., Yee H., López-Cruz O., 2007, ApJ, 671, 1471

Barkhouse W. A., Yee H. K. C., López-Cruz O., 2009, ApJ, 703, 2024

Bauer F. E., Alexander D. M., Brandt W. N., Hornschemeier A. E., Vignali C., Garmire G. P., Schneider D. P., 2002, AJ, 124, 2351

Baum W. A., 1959, PASP, 71, 106

Bautz L. P., Morgan W. W., 1970, ApJ, 162, L149

Bayliss M. B., et al., 2017, ApJ, 837, 88

Bekki K., Couch W. J., Shioya Y., 2002, ApJ, 577, 651

Bell E. F., 2003, ApJ, 586, 794

Bialas D., Lisker T., Olczak C., Spurzem R., Kotulla R., 2015, AAP, 576, A103

Boselli A., Gavazzi G., 2006, PASP, 118, 517

Bower R. G., Benson A. J., Malbon R., Helly J. C., Frenk C. S., Baugh C. M., Cole S., Lacey C. G., 2006, MNRAS, 370, 645

Brown M. J. I., et al., 2017, ApJ, 847, 136

Butcher H., Oemler A. J., 1978, ApJ, 219, 18

Carlberg R. G., 1984, ApJ, 286, 416

Castagné D., Soucail G., Pointecouteau E., Cappi A., Maurogordato S., Benoist C., Ferrari C., 2012, AAP, 548, A18

Cava A., et al., 2009, AAP, 495, 707

Chilingarian I. V., Melchior A.-L., Zolotukhin I. Y., 2010, MNRAS, 405, 1409

Cortese L., 2012, AAP, 543, A132

Demarco R., et al., 2010, ApJ, 711, 1185

Dressler A., 1980, AJ, 236, 351

Eisenstein D. J., Hu W., 1998, ApJ, 496, 605

Fukugita M., Ichikawa T., Gunn J., Doi M., Shimasaku K., Schneider D., 1996, AJ, 111, 1748

Gladders M. D., Yee H., 2000, AJ, 120, 2148

Gladders M. D., López-Cruz O., Yee H. K. C., Kodama T., 1998, ApJ, 501, 571

Gómez P. L., et al., 2003, ApJ, 584, 210

Goto T., Yamauchi C., Fujita Y., Okamura S., Sekiguchi M., Smail I., Bernardi M., Gomez P. L., 2003, MNRAS, 346, 601

Griffiths R. E., Padovani P., 1990, ApJ, 360, 483

Gunn J. E., et al., 1998, ApJ, 116, 3040

Hausman M. A., Ostriker J. P., 1978, ApJ, 224, 320

Hodge P. W., 1971, ARAA, 9, 35

Hopkins A. M., et al., 2003, ApJ, 599, 971

Howell S. B., 2006, Handbook of CCD Astronomy. Cambridge University Press

Hubble E., 1925, AJ, 62, 409

Iglesias-Páramo J., et al., 2006, ApJs, 164, 38

Jarrett T. H., et al., 2011, ApJ, 735, 112

Jedrzejewski R. I., 1987, MNRAS, 226, 747

Kennicutt R. C., 1998, ARAA, 36, 189

Kennicutt R. C., Evans N. J., 2012, ARAA, 50, 531

Kodama T., Arimoto N., 1997, AAP, 320, 41

Kravtsov A. V., Borgani S., 2012, ARAA, 50, 353

Larson R., Tinsley B., Caldwell C., 1980, AJ, 237, 692

Lauer T. R., Postman M., Strauss M. A., Graves G. J., Chisari N. E., 2014, ApJ, 797, 82

Lee J. C., Hwang H. S., Ko J., 2013, AJ, 774, 62

López-Cruz O., Yee H., Brown J. P., Jones C., Forman W., 1997, ApJL, 475, L97

Lopez-Cruz O., Barkhouse W. A., Yee H. K. C., 2004, The Astrophysical Journal, 614, 679

Mahajan S., Raychaudhury S., Pimbblet K. A., 2012, MNRAS, 427, 1252

Marcolini A., Brighenti F., D'Ercole A., 2003, MNRAS, 345, 1329

Martin D. C., et al., 2005, ApJ, 619, L1

Mo H., van den Bosch F. C., White S., 2010, Galaxy Formation and Evolution. Cambridge University Press

Moore B., Katz N., Lake G., Dressler A., Oemler A., 1996, Nature, 379, 613

Morrissey P., et al., 2005, ApJL, 619, L7

Moustakas J., Kennicutt Robert C. J., Tremonti C. A., 2006, ApJ, 642, 775

Omizzolo A., et al., 2014, AAP, 561, A111

Piffaretti R., Arnaud M., Pratt G. W., Pointecouteau E., Melin J. B., 2011, AAP, 534, A109

Popesso P., Biviano A., Böhringer H., Romaniello M., 2007, AAP, 461, 397

Ramos Padilla A. F., Ashby M. L. N., Smith H. A., Martínez-Galarza J. R., Beverage A. G., Dietrich J., Higuera-G. M.-A., Weiner A. S., 2020, MNRAS, 499, 4325

Ranalli P., Comastri A., Setti G., 2003, AAP, 399, 39

Rood H. J., Sastry G. N., 1971, PASP, pp 313–319

Rude C. M., Sultanova M. R., Kaduwa Gamage G. L. I., Barkhouse W. A., Kalawila Vithanage S. P., 2020, MNRAS, 493, 5625

Salim S., et al., 2016, ApJS, 227, 2

Salim S., Boquien M., Lee J. C., 2018, ApJ, 859, 11

Salpeter E. E., 1955, ApJ, 121, 161

Schechter P., 1976, ApJ, 203, 297

Schlafly E. F., Finkbeiner D. P., 2011, ApJ, 737, 103

Schlegel D. J., Finkbeiner D. P., Davis M., 1998, ApJ, 500, 525–553

Schneider P., 2007, Extragalactic astronomy and cosmology: an introduction. Springer Science & Business Media

Seigar M. S., Lynam P. D., Chorney N. E., 2003, MNRAS, 344, 110

Smee S. A., et al., 2013, AJ, 146, 32

Stott J. P., Pimbblet K. A., Edge A. C., Smith G. P., Wardlow J. L., 2009, MNRAS, 394, 2098

Struble M. F., Rood H. J., 1999, ApJ, 125, 35

Taranu D. S., Hudson M. J., Balogh M. L., Smith R. J., Power C., Oman K. A., Krane B., 2014, MNRAS, 440, 1934

Toba Y., et al., 2015, PASJ, 67

Tovmassian H. M., Andernach H., 2012, MNRAS, 427, 2047

Vader J., Sandage A., 1991, AJ, 379, L1

Valentinuzzi T., et al., 2011, AAP, 536, A34

Visvanathan N., Sandage A., 1977, ApJ, 216, 214

Vithanage S., 2018, PhD thesis, The Department of Physics and Astrophysics, University of North Dakota

Voit G. M., 2005, Reviews of Modern Physics, 77, 207

White D. A., Jones C., Forman W., 1997, MNRAS, 292, 419

Wright E. L., 2006, PASP, 118, 1711

Wright E. L., et al., 2010, AJ, 140, 1868

Wyder T. K., et al., 2007, ApJS, 173, 293

Yang G., et al., 2020, MNRAS, 491, 740

Yee H., 1991, PASP, 103, 396

York D. G., et al., 2000, AJ, 120, 1579

Yuan H. B., Liu X. W., Xiang M. S., 2013, MNRAS, 430, 2188

Zezas A., Baut V., eds, 2021, Star-Formation Rates of Galaxies. Cambridge University Press

Zwicky F., 1933, Helvetica Physica Acta, 6, 110

Zwicky F., Herzog E., Wild P., Karpowicz M., Kowal C. T., 1961, Catalogue of galaxies and of clusters of galaxies, Vol. I

de Jongl T., Klein U., Wielebinski R., Wunderlich E., 1985, Astron. Astrophys, 147, L6